Spin-Orbit Torque Control of Nanomagnetic Devices Probed by Nitrogen-Vacancy Centres in Diamond

Adrian Solyom

Physics Department, McGill University

Montréal, Québec, Canada

May 2023

A thesis submitted to McGill University in partial fulfillment of the requirements of the degree of Doctor of Philosophy

co-supervised by

Dr. Jack Sankey and Dr. Lilian Childress

Abstract

Novel computing architectures based on encoding information in magnons (spin wave excitations in magnets) show promise for improved energy efficiency and enabling biology-inspired neuromorphic computing. Spin orbit torques (SOTs) offer an attractive method for controlling magnonic circuits: they are capable of applying torques to localized geometries with high efficiencies per unit current that improve as the device dimensions are reduced. SOTs have been used for state-switching magnetic domains in nonvolatile memories, and can also dynamically anti-damp or damp magnetic resonances to stimulate large-angle oscillations of magnon modes or to squash them. As these devices decrease in size and energy, new detection modalities are needed to measure device characteristics and compare them with simulations, as existing techniques typically exhibit diffraction-limited spatial resolution.

To this end, we develop nitrogen-vacancy (N-V) sensing techniques to measure the oscillating fields of magnetic nanowires driven by SOTs. The point-like nature of N-V centres enables non-invasive nanoscale probing of devices: by observing optically detected magnetic resonance (ODMR), we detect the magnetic stray field at static and GHz frequencies. We fabricate bilayer devices of permalloy (Py) and Pt on diamond to enable SOT control of the magnetic layer in proximity of our N-V probe. Applying SOTs enables us to parametrically excite magnon modes, which we detect via ODMR to measure the oscillating field from while isolating the pump. We show that this excitation modality enables crosstalk-free detection of the magnetization, as the Oersted field from the microwave currents are isolated from the N-V frequencies. Furthermore, spin relaxometry measurements detect SOT-mediated cooling of the thermal magnons in the absence of microwave driving.

We further refine our nanofabrication process to make smaller devices capable of undergoing auto-oscillations when subject to strong anti-damping. We can resolve the magnon modes in our studied device, and we observe synchronization to the parametric drive. Comparing the measured ODMR spectra to magnetic simulations and measurements made in transport elucidates the features seen in the N-V fluorescence, allowing interpretation of such signals for future device characterization. We detect that parametrically driving a second mode can

sap the power of an auto-oscillating mode, indicating that N-Vs can be a useful tool for further study of inter-mode coupling in the nonlinear regime.

Abrégé

De nouvelles architectures informatiques basées sur le codage d'informations dans des magnons (les excitations de spin dans des aimants) sont prometteuses pour améliorer l'efficacité énergétique et permettre l'informatique neuromorphique inspirée de la biologie. Les couples spin-orbite (SOTs) offrent une méthode intéressante pour contrôler les circuits magnoniques: ils sont capables d'appliquer des couples à des géométries localisées avec des efficacités élevés par unité de courant qui s'améliorent à mesure que les dimensions de l'appareil sont réduites. Les SOTs ont été utilisés pour le changement d'état de domaines magnétiques dans les mémoires non volatiles, et peuvent également appuyer des couples d'anti-amortisement ou d'amortisement pour stimuler les oscillations à grand angle des modes magnon ou les écraser. Au fur et à mesure que ces dispositifs diminuent en taille et en énergie, de nouvelles modalités de détection sont nécessaires pour mesurer les caractéristiques des dispositifs et les comparer aux simulations, car les techniques existantes présentent généralement une résolution spatiale limitée par la diffraction.

À cette fin, nous développons des techniques de détection de la lacune d'azote (N-V) pour mesurer les champs oscillants des nanofils magnétiques entraînés par les SOTs. La nature ponctuelle des centres N-V permet un sondage nanométrique non invasif des dispositifs: en observant la résonance magnétique détectée optiquement (ODMR), nous détectons le champ magnétique émit par l'aimant aux fréquences statiques et GHz. Nous fabriquons des dispositifs bicouche Py/Pt sur diamant pour permettre le contrôle SOT de la couche magnétique à proximité de notre sonde N-V. L'application de SOT nous permet d'exciter paramétriquement les modes magnon, que nous détectons via ODMR pour mesurer le champ oscillant tout en isolant la pompe. Nous montrons que cette modalité d'excitation permet une détection sans diaphonie de l'aimantation, car le champ d'Oersted des courants micro-ondes est isolé des fréquences N-V. De plus, les mesures de relaxométrie de spin détectent le refroidissement médié par SOT des magnons thermiques en l'absence des micro-ondes.

Nous affinons davantage notre processus de nanofabrication pour fabriquer des dispositifs plus petits capables de subir des auto-oscillations lorsqu'ils sont soumis à un fort antiamortissement. Nous pouvons résoudre les modes magnons dans notre dispositif étudié, et nous observons une synchronisation avec le motif paramétrique. La comparaison des spectres ODMR mesurés aux simulations magnétiques et aux mesures effectuées dans le transport élucide les caractéristiques observées dans la fluorescence N-V, permettant l'interprétation de ces signaux pour la caractérisation future de l'appareil. Nous détectons que la commande paramétrique d'un second mode peut saper la puissance d'un mode auto-oscillant, indiquant que la magnétometrie N-V peut être un outil utile pour l'étude des couplages inter-mode dans le régime non linéaire.

Acknowledgements

I am honoured to have been supervised equally by Jack and Lily, whose mentorship I am truly grateful to have received for the better part of a decade. Their expertise spans the fields of spin-current controlled nanomagnetic systems and atomic molecular optics using colour centers, disparate domains whose overlap forms the foundation of this thesis. I have learned so much from Jack's knowledge of microwave circuits, nanofabrication and programming. Lily's intuition into the intricate world of quantum optics and her amazing teaching abilities have likewise helped me to learn how to better translate my ideas to page.

None of my work would have been possible without the technical help in microfabricating our devices. Robert, Zhao, Jun, and Peng have all helped me to understand how to use the many tools McGill has at its disposal. Without the help of Marie-Josée from l'Institut Interdisciplinaire d'Innovation Technologique, Marie-Héléne from Polytechnique, and Pat from Western Digital, none of the precisely fabricated nanowires would have been possible.

I also recognize the insightful discussions I have had with the many colleagues and friends in the physics department, particularly those I've known from the lab: Rigel, César, Michael, Maggie, Luke, Erika, Nathaniel, Mark, Märta, Yannik, as well as Fernanda, Pauline, Simon, Vincent, Tommy, Jiaxing, Raphael, Christoph, Abeer, André, Valeria, and Vlad. It has been an absolute pleasure having you in my life since I've moved to Montreal. Zack, these experiments would not have been possible without the extensive groundwork you have done, and I'm glad to have your enduring friendship.

I thank Yves, Dominique, Jean, and Vanessa for running the QSciTech training program, whose curriculum has proven to be invaluable in helping me in managing my project. I am grateful for the program funding which allowed me to intern with SBQuantum. I have learned so much from the team there; and am particularly lucky to have worked and learned from David, Vincent, Olivier, Saddem, Guillaume, and Mathieu.

Through my development as a scientist has been positively influenced by the vast network of people who have taught me and helped me achieve my goals. My life has been enriched with the many experiences I've shared with my friends from St. Catharines, including Mo, Connor, Brennan, Joey, Eric, Ross, and Brannen among the many. I feel equally priviledged for the friendships I've made in Hamilton, especially with Avi, Greg, Nick, Usman, Leo, Alissa, David, and Ahmed.

I recognize the immense support and love I've been given by all my family; especially from Carter, Isabel, my mom and dad, my grandmother and my omi. Alex, Jenn, Dani, Katie, Alie, and Emily, I am so grateful to have you in my life.

And to Laura, thank you for all your hard work and patience with me over the years. I never would have been able to see this through without you by my side.

Contents

List of Figures

Chapter 1

Introduction

Since the mid-20th century, the rapid advancement in computational technologies has allowed for faster and more efficient approaches in almost every field of human endeavour, from the design of new medicines and technologies to the conception of art and culture. The Information Age has gone hand in hand with Moore's law: the observation that iterative improvements lead to an exponential growth in the transistor count of computers, roughly pegged as a doubling every two years. While this scaling has held true for half a century, quantum mechanics places physical limits on the miniaturization of MOSFET devices that has slowed the continued scaling in computing power. In order to overcome these obstacles, entirely new architectures for information processing must be created, which requires multidisciplinary development of new materials, circuit designs, and algorithms.

The work presented in this thesis focuses on probing spin-current-controlled nanomagnetic systems, which have been proposed as one such alternative resource in computing design. Using the spin degree of freedom to encode information has the potential to making computing far more energy efficient than charge-based techniques. However, this promise of low-energy operation comes with additional overhead requirements to characterize their performance in sufficient detail to optimize their design. To this end, quantum sensing protocols based on the nitrogen-vacancy (N-V) centre in diamond are developed to non-invasively probe the stray field of these devices. In Section 1.1, we will explore the motivation and context behind the use of spin-based devices. We will briefly discuss the methods for characterizing spin wave excitations in Section 1.2 before concentrating on the principles of N-V magnetometry in Section 1.3. Finally, we discuss N-V applications to nanomagnetic systems in Section 1.4 before presenting the bodies of work composing this thesis.

1.1 Spintronics

Spintronics is a long-established field of research and industry devoted to the development of computing techniques that rely on the spin degree of freedom of electrons to encode information [1,2]. Magnetism that emerges from long-range correlations of spins in a material is inherently non-volatile; as long as the magnetic volume is large enough to be made insusceptible to thermal fluctuations, the magnet will keep its state without outside intervention. Magnetism has been used to store information for decades since the introduction of hard disk drives (1956, IBM) and cassette tapes (1962, Philips). These original examples would manipulate magnetic states by applying a magnetic field using an induction loop; however, the spatial extent of the induced field has limited the miniaturization of devices. In addition, bits were traditionally addressed mechanically, limiting the speed and longevity of such storage devices.

In this section, we explore techniques for the efficient manipulation of magnetic devices and the detection of their spin-wave dynamics. Advances in magnetoresistive readout have shown order-of-magnitude changes in resistance that depend on the magnetization state [3]. Materials with circuit-scale spin diffusion lengths permit spin currents to transport magnetic polarization for the application of strong, localized torques [4]. We will discuss how these torques can efficiently excite magnetic "spin waves", and the applications made possible by encoding signals in their phase or amplitude [5,6].

1.1.1 Magnetoresistive detection

Readout via magnetoresistance (arising from spin-dependent transport) is one way to electrically detect the bulk magnetization of a sample. Anisotropic magnetoresistance (AMR) was the first such effect discovered in 1856 by William Thomson [7]. In this original experiment, he noticed that the resistance of iron and nickel was lowest when the current flowed through the metal in the same direction as an applied magnetic field (and thus its magnetization), while it was highest when the current was perpendicular to the field. The effect arises from spin-scattering processes that occur between conduction electrons and the spins that make up the magnet [8–10].

The typical magnitude of AMR is limited to a few percent for most materials, but more recently discovered effects such as giant magnetoresistance (GMR) [11,12] and tunneling magnetoresistance (TMR) [13, 14] exhibited far larger resistance changes. While AMR involves passing current through a single magnetic domain, both GMR and TMR work by passing current between two narrowly separated domains in series. The magnetization of each layer is set by their respective density of states. When both domains have parallel magnetization, these densities of states are well matched, and current can flow between them. Antiparallel configurations of the domains lead to a mismatch between the densities of states that leads to increased scattering and resistance to current flow. GMR initially attracted more attention by using a non-magnetic metal spacer (such as copper) between the domains, achieving a 130% resistance change at room temperature [15]. More recently, TMR has been shown to achieve even greater results, with changes as high as 604% at room temperature [3], by instead using a thin insulating layer (such as MgO) between the domains. The large increase in resistance afforded by TMR allows for easy readout of spin states while using minimal energy.

Such two-domain readout schemes are also referred to as “spin valves” because the relative magnetization between the layers turns on or off the charge current through the devices. By imposing an asymmetry in the size of the two magnetic layers, control is only needed on the smaller, more susceptible “free” layer while the larger layer remains “fixed”. Pillars made with this geometry are known as magnetic tunnel junctions (MTJs) and have already been integrated into commercial hard-disk read heads. This mechanism is also the typical readout mechanism for solid-state magnetic storage devices, such as magnetic random access memory (MRAM) and racetrack storage, both of which will be briefly described in the following sections.

1.1.2 Spin transfer torques

The same spin-dependent scattering that gives rise to magnetoresistance also naturally generates spin currents. This spin current carries angular momentum and (again through spin-dependent scattering) exerts a spin-transfer torque (STT) on the magnetic layers [1]. When the size of the magnetic domain is sufficiently reduced, STTs can efficiently control the

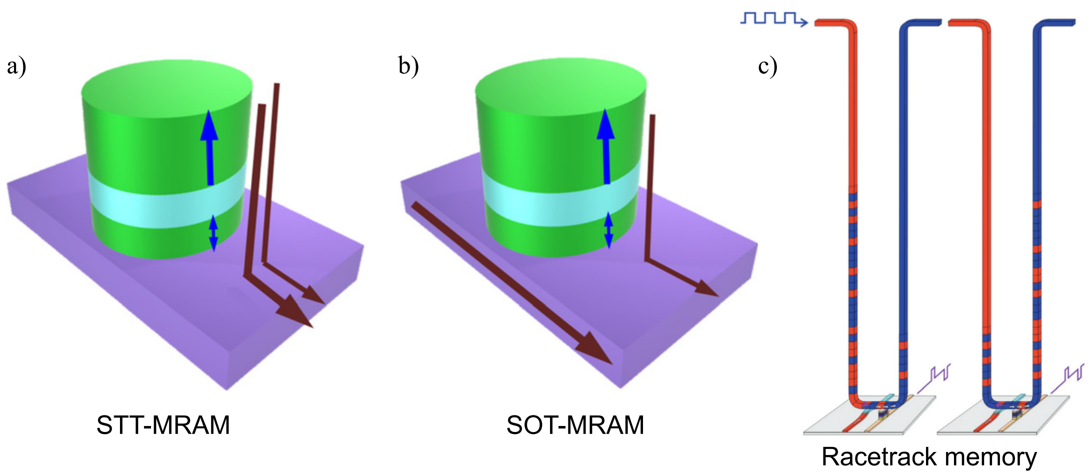

Figure 1.1: (a) A magnetic tunnel junction (MTJ) used as a spin-transfer-torque-based memory. Readout is done via tunnelling magnetoresistance between the fixed (top) and free (bottom) magnetic layers. Writing is done by using a high current to exert a spin transfer torque capable of switching the free layer. (b) A spin-orbit torque MTJ. Readout is the same as in (a), but spin-orbit torques produced by running current through a heavy metal layer cause the free layer to switch. (c) A racetrack for magnetic domain memories. Readout and writing are performed using a MTJ in the middle of the racetrack, while currents running through the length of the track push the domains forwards or backward to address individual bits. (a) and (b) are reprinted with permission from [16], (c) with permission from [17].

magnetization of the free layer. Calculations done independently by Slonczewski [18] and Berger [19] in 1996 predicted that such a torque would be sufficient to induce spontaneous auto-oscillations of the magnetization by overcoming the intrinsic damping of the magnetic dynamics. Moreover, complete switching of the free layer between parallel and anti-parallel states could be achieved using feasible currents in nanoscale devices [20].

These findings generated strong research interest in large part due to commercial applications in information storage, as switching torques capable of writing magnetic memory bits can be more spatially localized and efficiently driven compared with field torques generated by induction loops or nearby wires. Using STT to control and TMR to readout the free-layer magnetic state, spin-valve-based MRAM devices can be realized to create solid-state memories as shown in Fig. 1.1a [21]. More recently, spin-orbit torques have been proposed as a more efficient control mechanism than STTs (Fig. 1.1b), which we will cover in the next section.

Alternatively, the bit of information can be written instead to a subsection of a long nanowire, where the individual domain being addressed is localized to a point where a MTJ contacts the magnetic nanowire [17], as shown in fig. 1.1c. When a current passes through the length of the nanowire, STTs are exerted between adjacent domains and can move the domain walls with a velocity as high as 110 m/s [22]. This allows for solid state addressing of a very high density of magnetic bits, and the bits can in principle even be stored in a 3D array above the active layer allowing for greater densities [17].

1.1.3 Spin orbit torques

While STTs attracted interest for their ability to effectively localize spin currents within lithographically defined nanostructures, spin orbit torques (SOTs) proved to be a more promising prospect. With STT, the spin current and charge current are collinear such that each charge carrier can deposit at most one quantum of angular momentum as it passes the MTJ structure; SOTs apply torques by instead driving a spin current orthogonal to the charge current [23–25]. Heavy metals such as platinum and tungsten have large spin-orbit couplings, which causes a spin-dependent transverse force on charge carriers. Spins then drift in directions orthogonal to the charge current and spin polarization (the spin Hall effect), creating an associated spin current. In a normal wire, opposite spins simply accumulate on opposite sides of the wire, but this spin current can also apply spin transfer torques to attached magnetic elements (see Fig. 1.1b). The ratio between the perpendicular spin current (quanta of angular momentum per second) and the quanta of charge current flowing along the wire is the "spin Hall angle", and has been reported with typical values between 0.07 and 0.14 in Pt [26] up to 0.5 in AuT alloys [27].

SOTs can be more energy efficient than STTs because each charge carrier can deposit more than one quantum of angular momentum with each pass of the circuit. Additionally, the smaller switching currents afforded by SOTs helps to protect the device from degradation [28–31]. Because the charge and spin currents are orthogonal, once an electron scatters off the magnetic layer it is free to return to the heavy metal layer where the spin Hall effect can continue to deflect it back into the metal with the appropriate spin. Moreover, because the spin and charge currents are orthogonal, entirely new geometries of devices are made possible.

1.1.4 Spin torque oscillators

In addition to switching magnetic bits, spin currents can also apply damping-like torques that can effectively control the dynamics of magnetic oscillations. By injecting spins parallel to the equilibrium position, magnetic fluctuations can be reduced. Conversely, injecting spins anti-parallel to the equilibrium magnetization will produce anti-damping torques. When these torques overcome the intrinsic damping of the magnet, spontaneous auto-oscillations of the mode can "ring up", reaching a steady state limit cycle without the need to drive with an alternating current, thereby realizing a "spin torque oscillator" (STO) [32, 33].

In order to obtain the current densities required to overcome intrinsic damping – and to avoid Suhl instabilities that prevent large-angle, single-mode oscillations [34]– device sizes are necessarily limited to the order of 100 nm [35]. On the other hand, generation linewidths are typically limited by thermal phase noise and are inversely proportional to the auto-oscillator's energy [36], implying that higher quality factors can be obtained by increasing the number of participating spins. To overcome this challenge, oscillators made up of mutually synchronized STOs have been realized with Q $\approx$ 170 000 [37–40]. STOs have furthermore demonstrated the ability to inject spin waves into waveguides [41–44], a fundamental function for magnonic devices [45] which will be discussed in Section 1.1.6.

1.1.5 Parametric pumping

Anti-damping SOTs show great promise for their ability to generate and amplify spin waves [44,46,47], but are not unique in this function. Parametric amplification, or parallel pumping, has also emerged as an energy efficient method of controlling spin wave amplitudes with the added benefit of frequency selectivity and phase conservation over the signal [48]. In general, parametric pumping works by modulating a system parameter—e.g., the magnetic anisotropy [49–51], parallel fields [52–54], or spin currents [55]—at close to twice the natural frequency of oscillation. This provides intrinsic isolation between the pump and the signal and only drives modes that are set within a small tuning range set by the pump power, provided that it is above a critical threshold [48]. Parametric pumping can be used in combination with anti-damping SOTs in order to reduce the threshold pumping power, or to parametrically synchronize the auto-oscillation of STOs, thereby achieving smaller linewidths [55–57].

1.1.6 Magnonics and beyond

The ability to generate spin oscillations has ignited interest in using spin waves for computation. Propagating spin waves can carry information encoded in their amplitude and phase, and these signals can be processed by logic devices using interactions between input spin waves [6, 58]. The name "magnonics" refers to the development magnetic analogs of electrical circuitry based on magnetic spin waves, and takes the name from the quantum of spin wave excitation, the "magnon".

Magnetic waveguides allow magnons to propagate along their length, and careful selection of materials and interfaces gives designers a great deal of control over the permissible frequencies and bands of allowed modes. Magnonic crystals, for instance, can be integrated by applying a periodic structure to the waveguide, which allows for filtering and modulation of propagating spin waves [61–66]. Furthermore, devices have already been realized that can perform logical operations on spin wave inputs. NOT, NOR, NAND, XOR, and XNOR

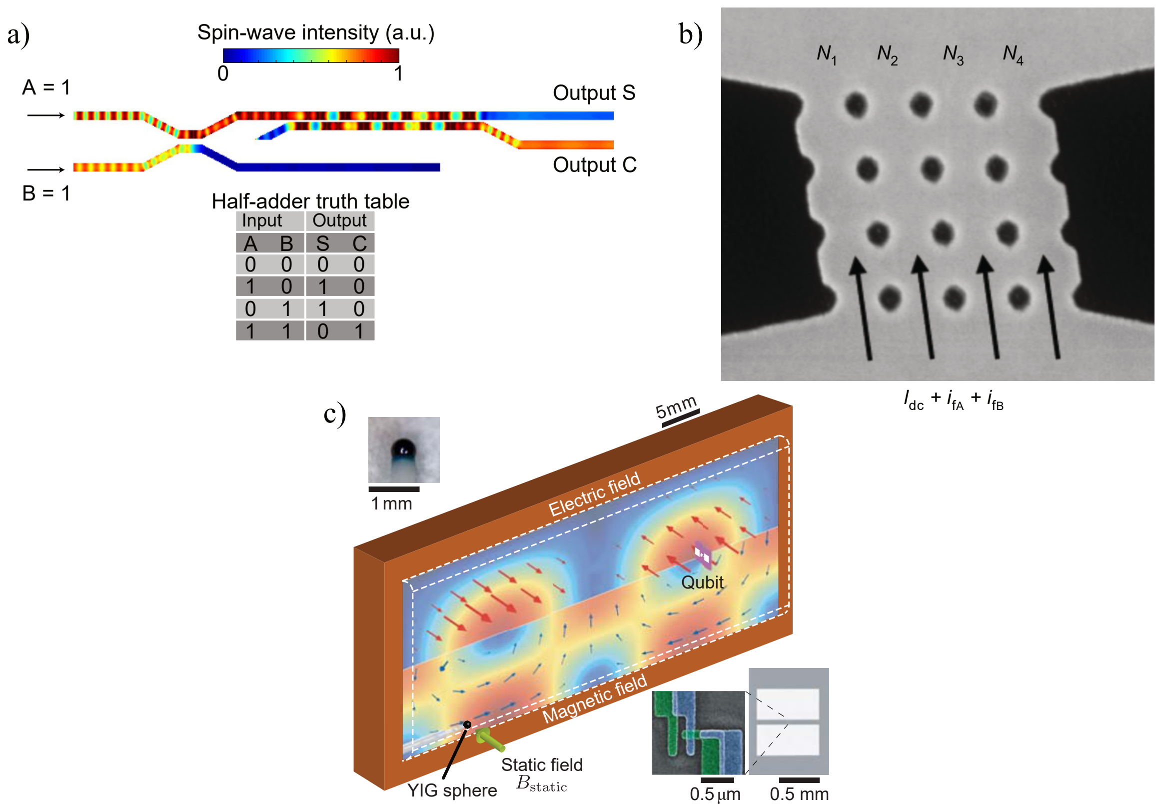

Figure 1.2: (a) A micromagnetic simulation of a magnonic half-adder design showing operation with two spin wave inputs. Interference at the directional coupler interfaces directs the resulting spin waves to outputs shown in the truth table. (b) SEM image of a 2D array of STO. Large spin currents funnelled between the gaps in the array create STOs that can synchronize with each other or with applied input microwaves, and can be used as spin-based “neurons”. (c) A microwave cavity enhancing the coupling between the occupation of a magnon mode in a YIG microsphere and the quantum states of a transmon qubit. (a) is reprinted with permission from [59], (b) with permission from [39], and (c) with permission from [60].

gates have been demonstrated on devices using interference in spin waves or electromagnetic waves [67–70]. All the components needed to build a spin-wave-based arithmetic logic unit have been demonstrated individually, and research is being conducted to develop the interconnects needed to demonstrate magnonic integrated circuits. Recently, a YIG-based magnonic half-adder was realized by using a directional coupler, as shown in Fig. 1.2a [59]. Although the half-adder was much larger than existing CMOS circuits accomplishing the same operation, micromagnetic simulations revealed that the design could be scaled down to require an order-of-magnitude less energy per operation than the electronic counterpart.

Spin-based devices offer a feasible way to implement novel computing methods as an alternative to the prevailing von Neumann architecture. Neuromorphic computing, for instance, takes inspiration from organic brains to create purpose built machine learning hardware [71–73]. As a basic demonstration of this, STOs have been shown to be capable of performing vowel recognition using mutual synchronization (see Fig. 1.2b) [39, 74]. Furthermore, STOs can act as “neurons”, while MTJs with a movable domain wall in the free layer can act as “synapses” with modifiable weights [75–78]. Connecting these together can enable hardware to implement spiking neural networks [79, 80]. These systems can be more efficient than existing hardware in running machine learning algorithms, and moreover can allow for the development of entirely new algorithms that may unlock far greater power than those written for deterministic architectures.

Finally, we note that while development of magnonic computers benefits from the ability to operate at room temperature, there is nothing preventing their use in the milliKelvin regime where the thermal magnon occupancy vanishes. This offers great extensibility to spin-based platforms, as the architecture offers another way of interconnecting the many studied quantum computing platforms [81]. Figure 1.2c shows one such example has already been performed, where superconducting qubits have been entangled with the magnon modes of a YIG microsphere when coupled via a microwave cavity [60, 82].

1.2 Methods for characterizing spin waves

There exist many methods for spin-wave detection based on entirely different physical approaches. The most common methods for spin-wave detection are based on transducing magnetic dynamics into an electric voltage using microwave circuits [83]. We already showed in Section 1.1.1 that magnetoresistance in metallic systems can be used to detect spin states; in the case of spin waves, this leads to oscillating resistance. Mixing with an oscillating current drive leads to a static voltage measured in the case of spin-transfer ferromagnetic resonance (ST-FMR) [26, 84, 85]. In the case of STOs, voltage oscillations arising from resistance mixing with bias currents can be detected with a microwave spectrometer [32, 85, 86]. These techniques can be implemented with little overhead and provide insight into the time and frequency response; however, the voltage measures the global magnetoresistance of the device and thus cannot reveal the spatial distribution of the dynamics.

Resistive readout is not possible in insulating magnets such as YIG, therefore other methods have been developed to probe spin waves in these systems. By fabricating an antenna over a magnetic waveguide, spin waves can be excited by current-induced fields [87–93] or detected by field-induced currents [93, 94]. In Section 1.1.3 we discussed how the spin Hall effect can send spin currents into magnetic layers to drive spin waves; the *inverse* spin Hall effect can be used to measure voltages caused by spin accumulation at a magnet/heavy metal interface [95–99]. These techniques are most sensitive to magnons that have the same wavelength as the antenna or device is wide. Because the detector is set by the manufacturing step, many samples with varied detector geometries are needed to measure magnons over a wide range of wave numbers [93].

Microscopy techniques based on magneto-optic effects allow for spin-wave detection with spatial imaging. The time-resolved magneto-optic Kerr effect (TR-MOKE) [100–102] is a method that detects the small rotation in the polarization of a light beam as it is reflected off a magnetic surface. By using pulsed laser sources and sweeping the delay between the magnetic and optical excitations, a series of snapshots of the magnetic surface with small temporal resolution is obtained. Another method called Brillouin light scattering (BLS) is a spectroscopic technique in which light is reflected off a magnet and the photons that scatter off of magnons and experience a shift in frequency equal to that of the magnon that is created or annihilated in the process [103–105]. Sending the scattered light to an interferometer measures the intensity of light as a function of magnon frequency, typically with a resolution in the tens of MHz [104]. Time-gating the analysis allows for the magnetic dynamics to be temporally resolved, though not with the same precision as TR-MOKE. BLS has been used to measure magnons subjected to spin-currents [39, 55, 106] and parametric pumping [53, 55]. The main limitations of TR-MOKE and BLS are the requirements for optical access to the magnetic material, as well as the spatial resolution of ~ 100 nm determined by the diffraction of light.

We note that there is continuous development in the space of magnon detection; over the last decade, the use of single electron spins to detect stray fields from magnetic materials has become an attractive candidate. These measurements are inherently non-invasive and can achieve greater spatial resolution via nanopositioning than optical diffraction allows. By far the most studied single spin detector—and the one presented in this thesis—is the nitrogen-vacancy centre in diamond [107]; a detailed description of this probe is presented in the following section.

1.3 Principles of nitrogen-vacancy magnetometry

The nitrogen-vacancy (N-V) centre in diamond has remarkable properties that have brought it to the forefront of research in nascent quantum technologies. The colour centre is an optically addressable point-like electronic spin system with excellent coherence properties, even at room temperature [107–109] These properties, coupled with the hardiness of diamond as a host material, have attracted much attention to the system for its potential in quantum metrology. At cryogenic temperatures, its spin-dependent, atom-like optical transitions make it suitable for use as a quantum node in a larger qubit-based network [110].

Physically, the N-V is composed of a nitrogen atom substituting a carbon within the diamond lattice, next to a neighbouring vacancy defect, as shown in Fig. 1.3a. In its negatively charged state, six electrons occupy the dangling bonds around the vacancy. Although the neutral charge state is also a stable conformation for the N-V, only the negatively charged state has desirable spin coherence.

N-Vs occur naturally in most diamonds in abundance. They were originally studied in ensembles, while the first study to isolate an individual centre was published in 1997 [111]. Typically, the creation of high quality N-V centres starts with a CVD-grown single crystal diamond, which allows direct control of the host parameters, including intrinsic nitrogen content and the isotopic purity of the carbon. N-Vs can be created by irradiating the sample with an electron beam or with nitrogen ions [112–114], both of which cause damage to the crystal lattice. A subsequent annealing step undoes part of the damage and, in so doing, allows vacancy defects to move towards energetically favourable pairings adjacent to embedded nitrogen.

Magnetometry with N-Vs can be performed under many modalities in order to detect dc or ac fields [109, 115]. Depending on the application, homogeneous fields can be measured using an ensemble of N-Vs to leverage $1/\sqrt{N}$ sensitivity scaling [116–118], but the system is especially useful when measuring nanoscale fields using a single isolated N-V center. Due to their point-like nature, N-Vs can be placed within tens of nanometers of the samples studied. This can be accomplished most simply by applying a layer of nanodiamonds directly to the sample being studied [119–121], as shown in Fig. 1.3b. Nanodiamond magnetometry suffers from impaired sensitivities as fluctuations from charges and paramagnetic impurities on nanodiamond surfaces lead to worsened decoherence rates [122]. The approach taken in this thesis is shown in Fig. 1.3c, which involves instead building the sample to be studied directly on a single-crystal diamond chip. If fabrication on diamond is not feasible for the chosen process or material, diamond nanobeams containing N-Vs with bulk-like properties can be manufactured and placed on the sample instead [123, 124], as shown in Fig. 1.3d. These methods all achieve stochastic lateral placement of the sensor, but with more effort, diamond-tip cantilevers [125,126] can be engineered and placed on an atomic force microscope platform to achieve precise and deterministic positioning of the sensor (Fig. 1.3e).

1.3.1 State preparation and readout

The energy levels of the negatively charged N-V are shown in Fig. 1.3f [107]. The electronic ground and excited states are separated by 1.945 eV [128]. Optically pumping the N-V can

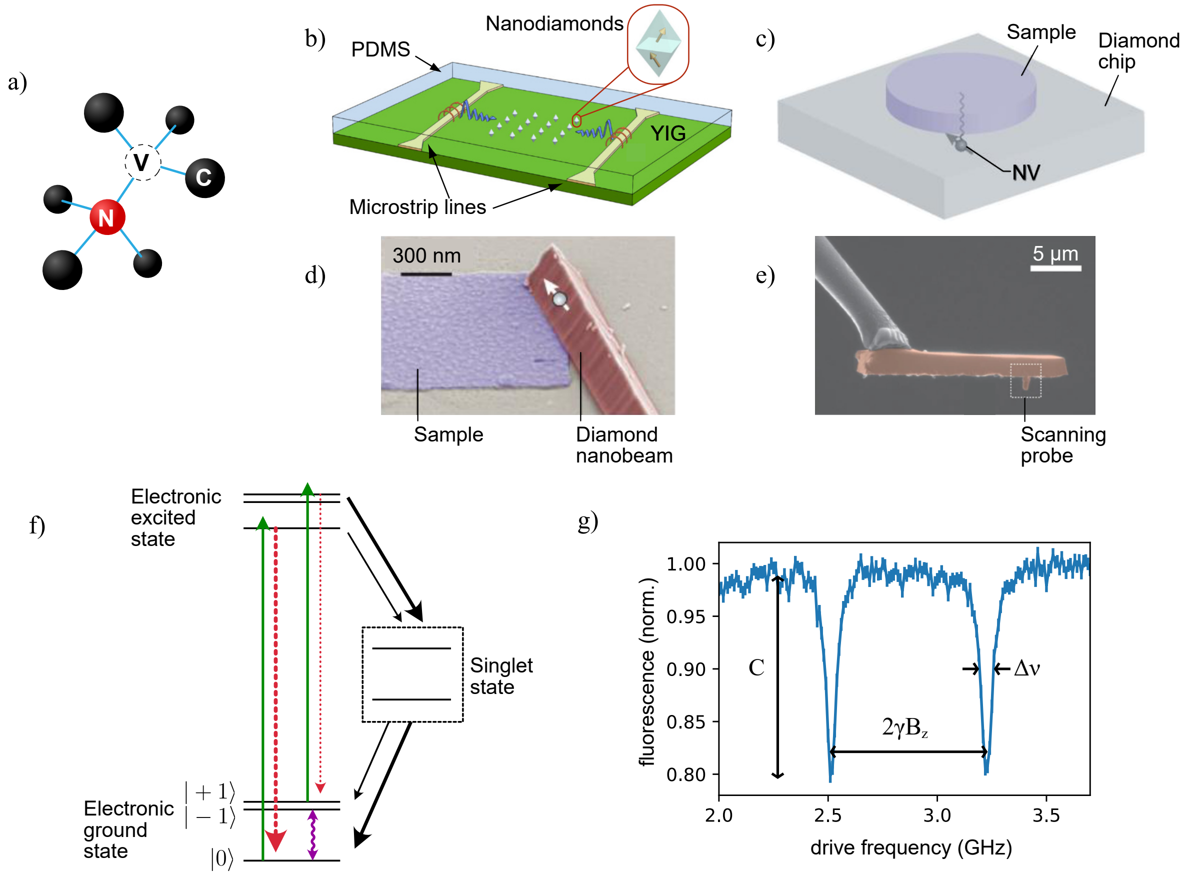

Figure 1.3: (a) The atomic structure of a nitrogen-vacancy centre in diamond. Neighbouring carbon atoms are replaced by a single nitrogen atom and a vacancy. (b-e) Different modalities for interfacing N-V centers with magnetic samples. (b) Placing N-V-containing nanodiamonds on top of the sample, in this case by using a PDMS stamp. (c) Fabricating the sample directly on a diamond substrate, and probing N-Vs found in a near-surface layer. (d) Fabricating diamond nanobeams with anisotropic ion-beam milling and placing them on the sample. (e) Fabricating diamond nanopillars and mounting them on scanning-probe systems in order to exert precise spatial control of the probe. (f) Energy level structure of the N-V. Green arrows indicate optical pumping, red arrows indicate fluorescent decay, black arrows indicate non-radiative decay channels, and the purple arrow indicates spin mixing produced by driving a microwave field resonant with the transition. (g) Typical CW-ODMR measurement. When a static magnetic field is applied, the Zeeman effect lifts the degeneracy between the $|0\rangle \leftrightarrow |-1\rangle$ and $|0\rangle \leftrightarrow |+1\rangle$ transitions, separating their frequencies by $2\gamma B_z$. The contrast C and linewidth $\Delta\nu$ is set by the excitation parameters of optical and microwave drives [115]. (b) is reprinted with permission from [121], (c) and (d) with permission from [127], and (e) with permission from [126].

be accomplished using above-resonant excitation (e.g., with 532 nm light from a laser diode, as performed in this body of work) by exciting the phonon sideband [129, 130]. This puts the N-V in an excited state with a lifetime of $\sim$ 12 ns [131], which then decays back to the ground state either radiatively by emitting a fluorescent photon or nonradiatively by entering a metastable spin singlet state.

Spin-dependent shelving rates from the excited state into the spin singlet enable simple spin initialization and readout mechanisms. Specifically, the shelving rate from the $|\pm 1\rangle$ states is about ten times greater than that from the $|0\rangle$ state, while the decay rates out of the singlet states back to the ground are comparatively slow [132]. This sets up a situation where optical cycling of the $|\pm 1\rangle$ states leads to decreased fluorescence compared to optical cycling of the 0 state, allowing fluorescence-based state readout with $\sim 30\%$ contrast. Furthermore, the process of optically cycling the centre preferentially polarizes the N-V into the $|0\rangle$ state via the same singlet state decay path.

Although the experimental simplicity of fluorescence-based state readout allows it to be easily implemented using confocal microscopy, it comes with the drawback that single-shot readout is impossible and measurements must be performed repeatedly to achieve a useful signal-to-noise ratio. Alternative methods of spin-state readout have been proposed and tested to improve the system, each with the goal of improving readout sensitivity. These include measuring photoelectric currents through diamond mediated by the N-V [133], measuring infrared light absorption between the singlet states [134], and using spin-to-charge conversion [135, 136].

1.3.2 Optically detected magnetic resonance

A major benefit of N-V magnetometry is that the spin dynamics are set by physical constants, meaning that no drift-susceptible calibration is needed to back out the field from measurement. When neglecting strain, electric field, and hyperfine interactions, the ground state spin Hamiltonian for the N-V is [107, 109]

$$\mathcal{H} = hDS_z^2 + h\gamma \mathbf{B} \cdot \mathbf{S}, \tag{1.1}$$

where $D = 2.88$ GHz is the zero field splitting, $\mathbf{B}$ is the magnetic field vector, $\mathbf{S} = [S_x, S_y, S_z]$ are the spin matrices, and h is Planck's constant, and $\gamma = 28$ GHz/T is the gyromagnetic ratio for the N-V spin. S_z is set by the symmetry of the defect, such that we lift the degeneracy between $|\pm 1\rangle$ and recover the linear Zeeman energy shifts when we apply fields along the N-V bond axis.

Microwave fields can drive transitions between states separated by a single quantum number when they have a non-zero projection on the transition dipole. Optically detected magnetic resonance (ODMR) is performed by measuring the fluorescent signal from the N-V to detect the spin transitions. A typical continuous-wave (CW) ODMR scheme involves optically pumping an N-V while applying a microwave tone and sweeping its frequency; the observed fluorescence of the emitter exhibits Lorentzian dips corresponding to the resonance frequencies of the spin transitions (see Fig. 1.3g). The separation between dips is equal to $2\gamma B_z$, where the subscript z indicates that the field is along the N-V axis. Measurement of this separation thus amounts to a direct observation of a component of the local magnetic field, although large off-axis fields can complicate this interpretation [109].

1.3.3 DC field measurements

When CW-ODMR is performed, static magnetic fields can be detected with a single N-V sensitivity of approximately [109, 115]

$$\eta_B \approx \frac{\Delta\nu}{\gamma C \sqrt{\mathcal{R}}}, \tag{1.2}$$

where C is the contrast of the fluorescence dip, $\Delta\nu$ is the associated linewidth, and $\mathcal{R}$ is the rate of detected fluorescence photons (see Fig. 1.3g). C and $\mathcal{R}$ are limited by the competition between the optical and microwave pumping rates and the multichannel decay rates of the N-V electronic structure; $\Delta\nu$ is limited by the inhomogeneous spin dephasing rate Γ_2^*, the microwave Rabi frequency Ω_R, and optically induced spin decoherence [115]. The best achievable CW-ODMR sensitivity for a single N-V in a typical setup was found to be $\eta_B \approx 2\ \mu\mathrm{T}\cdot\mathrm{Hz}^{-1/2}$ [115].

ODMR techniques can be improved beyond the CW limit by using a variety of pulse sequences at the cost of increased complexity. By separating the optical spin polarization pulse from the microwave π-pulse used to manipulate the spin, the competition between contrast and power broadening can be eliminated. Thus, when the π-pulses have been properly calibrated, pulsed ODMR can achieve an order of magnitude improvement in sensitivity over CW-ODMR [115]. Alternatively, instead of a single π pulse, sensitive dc magnetometry can be achieved using a Rasmey sequence consisting of two $\pi/2$ pulses separated by a phase evolution delay [137, 138].

1.3.4 AC field measurements

Pulsed measurements can also be used to detect oscillating magnetic fields with sensitivity even better than that in DC operation. The simplest such pulse sequence is the Hahn echo, which is performed by inserting a π pulse in the middle of a Ramsey sequence [139, 140]. Using a periodic train of π pulses within the Ramsey sequence, such as in CPMG [141, 142], the dephasing rate can be dramatically reduced from an inhomogeneous value of $\Gamma_2^* \approx 2 \times 10^5$ s^{-1} to the homogeneous value of $\Gamma_2 \approx 500\ \mathrm{s}^{-1}$, and correspondingly can attain AC single-N-V sensitivities of $\eta_{B,\mathrm{AC}} \approx 10\ \mathrm{nT} \cdot \mathrm{Hz}^{-1/2}$ [109]. This decoupling mechanism effectively performs a quantum lock-in measurement and is therefore sensitive only to AC fields [143].

The frequency range of this lock-in scheme is bounded at the lower end by Γ_2, while at the higher end the limit is set by the pulsing rate and thus by Ω_R [144]. Practical considerations mean this is typically limited to the tens of MHz. Higher frequency fields can still be probed if they are made resonant with the N-V transitions, allowing for measurement of Ω_R and therefore the component of the field driving the dipole transition [145], though we note that the resonant nature of this scheme is narrow in bandwidth.

1.3.5 Spin relaxometry

In addition to measuring magnetic fields via ODMR, N-V centres can also sense GHz magnetic power spectral densities by observing changes in the longitudinal relaxation rate Γ_1 [146, 147]. Specifically, the relaxation rate depends on the spectral density $S_\perp$ along the affected dipole moment as [148]

$$\Gamma_1 = \frac{\gamma^2}{2} S_\perp. \tag{1.3}$$

The 0 to +1 and 0 to −1 transitions are each sensitive to the power spectral density at their respective frequencies $\nu_\pm$. The typical method for measuring this relaxation is to initialize the N-V spin state using an optical pulse (followed by an appropriate π-pulse if initializing into $m_s = \pm 1$), waiting a variable time τ, and then reading out the spin state population with a second optical pulse. Fitting the decay signal to an exponential model then allows the estimation of Γ_1 for each transition. The relaxation rate is measurable between the intrinsic relaxation rate of $\Gamma_1 \approx 60$ Hz and the maximum detection limit set by the optical polarization rate of ~ 2 MHz. This large orders-of-magnitude dynamic range can make decay measurements quite slow without prior knowledge; therefore, some effort has been made to incorporate Bayesian inference models to speed up the measurement [149].

1.4 N-V probing of nanomagnets

Now that we have covered the basics of how N-V sensing works, we focus on the application of these methods to the probing of nanomagnetic systems. We divide this into two broad topics of interest, namely the detection of spatial textures and the detection of magnetic dynamics. The latter leads naturally to the work described in this thesis; however, understanding the methods for spatially resolving features is important to contextualizing the future directions in which research can be conducted.

1.4.1 Detecting spatial textures

By correlating spatial information along with the ODMR signals, N-V magnetometry can enable much richer measurement of magnetic textures. By using widefield microscopy techniques on ensembles of N-Vs, either by implanting a dense layer into a diamond substrate or by applying a coating of nanodiamonds [150], a 2D magnetic field map can be reconstructed a short distance from the target sample. This map is resolution-limited to approximately 300 nm by the point spread function of fluorescent light, but improvements can be made by instead using a diamond tip containing a single N-V centre mounted on a scanning probe to scan the sample [126]. While these systems can be positioned with sub-nanometer precision, the resolution with which underlying structures can be mapped is dependent on the sample-probe distance, which is currently limited to about 50 nm [127, 151]. Once the field has been fully mapped, an inversion problem remains to extract the structure of the underlying magnetization or currents. If the field is produced by a layer of currents, the currents can be uniquely reconstructed using only a single component of the mapped magnetic field [127]. However, the inversion problem for 2D magnetic textures is under-constrained, as an arbitrary number of magnetization maps can give rise to any given field, and thus a solution can only be obtained by gauge fixing. This example is shown in Fig. 1.4a, where the measured magnetic field above a skyrmion can be reconstructed into two equally valid conformations of the magnetization [152], as seen in panels iii. and iv. Only by applying additional constraints to the inversion can a unique solution be found. In the case of the skyrmion studied, the reconstruction in Fig. 1.4a-iv. is ruled out because the topology requires a discontinuity and is considered unphysical.

Similar reconstruction techniques have allowed for the imaging of electric currents flowing through carbon nanotubes [153]. Using widefield imaging of N-Vs below a flake of graphene, Tetienne et al were able to image the current flowing around defects in the flake [154]. Further experiments on graphene were able to observe a breakdown in the current flow from Ohmic to a viscous fluid-like behaviour [155, 156]. Likewise, the hydrodynamic flow of electrons was observed in WTe_2 at 20 K using scanning N-V magnetometry [157]. Low temperature scanning probe measurements over a superconductor were also able to make quantitative measurements of Pearl vortices [158].

A wide array of magnetic textures has also been imaged using similar techniques. Domain walls in thin magnets have been imaged to help determine their structure [161–163]. Imaging of chiral textures in $BiFeO_3$ [164, 165], vortex cores [166, 167] and skyrmions [152, 168, 169] is also possible. Van der Waal structures have been observed, allowing measurement of the magnetisation of CrI_3 [170] and $CrTe_2$ [171] monolayers. Defects in magnetic nanowires have also been studied for their relevance in spintronic circuits [172]. Furthermore, performing AC ODMR can allow for a more sensitive approach to scanned imaging by taking advantage

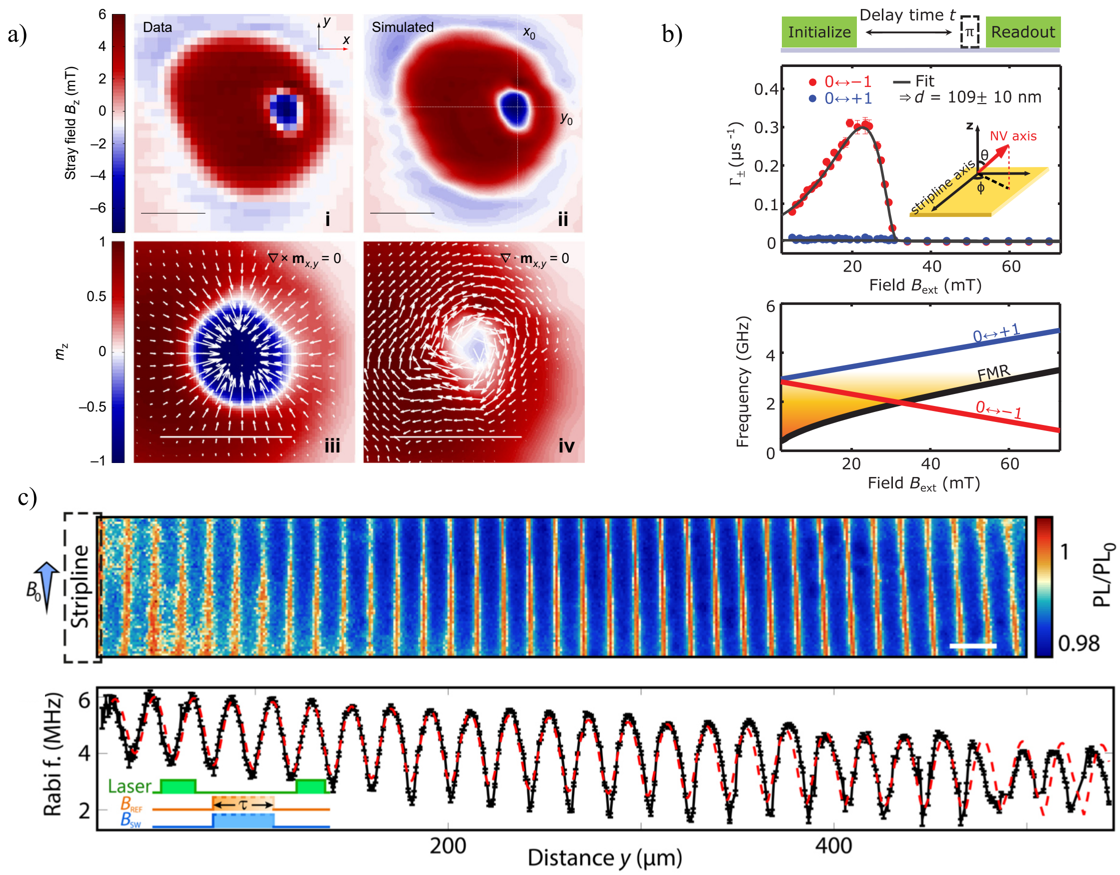

Figure 1.4: (a) Measurements and reconstruction of a skyrmion spin texture. Panel i. shows an N-V scanning probe measurement of one component of the stray magnetic field. Panel ii. shows the simulated field from the reconstructed magnetization. Panels iii. and iv. show two valid reconstructions of the underlying magnetization, obtained by fixing with the Néel (iii.) or Bloch (iv.) gauges. All scale bars are 500 nm (b) Spin relaxometry measurements of thermal magnons in a YIG sheet by an N-V embedded in a diamond nanobeam as the applied field is swept. Top panel: the relaxation rates measured for the $|0\rangle \leftrightarrow |-1\rangle$ ($|0\rangle \leftrightarrow |+1\rangle$) transitions in red (blue). The black line shows a fit to the known spin wave dispersion and thermal occupation, which allows for extraction of the separation distance between the YIG sheet and the N-V. Bottom panel: a graphical representation of N-V ODMR frequencies in red and blue which probe the spin wave spectrum that exists above the ferromagnetic resonance in black. (c) Measurement of a propagating spin wave in a sheet of YIG. Top panel: confocal imaging of a dense layer of N-Vs is sensitive to the interference pattern between the local stray field from the YIG sheet and a spatially homogeneous reference drive, revealing a propagating coherent spin wave. Scale bar is 20 μm. Bottom panel: Rabi frequency versus distance from stripline. The data (black) is measured using the pulsed ODMR sequence shown. The red line is a fit to a model of the field from the stripline, the spin-wave field, and the reference field. (a) is reprinted with permission from [152], (b) with permission from [159], and (c) with permission from [160].

of the large field gradients when oscillating the N-V scanning probe tip at the same rate as the quantum lock-in [173].

1.4.2 Detecting spin dynamics

Beyond the detection of static structures, N-V magnetometry has been used to observe a multitude of spin dynamics. By driving large-angle ferromagnetic resonance (FMR), the time-averaged magnetization can be reduced and measured by the change in ODMR frequencies of a proximal N-V [174]. Likewise, applying static fields to a magnetic disk can reposition vortex cores, which can strongly change the ODMR spectra [119]. FMR can also directly drive ODMR when both processes are tuned to the same frequency [174, 175]. However, what is more curious is that off-resonant FMR (in extended films) can also drive ODMR as long as the N-V frequencies are higher than those of the excited spin dynamics [176–178]. This suggests that spin-wave mixing can upconvert the excited fundamental mode into modes that are resonant with the N-V [179], consistent with the Suhl instability [34]. More recently, longitudinal spin fluctuations have also been predicted [180] and experimentally demonstrated [179,181] to have driven N-V spin relaxation even when the transition frequencies of the latter are below the magnon band minimum.

The thermal fluctuations of these modes can also be detected via spin relaxometry without any external microwave drive. The top panel of Fig. 1.4b shows the measured relaxation rates of an N-V spin in a diamond nanobeam positioned on a layer of YIG [159]. As the field is swept, the frequencies of the magnetic modes and the N-V transition frequencies change. A peak in the measured relaxation rates occurs when ν_- is just above the fundamental FMR mode, roughly where the magnon density of states is highest (see the bottom panel of 1.4b). Because the alternating fields rapidly average to zero at a far distance, the N-V is most sensitive to magnons that have wavevectors equal to the inverse of the probe-to-sample distance. This spatial filtering allows for the probe distance to be estimated as a fitting parameter of the relaxometry sweeps.

The dynamics of magnetic devices subjected to spin currents has also been investigated with N-Vs. In complement to the metallic systems studied in this thesis, by driving DC spin currents into a YIG magnetic insulator, relaxometry measurements were able to observe changes to the spin chemical potential of resonant magnon modes [159]. Spin currents have also been shown to control the amplitude of driven spin wave modes, effectively tuning the amplification of the microwave magnetic field [182]. Furthermore, by reducing the lateral dimension of the YIG and injecting spin currents, spin torque oscillations were confirmed by abrupt changes at critical current values in the relaxation rate of the N-V and the ODMR frequency due to large angle oscillations when no microwave drive was present [183]. Relaxometry measurements also observed the effects of voltage-controlled magnetic anisotropy over the thermal dynamics of a MTJ [184]. Magnons driven by thermal gradients have also been detected by relaxometry measurements [185], further demonstrating the versatility of the technique.

The detection and imaging of propagating spin waves is also of great importance to developing new tools of study. By placing nanodiamonds in an array on top of a layer of YIG and exciting a stripline with microwaves, resonant spin waves were seen to travel long distances and excited ODMR [121]. A similar measurement was then made using ensembles of N-Vs in a diamond substrate, where the field of the excited spin waves interferes with the Oersted field from the stripline to produce a periodic pattern in the measured fluorescence and Rabi frequency to reveal coherent spin waves [160, 186] (see Fig. 1.4c). Scanning-probe-based measurements of injected spin waves have since improved the resolution of such schemes [187], allowing direct imaging of spin wave dispersion [188,189], filtering effects based on probe height [189], and spin wave scattering off of magnetic targets [188].

1.5 Overview

The work presented in this thesis uses N-V magnetometry to study metallic systems in which we control the magnetic dynamics using spin currents. We demonstrate parametric pumping and spin orbit torque antidamping of magnetic normal modes using a permalloy/platinum (Py/Pt) nanowire; we detect these effects using a combination of ODMR and spin relaxometry with an N-V and contrast these against conventional ST-FMR measurements. We show N-V coupling to large-angle dynamics of multiple, unresolved modes driven by spin currents and measure a decrease in magnon temperature down to ~ 150 K (Chapter 2). By modifying the fabrication process, we realize a spin torque oscillator using a smaller device; parametric pumping allows us to synchronize the auto-oscillation and resolve individual modes of oscillation (Chapter 3). These findings complement similar studies conducted on YIG in parallel [159,183], noting that Py may be more relevant for industrial applications due to the ease of integration into nanofabrication.

Chapter 2

Probing a spin transfer controlled magnetic nanowire with a single nitrogen-vacancy spin in bulk diamond

Adrian Solyom[†,*], Zackary Flansberry[†,*], Märta A. Tschudin[†], Nathaniel Leitao[†], Michel Pioro-Ladrière[‡,||], Jack C. Sankey[†], and Lilian I. Childress[†]

[†] Department of Physics, McGill University, Montreal, Quebec H3A 2T8, Canada

[‡] Institut Quantique and Département de Physics, Université de Sherbrooke, Sherbrooke, Quebec J1K 2R1, Canada

[||] Quantum Information Science Program, Canadian Institute for Advanced Research, Toronto, Ontario M5G 1M1, Canada

[*] *These authors contributed equally to this work*

This chapter was first published in ACS Nano Letters, reprinted here with permission.
Citation: Nano Lett. 2018, 18, 10, 6494–6499

This work is motivated by recent advances in spin-current control of magnonic devices and the challenges involved in the design and characterization of these systems [100,105,190]. As we saw in Section 1.2, measurements based on resistive readout are inherently non-local, while techniques such as TR-MOKE and focused BLS have diffraction-limited spatial resolution. The development of single-spin sensing protocols is thus desirable because of the potential for high spatial resolution, sensitivity to spin waves with large wavevectors, and non-invasive detection. We chose to use a nitrogen-vacancy (N-V) center in diamond as our probe of choice due to its maturity as a solid-state spin system and its excellent field sensitivity even at room temperature [107–109]. This meant that we could non-invasively probe the local magnetic features of nanocircuits built directly on diamond using a simple home-built confocal microscope aparatus, with no vacuum or low-temperature requirements.

At the time that this work was being conducted, N-V probing of ferromagnetic modes had been demonstrated in extended sheets of low-dissipation Yttrium-Iron-Garnet (YIG) [176] and circular permalloy (Py) micromagnets [174]. Other various magnetic systems have also been investigated using N-Vs such as ferromagnetic insulator nickel zinc aluminum ferrite [179], organic ferrimagnet V[TCNE]$_x$ [191], cobalt and cobalt manganese iron germanium [177]. We wished to extend the N-V detection methods to probing spin-current controlled devices. Our system, a permalloy/platinum bilayer nanowire, was designed so that the heavy metal Pt layer could apply strong spin-orbit torques to the metallic Py layer. Anisotropic-magnetoresistance-based transport measurements meant that we could compare observations made with N-Vs to standard device calibrations, a feature lacking in similar measurements of a YIG/Pt bilayer [159]. We used spin-transfer ferromagnetic resonance measurements in a manner shown in Fig. 2.1 and described elsewhere in detail fig: [84]. By comparing these conventional measurements to the fluorescence data we obtained from the proximal N-V, we were able to validate our understanding of the features seen in the latter.

We performed optically detected magnetic resonance measurements of the device's stray field as it was parametrically pumped, allowing for a measurement free of crosstalk from the drive, which was isolated in frequency. This allowed us to detect the bias-induced antidamping threshold required to observe parametrically driven large-angle oscillations. Additionally, we measured magnon occupation in the absence of any microwave driving using spin relaxometry techniques [159, 174, 192]. Previous measurements using BLS had seen strong cooling in Py/Pt systems [193], and our experiment characterized a similar system using an N-V; the use of diamond as a substrate gave us excellent thermal management, allowing us to reach colder temperatures.

Author contributions

Adrian Solyom: Contributed equally to the experimental design with Zackary Flansberry. Acquired and analyzed the transport and N-V data, and wrote the manuscript.

Zackary Flansberry: Contributed equally to the experimental design with Adrian Solyom. Developed the nanofabrication process for patterning and connectorizing nanowires on diamond and built the transport acquisition apparatus for ST-FMR measurements.

Märta Tschudin: Acquired and analyzed $g^{(2)}(\tau)$ measurements; also assisted with other measurements and analysis.

Nathaniel Leitao: Contributed to micromagnetic simulations of the device.

Michel Pioro-Ladrière: Contributed to the initial conception of the experiment with Jack Sankey and Lilian Childress.

Jack Sankey: Co-supervised the project with Lilian Childress. Contributed to the initial conception of the experiment with Michel Pioro-Ladrière and Lilian Childress, and revised the manuscript. Developed thermal simulations for the current calibration and single domain simulations for validating the parametric ST-FMR.

Lilian Childress: Co-supervised the project with Jack Sankey. Contributed to the initial conception of the experiment with Michel Pioro-Ladrière and Jack Sankey, and revised the manuscript. Developed models for calibrating the external field and for parameter estimation of the spin relaxometry data.

Abstract

The point-like nature and exquisite magnetic field sensitivity of the nitrogen vacancy (NV) center in diamond can provide information about the inner workings of magnetic nanocircuits in complement with traditional transport techniques. Here we use a single NV in bulk diamond to probe the stray field of a ferromagnetic nanowire controlled by spin transfer (ST) torques. We first report an unambiguous measurement of ST tuned, parametrically driven, large-amplitude magnetic oscillations. At the same time, we demonstrate that such magnetic oscillations alone can directly drive NV spin transitions, providing a potential new means of control. Finally, we use the NV as a local noise thermometer, observing strong ST damping of the stray field noise, consistent with magnetic cooling from room temperature to ∼150 K.

2.1 Introduction

In nanoscale magnetic circuits, spin transfer (ST) effects provide an efficient means of all-electronic control, prompting the development of ST-based non-volatile memories, microwave-frequency oscillators, filters, detectors, and amplifiers [194, 195]. These developments call for new tools to understand the interplay between spins, magnons, and the environment. In parallel, the nitrogen-vacancy (NV) center in diamond [196] has emerged as a versatile sensor for studying magnetic systems, with excellent spatial and spectral resolution [197, 198]. The tiny magnetic moment of a single spin provides a non-invasive probe of local stray fields, and can be combined with scanned-probe [199] or subwavelength imaging [200] techniques to achieve nanoscale spatial resolution. Moreover, the NV offers a variety of sensing modalities appropriate for DC and AC magnetic fields [201, 202] or noise spectroscopy [203–205]. Recently, NV centers have probed ferromagnetic phenomena including vortex cores [206, 207], domain walls [208], ferromagnetic resonance (FMR) [209–213], and magnetic thermal quantities in an extended YIG film [213] modified by ST effects.

Here, we probe a metallic ST-controlled ferromagnetic nanowire with a single NV in bulk diamond. Different from microwave-frequency magnetoresistance readout [214–216], the

NV's point-like nature enables coupling to shorter-wavelength spin waves, thereby revealing qualitatively new features. First, we provide transport-based evidence of parametrically-driven magnetic oscillations – tuned through threshold with spin transfer anti-damping – and use the resulting (phase-locked) stray field oscillations *alone* to drive the NV spin resonance.

This removes any ambiguity from the interpretation of the transport measurements, and provides a potential new means of NV control. Additionally, transport readout indicates a precession angle up to $\sim 55°$, suggesting the absence of Suhl-like (multi-magnon) instabilities [217–219], which we tentatively attribute to the reduced density of states in our confined geometry. The observed changes in field at the NV independently corroborate the estimated angle, and (more importantly) we observe no signs of non-resonant NV spin flips in the PL spectra when directly driving FMR – a feature normally appearing in extended magnetic films [209–213] – providing additional evidence of suppressed multi-magnon instabilities. This observation suggests the NV's potential as an additional tool to illuminate the interplay between confinement and multi-magnon processes [220–222]. Finally, we demonstrate strong ST control of the magnetic thermal fluctuations: adapting the NV noise relaxometry method of Ref. [213], we observe large ST damping of the stray field noise, providing evidence of magnetic cooling from room temperature to ~ 150 K. The observed noise suppression is orders of magnitude larger than measured with an NV near a YIG film [213], and a factor of ~ 2 larger than measured with Brillouin light scattering from a related metallic structure [106]. An interesting open question is the fundamental limits of this cooling technique, in particular if and from what temperature the ground state can be reached. Interestingly, our demonstrated NV sensitivity suggests it may be possible to resolve magnetic zero-point fluctuations, thereby providing an optically active "handle" on a macroscopic magnet in the quantum regime.

These techniques, which are especially advantageous in systems having low magnetoresistance, pave the way to a deeper understanding of short-wavelength magnons, ST effects, and quantum emitter control.

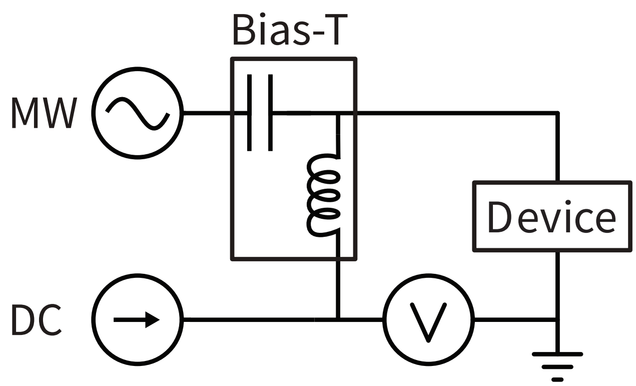

Figure 2.1: The magnetoresistive voltage V_{MR} is measured across the dc port of a bias-tee that is used to apply microwave and bias currents to the device.

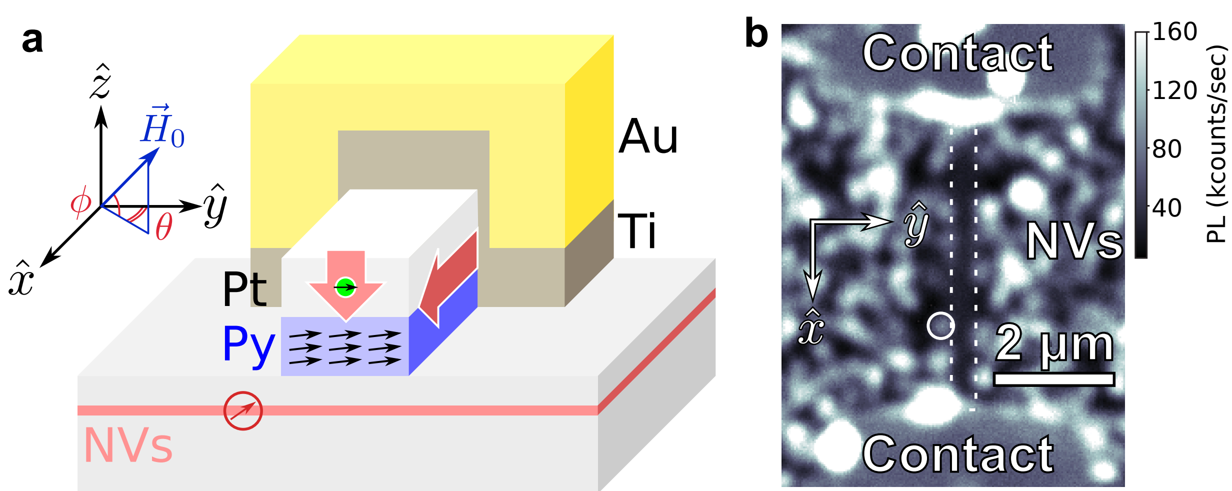

Figure 2.2: Device geometry. (a) Cross-section of nanowire on a diamond substrate with implanted NVs. Nanowire current (red arrow along $\hat{x}$) drives spins (green circle) polarized along $\hat{y}$ into the Py layer (red arrow along $\hat{z}$). (b) Confocal PL map of the device. The nanowire (dotted box) appears as a shadow. Circle indicates the NV under study.

2.2 Device Geometry

We fabricate [223] an 8-µm-long × 417-nm-wide (average, with ∼20 nm edge roughness) Py ($Ni_{81}Fe_{19}$, 10 nm) / Pt (10 nm) multilayer nanowire on electronic grade diamond with a layer of NVs implanted 60 ± 15 nm below the surface, as shown in Fig. 2.2(a). Figure 2.2(b) shows a photoluminescence (PL) image of the device pumped (532 nm, 0.3 mW) and collected (>594 nm) from above. Bright spots are NVs, the nanowire appears dark, and the contacts (Au) exhibit typical background PL. We focus on the indicated spot, with PL primarily from single NV whose symmetry axis lies 35° from the $\hat{y}$-axis in the yz plane [223]. Static magnetic fields are applied with a permanent neodymium magnet on a motorized stage, calibrated using the NV spin transitions [223]. For this device, a moderate field ($10 - 40$ mT) applied along the NV symmetry axis saturates the Py magnetization along $\hat{y}$, canted at most ∼3° out of the xy plane (dictated by shape anisotropy [223]). All measurements are taken at room temperature.

2.3 Transport Characterization of Magnetic Resonances

To verify the device's functionality, we perform ferromagnetic resonance (FMR) by applying current $I(t) = I_0 + I_{\mathrm{RF}} \cos 2\pi\nu_{\mathrm{NW}} t$ through the nanowire (bias I_0, amplitude I_{RF}, frequency ν_{NW}), and reading the anisotropic magnetoresistance (AMR) response via a generated DC voltage ΔV_{MR} [223, 224]. Due to the spin Hall effect, the electrical current $I(t)$ drives a pure spin current (polarized along $\hat{y}$) into the Py layer, applying a torque $\partial_t \hat{m} \parallel \hat{y}$ on the Py magnetization's unit vector $\hat{m} = m_x\hat{x} + m_y\hat{y} + m_z\hat{z}$. The field $\vec{H}_I \parallel \hat{y}$ generated by this current applies a torque along $\hat{z}$.

A "typical" ST-FMR spectrum for field $\mu_0 H_0 = 16.5$ mT applied along the NV axis but rotated $\theta = 5°$ about $\hat{z}$ is shown in Fig. 2.3(a) (blue circles), with $I_0 = 0$, and $I_{\mathrm{RF}} = 0.95$ mA. The resonant feature at 1.6 GHz is well fit by the expected Fano-like lineshape [223, 224], allowing us to extract the resonant frequency ν_{FMR} and linewidth $\Delta\nu$. Figure 2.3(b) shows the field dependence of these spectra (color scale) and the fit values of ν_{FMR} (points). The initial decrease in frequency corresponds to the equilibrium orientation $\langle\hat{m}\rangle$ shifting from

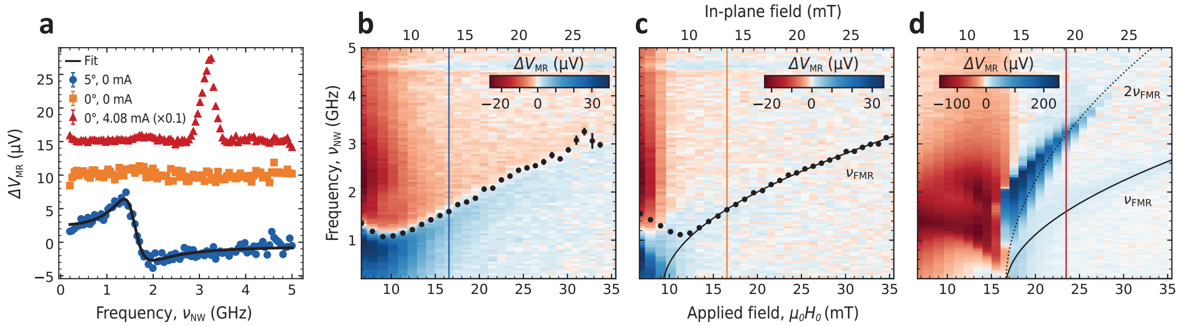

Figure 2.3: Transport FMR and parametric response. (a) Voltage ΔV_{MR} spectra (vertically separated for clarity) for bias $I_0 = 0$, RF amplitude $I_{\mathrm{RF}} = 0.95$ mA, and magnetic field $\mu_0 H_0 = 16.5$ mT applied along the NV axis (orange) or rotated about $\hat{z}$ by $\theta = 5°$ (blue). Red points (y-values divided by 10) correspond to $I_0 = 4.08$ mA and $\theta = 0°$ (taken at $\mu_0 H_0 = 23.5$ mT), showing a large resonance near twice the FMR frequency ν_{FMR}. (b) and (c) show the frequency and field dependence of ΔV_{MR} for $\theta = 5°$ and $0°$, with symbols denoting fit values of ν_{FMR}. (d) Same as (c), but with $I_0 = 4.08$ mA. Vertical lines in (b)-(d) correspond to the traces plotted in (a).

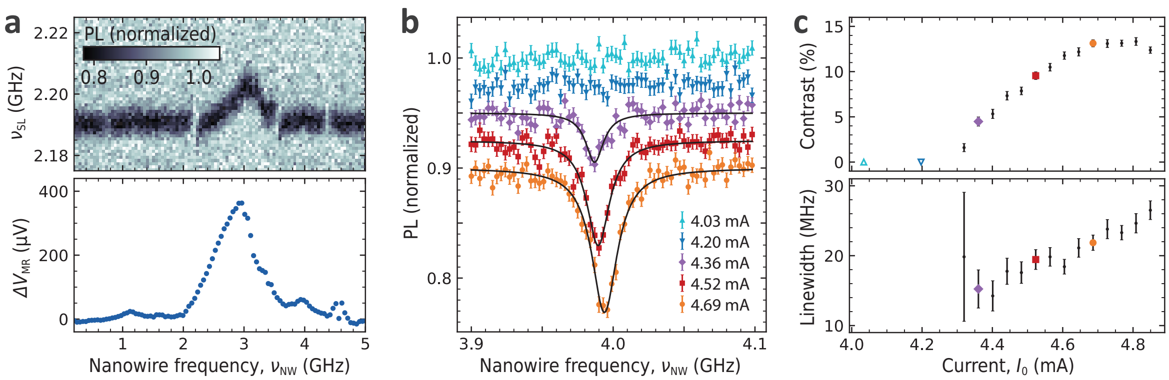

Figure 2.4: NV detection of parametrically-driven FMR. (a) Top: Photoluminescence (PL) versus stripline (nanowire) frequency ν_{SL} (ν_{NW}) with field $\mu_0 H_0 = 22.5$ mT along the NV axis, nanowire currents $I_{\mathrm{RF}} = 1.15 \pm 0.08$ mA and $I_0 = 4.9$ mA, and 0.2 mW of illumination between π-pulses. PL decreases near the ESR frequency $\nu_- = 2.19$ GHz, and ν_- shifts due to a reduced axial stray field. Data are normalized to off-resonant levels, which is why the contrast vanishes when ν_{NW} matches ESR frequencies (i.e., near 2.19 GHz, 3.59 GHz) or their harmonics (4.38 GHz). Bottom: Transport FMR readout ΔV_{MR} under the same conditions. Note the sharp feature at 4.6 GHz is an artifact from a lossy resonance in the waveguides, wirebonds, and device (see also Fig. 2.5(a)). (b) Same PL measurement as (a), but with *no* stripline power, $\mu_0 H_0 = 29.6$ mT, and varied I_0, driven near $2\nu_-$. Solid curves represent Lorentzian fits used to determine the ESR contrast and linewidth. (c) ESR contrast (top) and linewidth (bottom) for a wider range of currents. Below $I_0 = 4.3$ mA, data are consistent with zero contrast (see (b)).

$\hat{x}$ (where shape anisotropy provides $\nu_{\rm FMR} \sim 1$ GHz) and saturating along $\approx \hat{y}$, where the anisotropy field opposes the applied field. When $\theta = 0°$ (Fig. 2.3(a), orange squares), this FMR signal vanishes (as expected above the saturation field), since both the drive torques and AMR response also vanish to lowest order in m_x and m_z [223]. Figure 2.3(c) shows the field dependence of these $\theta = 0°$ spectra, along with $\nu_{\rm FMR}$ estimated from values at $\theta \neq 0$ [223]. Above saturation, $\nu_{\rm FMR}$ is well fit by the Kittel formula for spatially uniform $\hat{m}$, providing effective in-plane (out-of-plane) coercive fields $\mu_0 H_{yx} = 7.57 \pm 0.08$ mT ($\mu_0 H_{zx} = 517 \pm 4$ mT) [223].

Figure 2.3(d) shows the same $\theta = 0°$ measurement with $I_0 = 4.08$ mA. This applies a steady torque along $-\hat{y}$ that anti-damps the magnetization ($H_I = -6$ mT also shifts saturation to higher fields). Importantly, a *significantly* larger, asymmetric peak appears near twice the expected FMR frequency (see Fig. 2.3(a), red symbols), suggesting parametrically driven, large-amplitude oscillations. Simple macrospin simulations [223] reproduce the sign, magnitude, frequency, and line shape of this feature semi-quantitatively, and we interpret it as arising from a large-angle elliptical precession [214] of the spatially-averaged magnetization. Within this macrospin approximation, the largest-amplitude signal (120 μV) in Fig. 2.3(a) corresponds to an in-plane (out-of-plane) precession angle $\approx 30°$ (6°).

2.4 NV Response to Parametric Oscillations

This picture is validated by the NV's PL spectrum shown in Fig. 2.4. First, while driving the nanowire at frequency $\nu_{\rm NW}$, we apply a π-pulse with a nearby stripline to determine the NV's lower electron spin resonance (ESR) frequency. Figure 2.4(a) shows the PL response (top) and $\Delta V_{\rm MR}$ (bottom) for field $\mu_0 H_0 = 22.5$ mT along the NV axis. Reductions in PL are associated with driving the NV spin from its $m_s = 0$ spin projection to $m_s = \pm 1$, occurring at resonant frequencies $\nu_\pm$. Notably, the frequency ν_- of the stripline-driven transition shifts by up to 13 MHz when $\hat{m}$ is driven to large amplitude, and follows a path qualitatively similar to $\Delta V_{\rm MR}$. The maximum shift in ν_- corresponds to a decrease in the NV-axial magnetic field of 0.5 mT, as expected for the reduced average magnetization. This is a large fraction of the estimated 2.4 mT total stray field [223], corresponding to an in-plane precession angle

$\approx 60°$ that is within 10% of the value (55°) estimated from ΔV_{MR} in Fig. 2.4(a). We suspect the observed differences in line shape between (a) and (b) arise from the spatial structure of the actual (non-uniform) spin wave, which should change when the system is driven to a large-amplitude, nonlinear regime; in general, the stray field at the NV should respond differently to such changes than the device's overall resistance.

More compellingly, we can drive the NV transition using only the Py layer's stray field. Figure 2.4(b) shows a similar set of measurements in the absence of stripline current, with $\mu_0 H_0$ tuned to 29.6 mT, such that $\nu_{\mathrm{FMR}} \approx \nu_-$. Above $I_0 = 4.3$ mA, a PL dip (corresponding to field-driven transitions) appears at *twice* ν_-, as expected for parametric oscillations at half the drive frequency. Figure 2.4(c) shows the contrast and linewidth of this PL dip for a wider bias range, illustrating a sharp threshold at $I_0 = 4.3$ mA. This measured PL response provides unambiguous evidence of ST anti-damping and large-amplitude, parametrically driven oscillations. We note that details such as the precise threshold current and shapes of the bias dependences in (c), depend somewhat on $\vec{H}_I$, which slightly tunes the NV and FMR frequencies.

In Fig. 2.5, we map out the parametrically driven phase space of (a) ΔV_{MR}, and (b) PL under the same conditions as Fig. 2.4. For this larger drive, new features appear above the primary parametric ΔV_{MR} peak, which we tentatively attribute to higher order spin wave modes [225]. Of interest, the Py-driven PL feature near $2\nu_-$ from Fig. 2.4(b) extends over a wide range of fields, consistent with the presence of these higher-frequency transport features.

At this larger drive, we observe a residual directly-driven precession amplitude up to $\sim 14°$ at ν_{FMR} in the transport data (Fig. 2.5(a)). Despite this, we observe no evidence of spin flips at ν_{FMR} in the PL spectra of Fig. 2.5(b), contrasting what is ubiquitously observed near extended films [209–213]. We tentatively attribute this to the reduced density of states in our confined geometry, which acts to suppress multi-magnon up-conversion processes.

Finally, as shown in the inset, the Py-driven spin resonance splits by up to ~60 MHz at some fields. The nature of this splitting will be the subject of future work, but we suspect it is due to the presence of quasistable magnetic modes [226,227] having different average stray fields. Notably, information about these dynamics are *not* apparent in (a), highlighting this technique's potential to provide qualitatively new information.

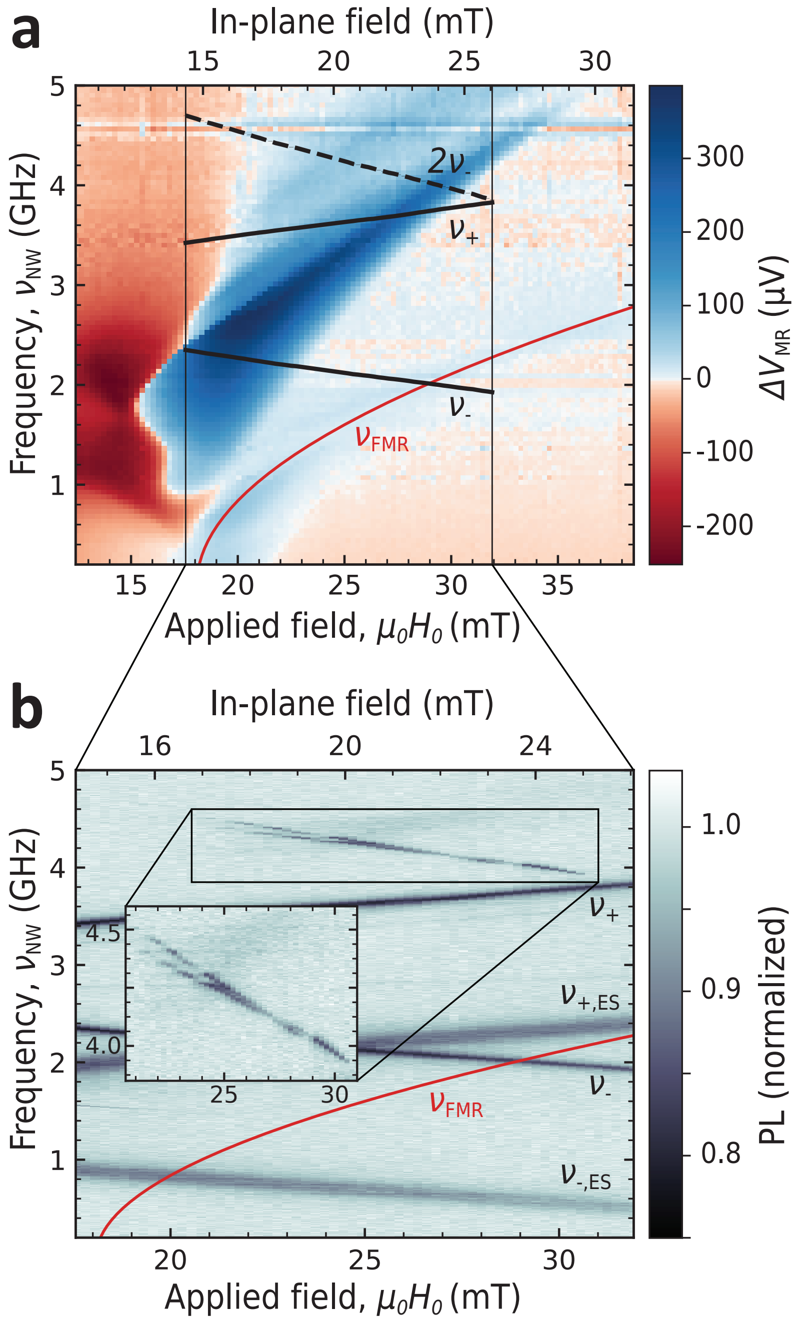

Figure 2.5: Phase space for parametrically driven (a) ΔV_{MR} and (b) PL (0.2 mW illumination) at $I_0 = 4.9$ mA and $I_{\mathrm{RF}} = 1.15$ mA. The four prominent PL features correspond to current-driven ESR transitions of the ground ($\nu_\pm$) and excited ($\nu_{\pm,\mathrm{ES}}$) states. Inset of (b) shows the Py-driven feature at $2\nu_-$. Red curves indicate the expected FMR frequency ν_{FMR}.

2.5 Strongly Damped Magnetization

The associated NV spin relaxation rates $\Gamma_\pm$ can also probe the local field noise, providing some information about the thermal occupancy of spin wave modes [106, 213]. Stated briefly, the noise spectral density $S_\perp$ of the stray field perpendicular to the NV axis (units of T^2/Hz) should have the form

$$S_\perp(\nu, H_0) = \sum_{\mathbf{k}} \bar{n}(\nu_{\mathbf{k}}(H_0)) P_{\mathbf{k}}(\nu, H_0) f_{\mathbf{k}}, \tag{2.1}$$

where $\bar{n}(\nu_{\mathbf{k}})$ is the thermal occupancy of the spin wave mode having wavenumber $\mathbf{k}$ and frequency $\nu_{\mathbf{k}}$, $f_{\mathbf{k}}$ is a constant converting magnon number to field noise power, and $P_{\mathbf{k}}(\nu, H_0)$ is a density function describing how this power is spread over the frequency domain (peaked at $\nu_{\mathbf{k}}$). In the presence of $S_\perp$, the NV spin relaxation rate $\Gamma(\nu)$ increases from its nominal value $\Gamma^0 \sim 60$ Hz [223] to a value

$$\Gamma(\nu) = \Gamma^0 + \frac{\gamma_{\mathrm{NV}}^2}{2} S_\perp, \tag{2.2}$$

where γ_{NV} is the gyromagnetic ratio of the NV spin. Figure 2.6(a) shows the measured [223] relaxation rates $\Gamma_\pm$ for varied field H_0, along with $\nu_\pm$ and ν_{FMR} below. Qualitatively similarly to extended YIG films [213], the largest relaxation occurs when when $\nu_\pm$ is just above ν_{FMR}, with peak value determined by the balance of $\bar{n}$, $P_{\mathbf{k}}$, $f_{\mathbf{k}}$ (which takes the largest value when $2\pi/|\mathbf{k}|$ is comparable to the NV-wire distance), and the density of spin wave states. In contrast to Ref. [213], spin-transfer damping (and antidamping) in this confined metallic system should completely dominate over Joule heating (the nanowire temperature changes at most by ~5 K [223]), enabling strong modification of the thermal fluctuations. Figure 2.6(b) shows how $\Gamma_\pm$ varies with I_0 (while simultaneously compensating $\vec{H}_I$ to fix ν_{FMR}); the weaker I_0-generated field at the NV leads to modest shifts of $\nu_\pm$ in Fig. 2.6(d). Both relaxation rates *significantly* decrease for negative current (damping), indicating a strong suppression of stray field noise, and increase for positive current (antidamping). Naively assuming these changes arise entirely from $\bar{n}(\nu_\pm)$, and that the action of damping is to modify the effective magnetic temperature T_{eff} [106, 213], the observed change in Γ_- corresponds to ST cooling to $T_{\mathrm{eff}} \sim 150$ K at $I_0 = -4.08$ mA. However, the probe frequencies $\nu_\pm$ drift with I_0 and the ST

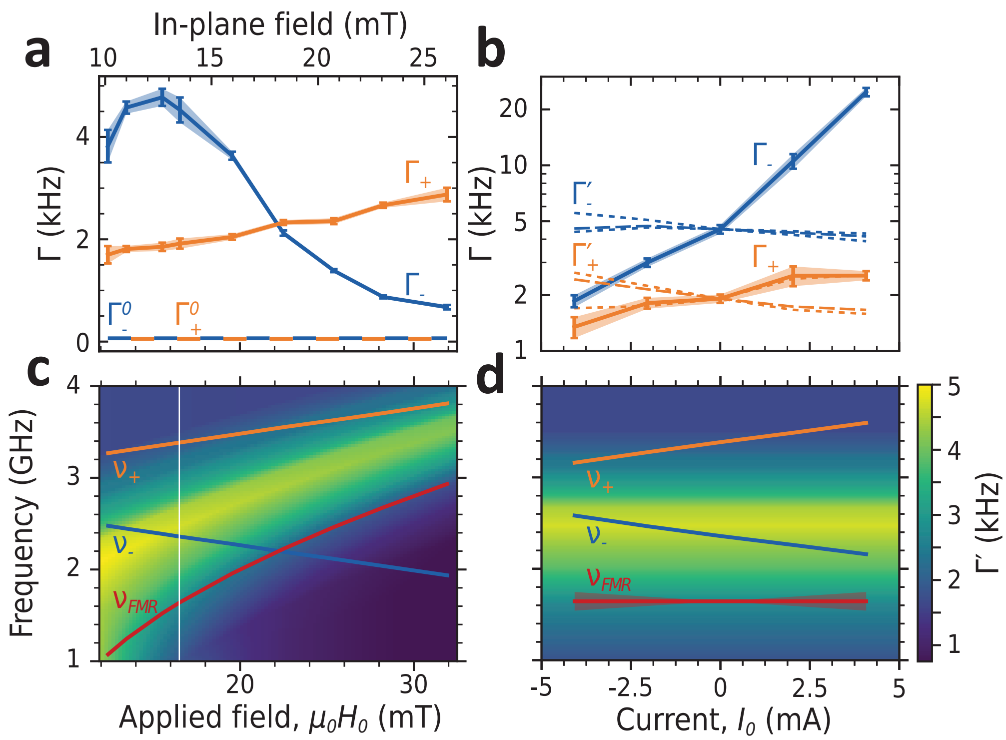

Figure 2.6: Spin relaxometry under bias. (a) Measured relaxation rates $\Gamma_\pm$ versus applied field, with bias I_0=0. Also shown is the internal rates $\Gamma^0_\pm$. (b) Measured $\Gamma_\pm$ for varied I_0 (solid lines), adjusting $\mu_0 H_0$ (nominally 16.5 mT at $I_0 = 0$, white line in (c)) to ensure $\nu_{\rm FMR}$ remains constant to within the shown error (shading on red line in (d)). Dashed lines are estimated rates $\Gamma'_\pm$ in the absence of ST effects, with absolute bounds shown as dotted lines. (c)-(d) Comparison of $\nu_\pm$ and $\nu_{\rm FMR}$ (curves) with reconstructed estimate of Γ' (color plots) [223].

damping broadens the peak in $S_\perp$. A model combining these effects with the observed field-dependence in Fig. 2.6(a) [223] produces the "spin transfer free" relaxation rate estimates $\Gamma'_\pm$ shown in Fig. 2.6(b) and the color scale in the lower panels of (a) and (b). Importantly, the expected changes are much smaller (and have the opposite trend), suggesting that our estimate of T_{eff} might represent an upper bound. We note that, in this geometry, we could not extract trustworthy parameters from FMR at maximum damping, highlighting the utility of the NV as an independent probe.

2.6 Conclusions

The NV PL spectrum provides qualitatively different information about magnetic nanocircuits than is provided by traditional transport measurements. We demonstrated parametric magnetic oscillations controlled by ST effects, and that ESR transitions can be driven entirely by a local magnetization. The latter technique may potentially facilitate fast, low-power control of NV spins, and the nonlinear dynamics involved could, e.g., be used to amplify incident fields [207]. We also observe large changes in the NV spin relaxation time when subjecting the magnetic element to ST damping, consistent with magnon cooling to well below ambient temperatures. Finally, we note that the demonstrated stray field coupling between the NV and spin wave modes is quite large. Of note, Fig. 2.6(a) exhibits a maximal Γ at 15.5 mT, where ν_- corresponds to a room-temperature magnon occupancy $\sim$2500, meaning the noise $S_{\perp,\text{ZPF}}$ generated by the ferromagnetic zero-point fluctuations would set Γ $\sim$1 Hz. This value is comparable to the intrinsic relaxation rates of bulk NV's at low temperature [228], suggesting it might be feasible to resolve the quantum fluctuations of a magnetic nanocircuit.

Appendix

2.7 Device fabrication

We fabricate an 8-μm-long × 417-nm-wide Py ($Ni_{81}Fe_{19}$) / Pt nanowire (layer thicknesses t_{Py} = 10 nm and t_{Pt} = 10 nm) on CVD-grown, electronic grade diamond (Element Six), as shown in Fig. 1 of the main text. Prior to depositing the nanowire, we relieve strain and smooth the diamond surface to ∼0.2 nm-rms over micron length scales (∼0.05 nm-rms over smaller scales) with Ar/Cl_2 etching [229], then create a layer of NV centers 75±15 nm below the surface with $^{15}N^+$ implantation (60 keV, Innovion Corp.) and high-temperature annealing [230]. A subsequent Ar/O_2 plasma etch (20 mTorr, 35 sccm Ar, 10 sccm O_2, 108 W RF for 45 sec; etches 20 nm/min) removes contaminants and reduces the NV depth to 60±15 nm. To remove any residual graphitized carbon and oxygen-terminate the surface, we perform a final clean in a boiling 1:1:1 mixture of nitric, perchloric, and sulfuric acid at 200° C for 1 hour. The Py/Pt nanowire is deposited with e-beam lithography, sputtering, and liftoff[1]. We then deposit Ti (10 nm) / Au (50 nm) macroscopic leads and a microwave stripline (10 μm wide, 17 μm center-to-center distance) using photolithography, and finally connect the leads to the nanowire with another e-beam liftoff (Ti (10 nm) / Au (70 nm) evaporated). The contacts leave an "active" region of length 5.2 μm exposed.

2.8 NV measurements

2.8.1 Single NV identification and isolation

We focus on an NV center ("NV_A") having the strongest stray field coupling. However, this NV is positioned near a second NV "NV_B", that provides an additional small photoluminescence (PL) signal. As described below, we identify these two NVs using a combination

[1]Note we recommend a more directional deposition (e.g., evaporation) to eliminate edge burrs and improve liftoff yield, though this might come at the expense of reduced film quality. One can also pattern sputtered films (e.g., with an ion mill), but it remains to be seen how such a process affects the optical properties of the diamond substrate.

of electron spin resonance (ESR) spectroscopy and photon correlation measurements, taking advantage of their different symmetry axes to isolate signals from NV_A.

The two NVs are both associated with the single bright emission spot shown in Fig. 1(b) of the main text. With the 532 nm excitation focused on this spot, we observe ESR spectra indicating the presence of NVs having two different orientations. Figure 2.7 shows two ESR spectra taken with a 6 mT magnetic field oriented 35° from the diamond surface in the xz and yz planes, such that it is aligned with one of the allowed <111> crystallographic orientations of the diamond bonds (i.e., along one of the allowed NV symmetry axes). Dips in PL are associated with driving the NV from its $m_s = 0$ spin projection to $m_s = \pm 1$, occurring at frequencies $\nu_\pm$ (nominally $\nu_+ = \nu_- = 2.87$ GHz at zero field). The deepest photoluminescence dip in both spectra is associated with $m_s = 0 \rightarrow -1$ transition of the better-coupled NV center (NV_A), mostly because the polarization of the 532 nm excitation is perpendicular to the NV_A symmetry axis. This transition shows the largest magnetic field dependence when the field is in the yz plane, parallel to NV_A (corresponding to the arrow in Fig. 1(a) of the main text), while the shallower $m_s = 0 \rightarrow -1$ transition of NV_B shows the largest deviation with the field aligned in the xz plane. Note that the $m_s = 0 \rightarrow +1$ transition of NV_A is barely visible above the noise in each spectrum, due to imperfect power coupling to our stripline at the higher frequencies (this is also why we do not see the $m_s = 0 \rightarrow +1$ transition for NV_B in these spectra). In principle, there could be multiple NVs creating the observed spectra, but the total photon count rate is approximately what we expect for two NVs. Moreover, because the emission spot is close to the magnetic nanowire, in a region of high magnetic field gradient, NVs with the same orientation would be expected to show distinct ESR lines. We see no evidence of unexpected dips under any conditions, lending additional credence to the identification of two NVs.

To further verify our interpretation that only two NV centers are co-located within the emission spot, we perform photon correlation measurements to estimate the number of contributing emitters. The second order correlation function $g^{(2)}(\tau)$ was measured with a Hanbury-Brown-Twiss setup, using a fiber beam-splitter and two single photon counting modules. A time-correlated single photon counting system (PicoHarp 300) was used to measure the histogram of times between two consecutive photons. Such a normalized distribution can be interpreted as a measurement of $g^{(2)}(\tau)$, as long as τ is much smaller than the mean time between two detection events (for us, $\tau \ll 1/\text{count rate} = (30\text{ kcounts/s})^{-1}$ ≈ 33 µs) [231]. We measure a background count rate (on a dark area of the sample) of $\approx$ 3 kcounts/s, which we subtract from our data before analysis.

Our data shows a clear anti-bunching signature at short times (see Fig. 2.8), characteristic of a small number of quantum emitters, and slight bunching at longer times, associated with metastable states in the emitters. To quantify $g^{(2)}(0)$ requires that we appropriately normalize the data. Merely setting the long-time value to 1 is problematic because of the exponential decay associated with the fact that we are not directly measuring the correlation function but a histogram of times between photons. Indeed, we observed such an exponential decays for $g^{(2)}(\tau)$ measured with attenuated laser light. We thus compensate for the decay by fitting an exponential with a decay constant τ, $e^{-t/\tau}$ to the data from 1 μs onward. Multiplying the full spectrum of data points by $e^{t/\tau}$ corrects for the exponential decay, and allows us to used the long-time value for our normalization. We then use a three level model to fit the curve to the function [232]:

$$g^{(2)}(\tau) = c_1 \left(1 + c_2 e^{-\frac{\tau}{\tau_1}} + c_3 e^{-\frac{\tau}{\tau_2}}\right), \tag{2.3}$$

where $c_{1,2,3}$ are scaling factors and $\tau_{1,2}$ correspond to the lifetimes of the involved NV states. We find that $g^{(2)}(0) = 1 + c_2 + c_3 = 0.45 \pm 0.01$, consistent with two co-located emitters, where one is slightly better coupled to our optical excitation/collection path than the other.

In our measurements, we isolate NV_A from NV_B by taking advantage of their different orientations. For ESR measurements (such as in Fig. 3 of the main text), the transitions of NV_A and NV_B are spectrally resolved. Moreover, we align the polarization of the 532 nm illumination to preferentially excite NV_A, reducing photoluminescence from NV_B; we also work in magnetic fields aligned with NV_A, which reduces the ESR contrast of NV_B. As a result, the resonances from NV_B are only weakly visible in the spin resonance data shown in Fig. 4(b) of the main text. For spin relaxation measurements, we use π pulses tuned to the transitions of NV_A to isolate its relaxation rates from those of NV_B, as described in further detail below.

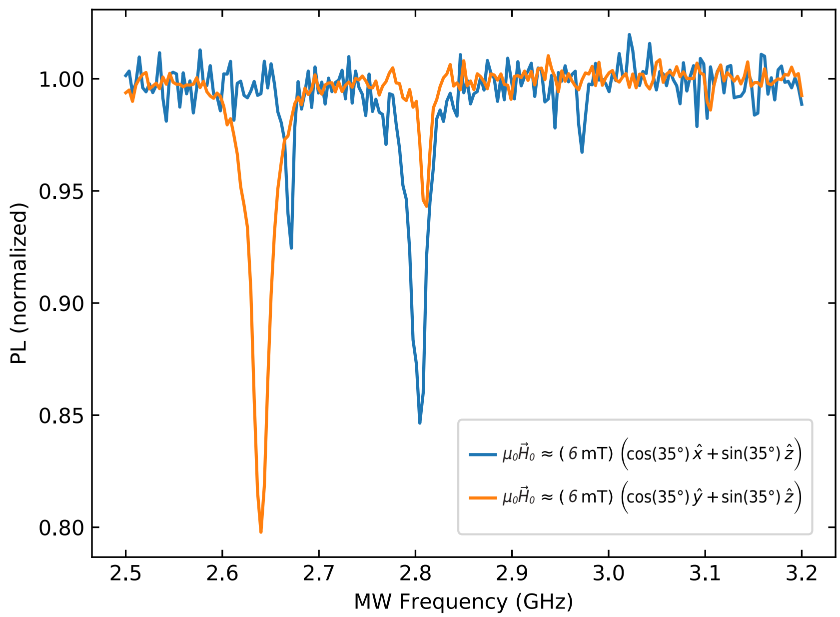

Figure 2.7: ESR measurement of the probed spot in Fig. 1(b) of the main text, showing PL dips associated with two NV centers.

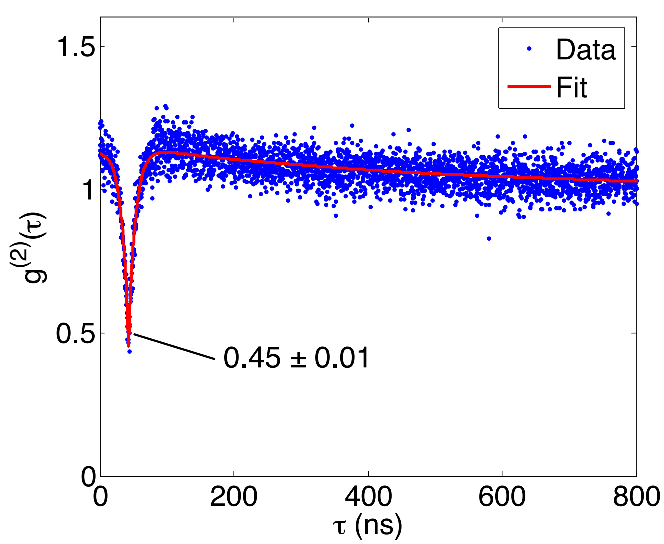

Figure 2.8: $g^{(2)}(\tau)$ correlation measurement of the studied emission spot, with $g^{(2)}(0)$=0.45±0.01.

2.8.2 Extracting spin relaxation rates

We extract the two relaxation rates $\Gamma_\pm$ for NV_A by initializing the spin into the three spin projections $m_s = -1, 0, 1$, observing its relaxation via photoluminescence measurements, and fitting our data to a rate equation model.

We prepare the spin projections using a 0.4 mW pulse of 532 nm excitation, which optically pumps both NV_A and NV_B into $m_s = 0$; to prepare $m_s = \pm 1$, we then apply a π pulse of microwaves tuned to the NV_A spin transitions for durations of 50-200 ns, chosen to maximize the contrast of a Rabi sequence. These π pulses are far off resonance with NV_B, so it remains in $m_s = 0$. After a variable delay of duration τ, we again apply a pulse of 532 nm excitation and observe photoluminescence counts, which are higher for $m_s = 0$ states than for $m_s = \pm 1$. In the end, we record three photoluminescence traces: $f_0(\tau), f_+(\tau)$, and $f_-(\tau)$, where the subscript indicates the spin state into which NV_A was initialized.

Since these photoluminescence traces include emission from both NV_A and NV_B, we consider the differences in the photoluminescence traces $d_-(\tau) = f_0(\tau) - f_-(\tau)$ and $d_+(\tau) = f_0(\tau) - f_+(\tau)$. Because NV_B is prepared in the same way for all three initializations, its (possibly τ-dependent) photoluminescence is eliminated in the data sets $d_\pm(\tau)$, as is any background photoluminescence not associated with NV_A.

We then simultaneously fit $d_-(\tau)$ and $d_+(\tau)$ to a rate equation model for spin relaxation:

$$\begin{aligned}
\frac{dp_-(t)}{dt} &= \Gamma_- \left(p_0(t) - p_-(t)\right) \\
\frac{dp_+(t)}{dt} &= \Gamma_+ \left(p_0(t) - p_+(t)\right) \\
\frac{dp_0(t)}{dt} &= -(\Gamma_- + \Gamma_+)p_0(t) + \Gamma_- p_-(t) + \Gamma_+ p_+(t),
\end{aligned} \tag{2.4}$$

where $p_m(t)$ is the population of NV_A in spin state m and $\Gamma_\pm$ are the relaxation rates on the $m_s = 0 \leftrightarrow m_s = \pm 1$ transitions. We also considered double quantum relaxation between $m_s = \pm 1$ states, but our fits revealed that this rate was insignificant. The fit functions for $d_\pm(\tau)$ are found by calculating the population in $m_s = 0$ for three different spin initializations, $p_0(\tau)^{(m)}$ (where the superscript indicates the initial state), and subtracting to reconstruct a signal proportional to $d_\pm(\tau) \propto p_0(\tau)^{(0)} - p_0(\tau)^{(\pm)}$. Note that this proportionality holds even for imperfect optical pumping and imperfect π pulses – low fidelity initialization and incomplete π pulses reduce the contrast of our signals, but not their time dependence. We can thus fit $d_{\pm}(\tau)$ to $A\left(p_0(\tau)^{(0)} - p_0(\tau)^{(\pm)}\right)$, where A is an unknown fitting parameter, and extract the two relaxation rates $\Gamma_{\pm}$.

2.9 Magnetic field calibration

We apply static magnetic fields using a permanent magnet (K&J magnetics, D42-N52) mounted on a three-axis translation stage equipped with closed-loop motorized actuators (CONEX-TRB25CC). The 25mm range of motion permits us to apply magnetic fields up to 90 mT oriented along the NV symmetry axis.

To calibrate the relationship between the actuator position and the applied magnetic field, we exploit the field-dependent photoluminescence of the NV center [233]. Essentially, NV photoluminescence is maximized when the magnetic field is parallel to its symmetry axis, with heightened sensitivity near the ground- and excited-state level anti-crossings near 103 mT and 51 mT, respectively. Following the procedure described in Ref. [210], we measure the photoluminescence of an NV as a function of the position of the permanent magnet. From this data, we can extract the controller coordinates that bring the NV center to the excited state level anti-crossing (51 mT) and align the magnetic field with the NV axis. We then model the stray field of the permanent magnet using RADIA [234] and determine the position (relative to the permanent magnet origin) where the stray field is 51 mT aligned with the NV axis. This provides a coordinate transformation between our controller position and the model. We can then use the RADIA model to roughly predict the field as a function of controller position. We design a trajectory for the magnet that should maintain the magnetic field along the NV axis or at a defined angle relative to that axis.

This calibration procedure gives only an approximation of the magnetic field due to potential inaccuracy of the RADIA model and possible misalignment between the (nominally aligned) coordinate axes of our sample and the controller axes. We therefore use NV electron spin resonance (ESR) measurements to determine the actual magnetic field taken along the trajectories used in our experiments. Note that these measurements were taken after the device magnetization disappeared (see Sec. 2.12.4), so the NV experiences only the applied magnetic field. We fit the ESR spectra to extract the transition frequencies $\nu_{\pm}$. From the linear and quadratic Zeeman effects, we can determine the on- and off-axis components of the magnetic field [210], and thus calculate its magnitude. Figure 2.9(a) shows the difference between the extracted and expected field magnitudes as a function of the expected field predicted by the RADIA model. These values are found using an NV g-factor of 2.0030(3) and a zero field splitting of 2.870(2) GHz, consistent with our observed splittings and literature values [196, 235]. The solid red curve is a sixth order polynomial interpolating function used to rescale the magnitudes of the magnetic fields in the data presented in the main text. Figure 2.9(b) shows the extracted angle of the magnetic field, which is poorly constrained by these measurements; due to the good ESR contrast observed over the entire magnetic field scan at $\theta = 0°$ in Fig. 4(b) of the main text, and the strong suppression of directly-driven FMR at $\theta = 0°$, we believe the angular alignment is good to within a couple of degrees.

2.10 Spin transfer control and magnetoresistive read-out

We control the magnetization of the Py layer with current $I(t)$ in the nanowire, which provides two torques. First, as indicated in Fig. 1(a) of the main text, the current density J_{Pt} in the Pt layer produces a spin current density $J_{\text{s}} = \theta_{\text{SH}} J_{\text{Pt}}$ (where θ_{SH} is Pt's spin Hall angle), polarized along $\hat{y}$ and travelling along $\hat{z}$ [236]. A fraction η of these spins are absorbed by the Py layer ($\eta\theta_{\text{SH}} = 0.055$ [224]), thereby applying an areal spin transfer torque (STT) density at the Py interface, or an effective per-volume torque density (N·m/m^3)

$$\vec{T}_{\text{STT}} = \frac{\hbar\eta\theta_{\text{SH}} J_{\text{Pt}}}{2et_{\text{Py}}} \hat{m} \times (\hat{m} \times \hat{y}) \,, \tag{2.5}$$

where the unit vector $\hat{m} = m_x\hat{x} + m_y\hat{y} + m_z\hat{z}$ represents the orientation of the local magnetization. Second, the current in the wire generates a magnetic field $\vec{H}_I$ in the Py layer, with a torque (volume) density

$$\vec{T}_{H_I} = \mu_0 M_s \vec{H}_I \times \hat{m}, \tag{2.6}$$

where M_s is the Py saturation magnetization. Changes in the magnetization can then be read out via the device's resistance, which varies approximately[2] as

$$R = R_0(1 + \delta_{\text{AMR}} m_x^2), \tag{2.7}$$

where $R_0 = 237\ \Omega$ is the wire's unbiased resistance at $m_x = 0$, and $R_0\delta_{\text{AMR}} \approx 0.2$ mΩ is the change due to anisotropic magnetoresistance (AMR) from the fraction of current flowing through the Py layer (measured by monitoring R while sweeping the field).

To verify device functionality, we perform spin transfer ferromagnetic resonance (ST-FMR) similar to that of Ref. [224]. To briefly summarize, a current $I(t) = I_0 + I_{\text{RF}} \cos(2\pi\nu_{\text{NW}} t)$ (with DC bias I_0, "radio frequency" (RF) amplitude I_{RF}, and frequency ν_{NW}) driving coherent resistance oscillations $R(t) = R_0 + \Delta R_0 + \Delta R_{\text{RF}} \cos(\nu_{\text{NW}} t + \psi)$ (for constant offset ΔR_0,

[2] This assumes $m_z \ll m_x$, which is justified by the calculations and simulations in Sec. 2.12.

amplitude ΔR_{RF}, and phase ψ) will generate a time-averaged voltage change

$$\Delta V = I_0 \Delta R_0 + \frac{1}{2} I_{\mathrm{RF}} \Delta R_{\mathrm{RF}} \cos\psi \tag{2.8}$$

that can be read out with a lock-in technique (see Sec. 2.11.2). This voltage comprises a resonant magnetoresistance signal ΔV_{MR} (estimated for a macrospin in Sec. 2.12) and a broad background due to Joule heating (useful for estimating I_{RF}, as discussed in Sec. 2.11) that is subtracted from all presented spectra.

2.11 Joule heating background, differential resistance, and RF current calibration

When a time-dependent current passes through a resistive wire, it dissipates a time-dependent power, thereby heating the sample and causing a time-dependent change in resistance. In general, this nonlinear response can generate a static voltage $\langle V \rangle$ across the resistor. Here we develop a framework for quantifying this effect, and show how it can be used to provide a reasonable estimate of the RF current flowing through our nanowires. This calibration considers RF temperature oscillations not included in (e.g.) Tshitoyan *et al* [237], which are especially relevant when the substrate is highly thermally conductive.

2.11.1 Derivation of Joule heating mixdown voltage

In general, the instantaneous voltage V will depend on current I and the change in temperature ΔT. For small I and ΔT, we can Taylor expand to 3rd order:

$$\begin{aligned}
V \approx\ & (\partial_I V)\, I + (\partial_T V)\, \Delta T && (2.9)\\
& + \frac{1}{2}\left(\partial_I^2 V\right) I^2 + (\partial_T \partial_I V)\, I \Delta T + \frac{1}{2}\left(\partial_T^2 V\right) \Delta T^2 && (2.10)\\
& + \frac{1}{6}\left(\partial_I^3 V\right) I^3 + \frac{1}{2}\left(\partial_T \partial_I^2 V\right) I^2 \Delta T + \frac{1}{2}\left(\partial_T^2 \partial_I V\right) I \Delta T^2 + \frac{1}{6}\left(\partial_T^3 V\right) \Delta T^3, && (2.11)
\end{aligned}$$

where all of the parenthetical factors are constants of the system determined by the resistor's geometry, materials, and thermal anchoring. We simplify this with the following assumptions:

1. In the absence of temperature change, the resistor responds linearly. This means the terms (red) having no temperature dependence $\partial_I^2 V = \partial_I^3 V = 0$; as a result, $\partial_T \partial_I^2 V = 0$ as well.

2. Changing the temperature does not on its own generate a voltage. This means the current-independent terms $\partial_T V = \partial_T^2 V = \partial_T^3 V = 0$ (teal).

3. The temperature change $\Delta T \sim I^2$ to lowest order, meaning the penultimate term (blue) is of order I^5 and can be dropped.[3]

Under these assumptions,

$$V \to (\partial_I V)\, I + (\partial_T \partial_I V)\, I \Delta T. \tag{2.12}$$

The first term is the heat-free linear response of the resistor, with the constant $\partial_I V$ being the resistance near $I = 0$. We emphasize that $\partial_I V$ is a constant that does *not* depend on I or ΔT (all differentials in Eq. 2.12 are evaluated at $I = \Delta T = 0$) and is qualitatively different from laboratory measurements commonly referred to as "differential resistance", wherein the current is slowly modulated and the resulting voltage modulations are recorded (see Section 2.11.2).

The second term is the Joule heating nonlinearity of interest; an "extra" voltage can be generated from this term only if there is both a current *and* a temperature change. For example, if $I = I_0$ is some constant value, this will heat the sample, causing $\Delta T > 0$, which raises the resistance by $(\partial_T \partial_I V)\, \Delta T$, at which point I_0 produces an additional voltage. If I changes slowly enough with time that the system remains in steady state, it is this term that is responsible for a bias dependence in a low-frequency differential resistance measurement (see Sec. 2.11.2).

We eliminate temperature ΔT by assuming small enough changes that ΔT responds linearly to the applied power P. In this limit, an oscillatory component in the power $P_1 \cos \omega t$

[3] In systems having a more significant Peltier effect (e.g., some spin valves), this should not be dropped.

of amplitude P_1 and frequency ω will induce a temperature change

$$\Delta T = [X(\omega)\cos\omega t + Y(\omega)\sin\omega t]\, P_1, \tag{2.13}$$

where $X(\omega)$ and $Y(\omega)$ (units of K/W) represent the thermal transfer function of the wire, capturing the magnitude and phase shift of the thermal response.[4] In our experiments, we apply a current of the form

$$I = I_0 + I_1\cos\omega t, \tag{2.14}$$

for constants I_0, I_1 and frequency ω, such that the instantaneous power is, to leading order (again assuming negligible Peltier effects)

$$\begin{aligned} P(t) &\approx (I_0 + I_1\cos\omega t)^2\,(\partial_I V) \\ &= \left(I_0^2 + \frac{1}{2}I_1^2 + 2I_0I_1\cos\omega t + \frac{1}{2}I_1^2\cos 2\omega t\right)(\partial_I V)\,. \end{aligned} \tag{2.15}$$

This comprises a thermal drive at three frequencies (zero, ω, and 2ω) which, in this linear-response limit, can be treated separately. As such, the temperature

$$\Delta T \approx P_0X_0 + P_1X(\omega)\cos\omega t + P_1Y(\omega)\sin\omega t + P_2X(2\omega)\cos 2\omega t + P_2Y(2\omega)\sin 2\omega t \tag{2.16}$$

with

$$P_0 \equiv \left(I_0^2 + \frac{1}{2}I_1^2\right)(\partial_I V) \tag{2.17}$$

$$P_1 \equiv (2I_0I_1)\,(\partial_I V) \tag{2.18}$$

$$P_2 \equiv \left(\frac{1}{2}I_1^2\right)(\partial_I V)\,. \tag{2.19}$$

[4] We choose this quadrature formulation of the transfer function over the "usual" complex one due to the nonlinear operations in the rest of the analysis. The quadrature basis is also very convenient for calculating the mixdown voltage, which requires only the in-phase component $X(\omega)$.

Plugging Eq. 2.16 into the voltage expansion of Eq. 2.12,

$$V \approx (\partial_I V)(I_0 + I_1 \cos\omega t) \tag{2.20}$$
$$+ (\partial_T \partial_I V)(I_0 + I_1 \cos\omega t)(P_0 X(0)) \tag{2.21}$$
$$+ (\partial_T \partial_I V)(I_0 + I_1 \cos\omega t)(P_1 X(\omega)\cos\omega t + P_1 Y(\omega)\sin\omega t) \tag{2.22}$$
$$+ (\partial_T \partial_I V)(I_0 + I_1 \cos\omega t)(P_2 X(2\omega)\cos 2\omega t + P_2 Y(2\omega)\sin 2\omega t)\,. \tag{2.23}$$

Taking a time-average yields

$$\begin{aligned}\langle V\rangle &= (\partial_I V) I_0 + (\partial_T \partial_I V)\left(I_0 P_0 X(0) + \frac{1}{2} I_1 P_1 X(\omega)\right)\\ &= I_0 (\partial_I V)\left(1 + \chi(0) I_0^2 + \frac{1}{2}\left[\chi(0) + 2\chi(\omega)\right] I_1^2\right)\end{aligned} \tag{2.24}$$

where we have defined a fractional resistance change transfer function

$$\chi(\omega) \equiv (\partial_T \partial_I V) X(\omega) \tag{2.25}$$

for brevity (units of $1/\mathrm{mA}^2$). The first term is Ohm's law and the second is the steady state heating due to DC current. The third term is the response to an RF drive, and is responsible for large backgrounds observed in FMR (see Sec. 2.11.2). Importantly, this comprises two terms, the first ($\chi(0)$) arising from the time-averaged power absorbed by the wire, and the second ($\chi(\omega)$) arising from the heat-induced resistance oscillations at ω mixing with the drive current.

2.11.2 Differential resistance and estimation of RF current

We now discuss a means of interpreting the signal from a lock-in-based differential resistance measurement in the presence of DC and RF current. Section 2.11.2 discusses a "traditional" continuous-wave lock-in approach, and Sec. 2.11.2 discusses an impulse method that happens to be easier with our apparatus. Section 2.11.2 then discusses a means of using the observed voltages in these measurements to estimate the RF current flowing through the device.

Traditional lock-in readout

When "differential resistance" is measured using a lock-in technique, the bias is modulated, such that the current

$$I_0 \to I_0 + I_m \cos \omega_m t, \tag{2.26}$$

where I_m is the lock-in's modulation amplitude, and $\omega_m \ll \omega$ is the modulation frequency (typically chosen to be low enough that the device remains in steady state). In this case, the voltage (Eq. 2.24) becomes

$$\langle V \rangle \to (\partial_I V)\,(I_0 + I_m \cos \omega_m t) \left(1 + \chi(0)\,(I_0 + I_m \cos \omega_m t)^2 + \frac{1}{2}\left[\chi(0) + 2\chi(\omega)\right] I_1^2\right) \tag{2.27}$$

$$= ... + (\partial_I V) \left(I_{LI} + \chi(0)\left[3I_0^2 I_m + \frac{3}{4} I_{LI}^3\right] + I_m \left[\frac{1}{2}\chi(0) + \chi(\omega)\right] I_1^2\right) \cos \omega_m t \tag{2.28}$$

where we have lumped all terms not contributing to the measured amplitude at ω_m into "..." for brevity, and used the identity

$$\cos^3 \omega_m t = \frac{3}{4} \cos \omega_m t + \frac{1}{4} \cos 3\omega_m t. \tag{2.29}$$

The lock-in measurement demodulates at ω_m to record the response amplitude, which is then divided by I_m to define a "differential resistance"

$$R_{\text{diff}} \equiv (\partial_I V) \left(1 + \chi(0)\left[3I_0^2 + \frac{3}{4} I_m^2\right] + \left[\frac{1}{2}\chi(0) + \chi(\omega)\right] I_1^2\right). \tag{2.30}$$

Note this result agrees with Eq. 2.24 in the low-frequency limit $\chi(\omega) \to \chi(0)$, but here we can see how the presence of RF current will alter this signal.

Impulse readout

In our experiment, we employ an impulse readout of R_{diff} wherein the amplitude of the modulation is slowly increased to its maximum value and then decreased to zero as

$$I_0 \to I_0 + I_s(t) \tag{2.31}$$

$$I_s(t) \equiv I_m \sin^2\left(\frac{\omega_m}{2N}t\right)\sin(\omega_m t) \tag{2.32}$$

$$= \frac{I_m}{4}\left(2\sin(\omega_m t) - \sin\left[\omega_m\left(1+\frac{1}{N}\right)t\right] + \sin\left[\omega_m\left(1+\frac{1}{N}\right)t\right]\right), \tag{2.33}$$

where N is a large integer. We have expanded I_s in the last line to highlight that this waveform includes only 3 frequencies near ω_m, which helps minimize artifacts associated with abrupt changes in current. Similar to the continuous-wave measurement, the device responds adiabatically for sufficiently small ω_m, and the low-frequency voltage becomes

$$\langle V\rangle \to V_0 + V_s(t) \tag{2.34}$$

$$= (\partial_I V)\,(I_0 + I_s(t))\left(1 + \chi(0)\,(I_0 + I_s(t))^2 + \left[\frac{1}{2}\chi(0) + \chi(\omega)\right] I_1^2\right)$$

$$= (\partial_I V)\left(\text{DC} + \left(1 + 3\chi(0)I_0^2 + \left[\frac{1}{2}\chi(0) + \chi(\omega)\right] I_1^2\right) I_s + 3\chi(0)I_0 I_s^2 + \chi(0)I_s^3\right), \tag{2.35}$$

where "DC" contains all time-independent terms. We then extract a similar "differential resistance" $R_{\text{diff,s}}$ by taking an overlap with the injected impulse $I_s(t)$ to extract a (normalized) "in-phase" response amplitude

$$R_{\text{diff,s}} = \frac{1}{I_m} \times \frac{\int_0^{2\pi N/\omega} [V_0 + V_s(t)]\, I_s(t) dt}{\int_0^{2\pi N/\omega} I_s^2(t) dt} \tag{2.36}$$

$$= \frac{8}{3\pi N I_m^3}\int_0^{2\pi N/\omega} V_s(t) I_s(t) dt. \tag{2.37}$$

By symmetry, the even powers of I_s in Eq. 2.35 vanish, leaving behind

$$R_{\text{diff,s}} = (\partial_I V)\left(1 + \chi(0)\left(3I_0^2 + \frac{35}{64}I_m^2\right) + \left[\frac{1}{2}\chi(0) + \chi(\omega)\right] I_1^2\right). \tag{2.38}$$

In practice, the measured value of $R_{\mathrm{diff,i}}$ does not depend on frequency below $\sim$ 300 Hz (limited in our case by the low-pass action of our bias-T), which allows us to estimate $\chi(0)$ from the bias-dependence of $R_{\mathrm{diff,i}}$ in the absence of RF current ($I_1 = 0$). Figure 2.10 shows a measurement of $R_{\mathrm{diff,i}}(I_0)$, with $\omega_m = 2\pi\times 265$ Hz. The data is well-fit by Eq. 2.38 (with a small offset bias $I_{\mathrm{off}} = -15 \pm 1$ μA), from which we extract $\partial_I V = 237.3 \pm 0.3\,\Omega$, $\chi(0) = 5.3085 \pm 0.004 \times 10^{-4}$ mA^{-2}. The small offset current is likely due to a combination of non-ideal electronics and Peltier effects associated with asymmetric contacts to our nanowire on chip. In the present experiment, this offset leads to at most a few-percent error in our calibration of I_1 (discussed below), along with a small, smoothly-varying background signal in our ferromagnetic resonance measurements of up to ∼5 μV at low frequencies. The associated correction, which does not affect the central conclusions of the present work, will be the subject future work.

Maximum change in wire temperature (including the green laser)

In the presence of only DC bias, Eq. 2.24 simplifies to

$$\langle V\rangle \rightarrow (\partial_I V)\,(I_0)\left(1 + \chi(0) I_0^2\right), \tag{2.39}$$

such that the DC resistance

$$\frac{\langle V\rangle}{I_0} = (\partial_I V) + (\partial_I V)\,\chi(0) I_0^2 \tag{2.40}$$

$$= R_0 + R_0 \alpha \Delta T, \tag{2.41}$$

where α is the temperature coefficient of resistance. From this, we identify

$$R_0 = \partial_I V \tag{2.42}$$

$$\Delta T = \frac{\chi(0) I_0^2}{\alpha} \tag{2.43}$$

Using the above fit values and using the Pt coefficient $\alpha \gtrsim 0.003$ K^{-1} as a lower bound, we place an upper bound on the maximum Joule heating temperature change $\Delta T \lesssim 5$ K for our

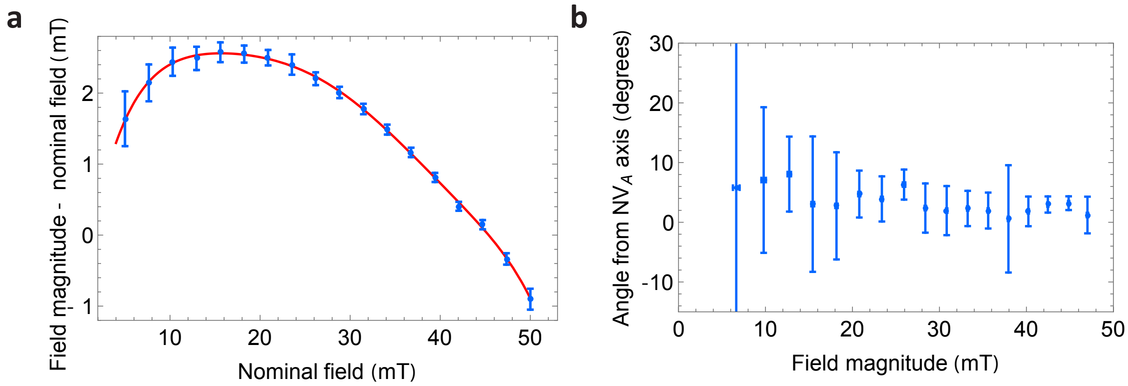

Figure 2.9: (a) Magnetic field magnitude (as determined by ESR measurements), relative to the expected magnetic field (as calculated by RADIA). Red curve is a sixth order polynomial fit used to rescale the magnetic field values in the main text. (b) Off-axis angle of the magnetic field as a function of magnitude. The (large) error bars represent systematic uncertainties in our system parameters.

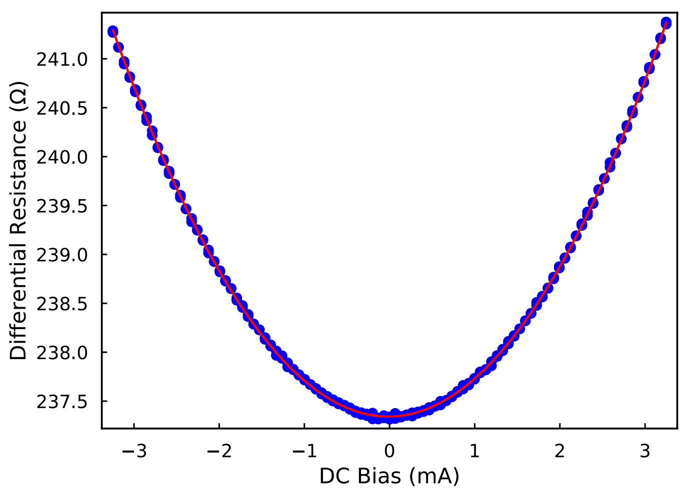

Figure 2.10: Measured impulse differential resistance $R_{\text{diff,i}}$ versus DC bias I_0 with modulation amplitude $I_m = 81.5$ μA, modulation frequency $\omega_m = 2\pi \times 265$ Hz, $N = 53$ periods per impulse, and no RF current ($I_1 = 0$). Solid red curve is a fit to the form $R_{\text{diff,s}} = (\partial_I V)\left(1 + \chi(0)\frac{35}{64}I_m^2 + 3\chi(0)\left(I_0 - I_{\text{off}}\right)^2\right)$, with fit parameters $\partial_I V = 237.3 \pm 0.3\,\Omega$, $\chi(0) = 5.3085 \pm 0.004 \times 10^{-4}$ mA^{-2}, and offset current $I_{\text{off}} = -15 \pm 1$ μA. Uncertainty on $\chi(0)$ and I_{off} are statistical, and the uncertainty on $\partial_I V$ is systematic, due to uncertainty in series resistors leading to the sample. Note this measured $\partial_I V$ includes the resistances of everything after the bias-T, including a circuit board, wire bonds, and on-chip leads / contacts, so this is an upper bound on the wire resistance.

bias range ($I_0 < 5$ mA).

We can also use the resistance to place a bound on the local heating from our green excitation laser. Centering a 2 mW continuous beam on a similar nanowire (260 nm wide, 5.2 μm active region length, $R_0 = 545\ \Omega$) produces a resistance change of 0.7 Ω, corresponding to an average temperature change $\lesssim 0.4$ K. If we assume all of this heat remains confined to within the 280-nm-wide green spot, the local temperature change would be $\lesssim 8$ K. Additionally, the maximum continuous power we apply for this study is 0.4 mW, so a more accurate upper bound is $\lesssim 1.6$ K. Finally, while addressing the NV, the beam is focused 400 nm *away* from the center of the wire, further reducing the expected heating. We corroborate this by performing FMR with and without the full 2 mW centered on the wire, observing identical spectra (within our statistical noise).

Estimating RF current from rectified voltage

Knowing $\chi(0)$, we can, in principle, use the measured rectified voltage (Eq. 2.24 rewritten)

$$\langle V\rangle = I_0\left(\partial_I V\right)\left(1+\chi(0)I_0^2+\frac{1}{2}\left[\chi(0)+2\chi(\omega)\right]I_1^2\right) \tag{2.44}$$

to estimate the RF current I_1. Figure 2.11(a) shows a "typical" spectrum of just the RF-induced rectified voltage

$$\begin{aligned}\Delta\langle V\rangle &= \langle V\rangle - \left[\langle V\rangle\right]_{I_1=0}\\ &= \frac{1}{2}\left(\partial_I V\right)\left[\chi(0)+2\chi(\omega)\right]I_0 I_1^2\end{aligned} \tag{2.45}$$

as recorded with a chopped lock-in technique at 265 Hz [216][5], with a bias $I_0 = -2.04$ mA, a nominal power -5 dBm (~ 0.5 mA into the nanowire), and field $\mu_0 H_0$ =20.6 mT applied along an in-plane angle $\theta = 5°$ (orange) and 0° (blue) from the wire's long axis and 35° out of plane. Under these conditions, the magnetization dynamics are heavily damped, and the magnetization is saturated approximately along the in-plane short axis ($\hat{y}$) of the nanowire

[5]The only difference from Ref. [216] is that we employ a Wheatstone bridge on the low-frequency port of our bias-T to eliminate common-mode noise from our current source, and use the "single-shot" readout discussed in Sec. 2.11.2.

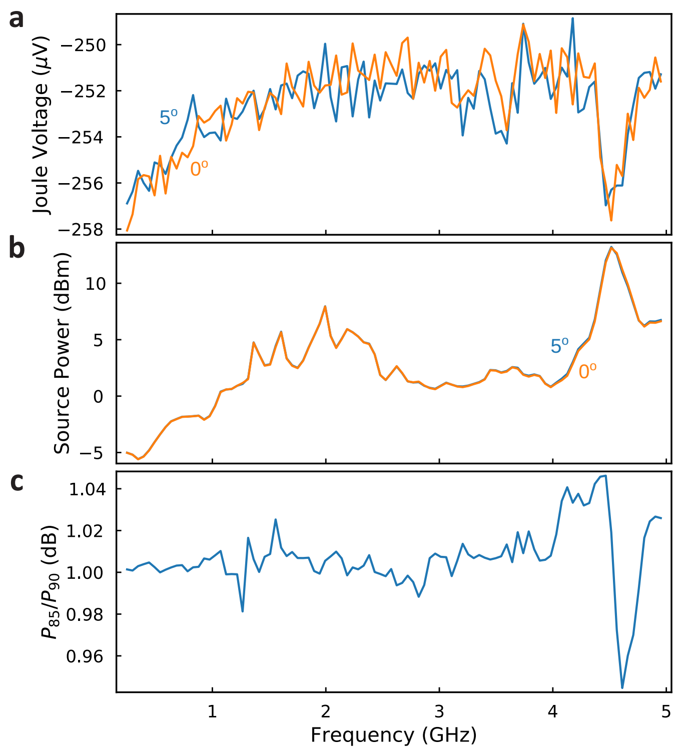

Figure 2.11: Joule heating spectra. (a) “Typical” rectified voltage $\langle V \rangle$ versus RF frequency for bias $I_0 = -2.04$ mA, *nominal* power -5 dBm ($\sim$ 0.5 mA into the nanowire), and field $\mu_0 H_0$ =20.6 mT applied a in-plane angle $\theta = 5°$ (orange) and 0° (blue) from the wire axis and 35° out of plane. The (heavily damped) magnetic resonance near 2.4 GHz should only appear in the off-axis ($\theta = 5°$) case, and evidently represents at most a sub-percent contribution to this signal. (b) Frequency-dependent output power used to compensate for losses in the electronic components between the RF source and nanowire. (c) Ratio of the two curves in (b), showing at most a few-percent difference between the compensation spectra.

(canted a few degrees out of plane).

Importantly, this data was recorded *after* adjusting the output power at each frequency (Fig. 2.11(b)) to ensure a frequency-independent $\Delta\langle V\rangle$ at $I_0 = -4.08$ mA, which allows us to roughly compensate for the strongly frequency-dependent input coupling of our microwave circuitry. Figure 2.11(c) shows the ratio of the powers in b, highlighting that the damped ferromagnetic resonance feature, which should appear near 2.4 GHz in the $\theta = 5°$ spectrum, represents at most a $\sim$1% correction. The high-frequency peak in Fig. 2.11(a) is a noise feature owing to poor coupling near 4.7 GHz. The low-frequency tail is a bias-independent feature that we suspect arises from electronics nonidealities and / or a small Peltier effect. As such, we subtract it from all spectra in the main text. Its presence or absence from the data does not quantitatively or qualitatively affect the conclusions of this work.

Having no reliable means of measuring the loss spectrum of our circuit board, wire bonds (as connected to the sample), and microfabricated leads, we cannot use the measurement in Fig. 2.11(a) to estimate $\chi(\omega)$ directly. We can, however, still solve Eq. 2.45 for the RF amplitude

$$I_1 = \sqrt{\frac{2\Delta\langle V\rangle}{I_0\,(\partial_I V)\,\chi(0)\left(1 + 2\frac{\chi(\omega)}{\chi(0)}\right)}}, \tag{2.46}$$

and, since we expect $0 < \chi(\omega) < \chi(0)$ (i.e., χ is largest at $\omega = 0$), we can constrain the RF current I_1 to the range

$$\sqrt{\frac{2\Delta\langle V\rangle}{3I_0\,(\partial_I V)\,\chi(0)}} < I_1 < \sqrt{\frac{2\Delta\langle V\rangle}{I_0\,(\partial_I V)\,\chi(0)}}, \tag{2.47}$$

representing a maximum systematic error of $\pm$37%. However, the frequency dependence of $\chi(\omega)$ *will* impose a *frequency-dependent* systematic error, which can in principle skew observed ferromagnetic resonance curves. In the following section, we improve upon this estimate by simulating the thermal response of our wire on a diamond substrate.

2.11.3 Modeling the thermal transfer function for our wire

The goal of this section is to simulate the thermal response of our nanowire so that we may more accurately estimate how the Joule-rectified voltage depends on the RF current and DC bias. Inspecting Eq. 2.46, the only quantity of which we do *not* have an independent measure is the ratio $\chi(\omega)/\chi(0)$,[6] which the following sections address.

Parallel resistor model

To model the thermal response of our multilayer nanowire to an oscillatory current, we first must estimate the current carried by each layer. We model the Pt and Py layers of the wire as two resistors connected in parallel, with values R_{Pt} and R_{Py}, such that our *total* current through the wire

$$I = I_0 + I_1 \cos\omega t, \tag{2.48}$$

is divided into layer currents

$$I_j = \frac{R}{R_j}\left(I_0 + I_1 \cos\omega t\right) \tag{2.49}$$

for $j \in \{\mathrm{Pt}, \mathrm{Py}\}$, where

$$R \equiv \frac{R_{\mathrm{Py}} R_{\mathrm{Pt}}}{R_{\mathrm{Py}} + R_{\mathrm{Pt}}} \tag{2.50}$$

is the total wire resistance. The dissipated power in each layer is then

$$P_j = \frac{R^2}{R_j}\left(I_0^2 + 2I_0 I_1 \cos\omega t + I_1^2 \cos^2\omega t\right). \tag{2.51}$$

and the first harmonic has amplitude

$$P_{j1} = \frac{2I_0 I_1 R^2}{R_j}, \tag{2.52}$$

Importantly, $P_{j1} \propto I_1$, so the ratio of first-harmonic amplitudes is

$$\frac{P_{\mathrm{Py}1}}{P_{\mathrm{Pt}1}} = \frac{R_{\mathrm{Pt}}}{R_{\mathrm{Py}}}. \tag{2.53}$$

With this oscillatory drive, we expect a steady state solution to cause a (time dependent)

[6] Recall the Fig. 2.11 provides the Joule-rectified voltage $\Delta\langle V\rangle$, I_0 is measured with a series resistor, and $(\partial_I V)\,\chi(0)$ can be estimated as in Fig. 2.10.

temperature change ΔT_j, such that the layer resistances

$$R_j = R_{j0}\left(1 + \alpha_j \Delta T_j\right) \tag{2.54}$$

where I_j is the layer current, R_{j0} is the zero-heat layer resistance, and α_j is the layer's temperature coefficient of resistance. The resistance of the combined nanowire is then

$$R = R_0 \frac{\left(1 + \alpha_{\mathrm{Pt}} \Delta T_{\mathrm{Pt}}\right)\left(1 + \alpha_{\mathrm{Py}} \Delta T_{\mathrm{Py}}\right)}{1 + \frac{R_0}{R_{\mathrm{Py}}}\alpha_{\mathrm{Pt}}\Delta T_{\mathrm{Pt}} + \frac{R_0}{R_{\mathrm{Pt}}}\alpha_{\mathrm{Py}}\Delta T_{\mathrm{Py}}} \tag{2.55}$$

with zero-heat total wire resistance

$$R_0 \equiv \frac{R_{\mathrm{Py}0} R_{\mathrm{Pt}0}}{R_{\mathrm{Py}0} + R_{\mathrm{Pt}0}}. \tag{2.56}$$

Assuming the resistance changes due to Joule heating are a small fraction of the zero-heating values ($\alpha_j \Delta T_j \ll 1$; see Fig. 2.10),

$$R \approx R_0 + \frac{R_0^2}{R_{\mathrm{Pt}}}\alpha_{\mathrm{Pt}}\Delta T_{\mathrm{Pt}} + \frac{R_0^2}{R_{\mathrm{Py}}}\alpha_{\mathrm{Py}}\Delta T_{\mathrm{Py}}, \tag{2.57}$$

and the power amplitudes in each layer (keeping only terms of order $I_j^2 \sim \Delta T_j$) become

$$P_j \approx \frac{R_0^2}{R_{j0}}\left(I_0^2 + 2 I_0 I_1 \cos\omega t + I_1^2 \cos^2 \omega t\right). \tag{2.58}$$

In the presence of these static and oscillatory powers, the layer temperature change

$$\Delta T_j = \left(X_j(0) P_{j0} + P_{j1}\left(X_j(\omega)\cos\omega t + Y_j(\omega)\sin\omega t\right) + X_j(2\omega)\cos 2\omega t\right) \tag{2.59}$$

$$P_{j0} \equiv \left(I_0^2 + \frac{1}{2} I_1^2\right)\frac{R_0^2}{R_j} \tag{2.60}$$

$$P_{j1} \equiv 2 I_0 I_1 \frac{R_0^2}{R_j} \tag{2.61}$$

$$P_{j2} \equiv \frac{1}{2} I_1^2 \frac{R_0^2}{R_j}, \tag{2.62}$$

where $X_j(\omega)$ and $Y_j(\omega)$ are the quadratures of the transfer function for each layer. The instantaneous *total* voltage is then

$$
\begin{aligned}
V &= IR && (2.63)\\
&= R_0\left(I_0 + I_1\cos\omega t\right)\left(1 + \sum_j \frac{R_0}{R_j}\alpha_j X_j(0) P_{j0}\right) && (2.64)\\
&+ R_0\left(I_0 + I_1\cos\omega t\right)\left(\sum_j \frac{R_0}{R_j}\alpha_j P_{j1}\left(X_j(\omega)\cos\omega t + Y_j(\omega)\sin\omega t\right)\right) && (2.65)\\
&+ R_0\left(I_0 + I_1\cos\omega t\right)\left(\sum_j \frac{R_0}{R_j}\alpha_j X_j(2\omega)\cos 2\omega t\right), && (2.66)
\end{aligned}
$$

and the time-averaged voltage can be written as

$$
\langle V\rangle = I_0 R_0\left(1 + \chi(0) I_0^2 + \frac{1}{2}\left[\chi(0) + 2\chi(\omega)\right] I_1^2\right) \tag{2.67}
$$

with the *total* in-phase transfer function

$$
\begin{aligned}
\chi(\omega) &\equiv \sum_j \frac{R_0^3}{R_j^2}\alpha_j X_j(\omega)\\
&= \frac{R_0^3}{R_{\mathrm{Pt}}^2}\alpha_{\mathrm{Pt}} X_{\mathrm{Pt}}(\omega) + \frac{R_0^3}{R_{\mathrm{Py}}^2}\alpha_{\mathrm{Py}} X_{\mathrm{Py}}(\omega). && (2.68)
\end{aligned}
$$

This formula is identical to that of the single-resistor case (Eq. 2.24 of Sec. 2.11.1, identifying $R_0 = \partial_I V$), except that $\chi(\omega)$ is now a weighted average of the layers' individual responses. Not surprisingly, the weighting factors scale as α_j, and increase as the layer resistance R_j is reduced (when a larger fraction of the current flows through layer j). Additionally, for the case of a single layer (of resistance R_0, thermal coefficient α, and transfer function X), this expression simplifies to $\chi(\omega) \to R\alpha X(\omega)$ and we can identify $\partial_T\partial_I V = R_0\alpha$ from Eq. 2.24, as expected.

As mentioned above (see also Eq. 2.46), we are interested in the ratio

$$
\begin{aligned}
\frac{\chi(\omega)}{\chi(0)} &= \left(\frac{X_{\mathrm{Pt}}(\omega)}{X_{\mathrm{Pt}}(0)}\right)\frac{1 + \eta X_{\mathrm{Py}}(\omega)/X_{\mathrm{Pt}}(\omega)}{1 + \eta X_{\mathrm{Py}}(0)/X_{\mathrm{Pt}}(0)} && (2.69)\\
\eta &= \frac{R_{\mathrm{Pt}}^2\alpha_{\mathrm{Py}}}{R_{\mathrm{Py}}^2\alpha_{\mathrm{Pt}}}.
\end{aligned}
$$

Assuming $R_{\mathrm{Pt}}/R_{\mathrm{Py}} = 0.325$ [225] and $\alpha_{\mathrm{Py}}/\alpha_{\mathrm{Pt}} \sim 1.33$ for our system, $\eta \sim 0.15$. As we will show in the following section, $X_{\mathrm{Py}}/X_{\mathrm{Pt}} < 1$ over the frequency range of interest, so we can make a further approximation

$$\frac{\chi(\omega)}{\chi(0)} \approx \left(\frac{X_{\mathrm{Pt}}(\omega)}{X_{\mathrm{Pt}}(0)}\right)\left(1+\eta\left[\frac{X_{\mathrm{Py}}(\omega)}{X_{\mathrm{Pt}}(\omega)} - \frac{X_{\mathrm{Py}}(0)}{X_{\mathrm{Pt}}(0)}\right]\right) \tag{2.70}$$

which illustrates the correction due to the presence of the Py layer is small (as discussed below, it should be $\lesssim 3\%$). Nonetheless, we simulate both layers because there is not much additional overhead.

Finite-element simulation

We perform finite-element simulations (COMSOL) of the nanowire's active region (between the contacts, where the current is concentrated) and the diamond substrate. Figure 2.12(a) shows the simulated geometry, comprising a $L \times W \times H$ diamond substrate (dimensions varied with frequency as discussed below), upon which a 10 nm Py (bottom) / 10 nm Pt (top) nanowire spanning 5.2×0.417 µm^2 is positioned at the center. We assume the heat is primarily dissipated in the constriction (the nanowire), and that the large-area connection to diamond serves as the dominant heat sink in this system; as such we do not bother to include the leads in this study. Including a "standard" convective heat loss of ~25 W/m^{2}K boundary condition on all free surfaces does not significantly alter the results, nor does reducing the mesh density along each axis by a factor of 2.

As per Eq. 2.53, we introduce an oscillatory power of amplitude P_{Pt1}=10^{17} W/m^3 and $P_{\mathrm{Py1}} = (R_{\mathrm{Py}}/R_{\mathrm{Pt}})\, P_{\mathrm{Pt1}}$ and frequency ω to the Pt and Py layers. We let the simulation run until it converges to a steady state, then extract the in-phase (X_j, Fig. 2.12(b)) and out-of-phase (Y_j, Fig. 2.12(c)) amplitudes from the time-dependent temperatures $T_j(t)$.[7]

At lower frequencies, the temperature change penetrates further into the diamond, and a larger diamond volume is required for the results to converge. At the lowest frequency simulated ($\omega = 2\pi\times265$ Hz), for example, we employed the 0.8 mm × 0.8 mm × 0.4 mm volume shown in Fig. 2.12(a), but a small deviation from adiabatic response is still evidenced

[7]Note this single-frequency method is significantly more efficient than performing an impulse response when covering this many decades of frequency.

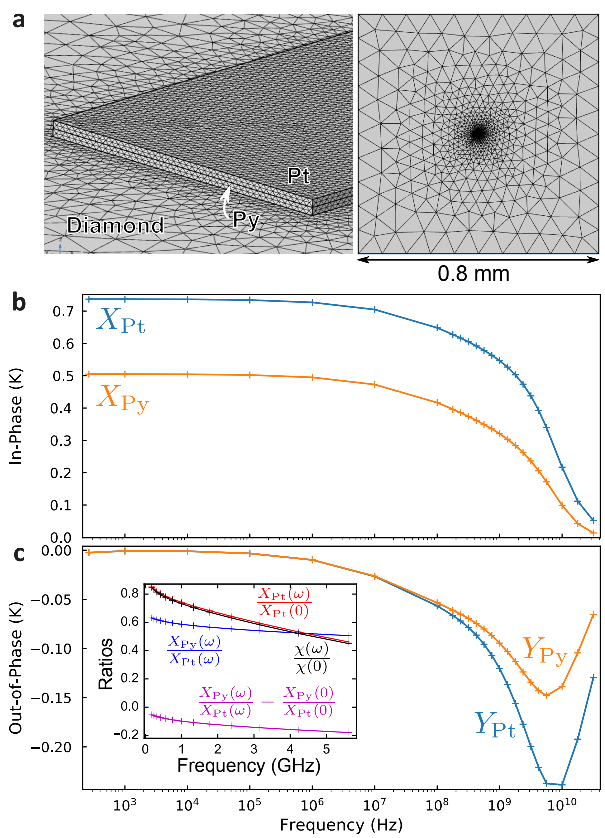

Figure 2.12: Simulated thermal response of Py/Pt nanowire on diamond, assuming a wire length l=5.2 μm, width w=417 nm, Pt and Py thicknesses h=10 nm, resistivities $\rho_{\mathrm{Pt}} = 21.9\,\Omega$-cm and $\rho_{\mathrm{Py}} = 65.2\,\Omega$-cm. (a) Simulation volume for the low-frequency response (left) and nanowire mesh (right). (b) In-phase temperature oscillation amplitude at the drive frequency for the Pt (blue) and Py (orange) layer, for a drive power amplitude $P_{\mathrm{Pt1}} = 10^{17}$ W/m^3 and $P_{\mathrm{Py1}} = 0.336 \times 10^{17}$ W/m^3 in the Py layer. (c) Out-of-phase oscillation amplitude, showing steady-state behavior at low frequencies (where the thermal penetration depth in the diamond is much larger than the wire) and the onset of a lagged response at higher frequencies (where the heat is confined to very near the wire). Inset shows $\chi(\omega)/\chi(0)$ (black) as well as $X_{\mathrm{Pt}}(\omega)/X_{\mathrm{Pt}}(0)$ (red), $X_{\mathrm{Py}}(\omega)/X_{\mathrm{Pt}}(\omega)$ (blue), $\frac{X_{\mathrm{Py}}(\omega)}{X_{\mathrm{Pt}}(\omega)} - \frac{X_{\mathrm{Py}}(0)}{X_{\mathrm{Pt}}(0)}$ (magenta) from Eqs. 2.69 and 2.70.

by a sub-percent out-of-phase response due to integrator-like behavior as heat reaches the boundaries of the diamond. This phase lag returns at higher frequencies ($\omega > 2\pi \times 10^6$ Hz) as the heat ceases to efficiently escape the nanowire.

The inset of Fig. 2.12(c) shows the quantities of interest in Eqs. 2.69-2.70, as well as $\chi(\omega)/\chi(0)$ for the *total* wire assuming $\eta = 0.15$. We can now plug this into our expression for the RF current amplitude (Eq. 2.46 rewritten)

$$I_1 = \sqrt{\frac{2\Delta\langle V\rangle}{I_0\left(\partial_I V\right)\chi(0)\left(1+2\frac{\chi(\omega)}{\chi(0)}\right)}} \tag{2.71}$$

to convert the observed rectified voltage $\Delta\langle V\rangle$ in Fig. 2.11(a) (at $I_0 = -2.04$ mA) to RF current, using the values $\partial_I V = 237.3 \pm 0.3\,\Omega$, $\chi(0) = 5.3085 \pm 0.004 \times 10^{-4}$ mA^{-2} from the fit in Fig. 2.10. Figure 2.13 shows the frequency dependence of I_1 (black curve) along with the absolute calibration range of Eq. 2.47 (shaded region), highlighting the importance of the frequency-dependent thermal response in our system. If we ignored $\chi(\omega)$ as in Ref. [237] (e.g.) we would overestimate I_1 by up to 65%, and miss a systematic variation of $\sim 10\%$ over the probed frequency range. We suspect this correction is smaller in more thermally-isolated systems such as wires on oxide or spin valves, though we note that the thermal transfer function falls off very gradually at high frequencies.

2.12 Macrospin model

In this section we develop a useful toy model in which the magnetization of the Py layer is assumed to be spatially uniform. Section 2.12.1 presents the equations of motion, Sec. 2.12.2 derives the natural frequency for small-angle precession about equilibrium, and Sec. 2.12.3 derives the magnetization's linear susceptibility to general oscillatory torques. Finally, we perform simulations to roughly describe the parametrically driven, large-amplitude dynamics in Figs. 3-4 of the main text in Sec. 2.12.4.

2.12.1 Equation of motion

We employ the Landau-Lifshitz-Gilbert equation in the low-damping limit, with the spin Hall torque from the Pt layer [224]:

$$\begin{aligned}\partial_t \hat{m} &= \gamma_0 \mu_0 \vec{H}_{\text{eff}} \times \hat{m} + \alpha \hat{m} \times \partial_t \hat{m} + \frac{g\mu_B \eta \theta_{\text{SH}} J_{\text{Pt}}}{2et_{Py} M_s} \hat{m} \times (\hat{m} \times \hat{y}) \\ &\approx \gamma_0 \mu_0 \left(\vec{H}_{\text{eff}} \times \hat{m} + \alpha \hat{m} \times \left(\vec{H}_{\text{eff}} \times \hat{m} \right) \right) + \frac{g\mu_B \eta \theta_{\text{SH}} J_{\text{Pt}}}{2et_{\text{Py}} M_{\text{s}}} \hat{m} \times (\hat{m} \times \hat{y}) \,. \end{aligned} \tag{2.72}$$

Here, $\hat{m} = m_x \hat{x} + m_y \hat{y} + m_z \hat{z}$ is a unit vector describing the orientation of the magnetization, γ_0 is the magnitude of the gyromagnetic ratio, μ_0 is the magnetic permeability of free space, $\vec{H}_{\text{eff}}$ is the effective field (discussed below), α is the damping parameter (approximately equal to the Gilbert damping for weak damping and spin transfer torques), μ_B is the Bohr magneton, η is the fraction of incident spins that are absorbed by the Py layer, θ_{SH} is the spin Hall angle of Pt, J_{Pt} is the charge current density in the Pt layer (determined by the parallel resistor model of Sec. 2.11.3), e is the electron charge, t_{Py} is the thickness of the Py layer, and M_{s} is its effective saturation magnetization. The effective field

$$\vec{H}_{\text{eff}} = \vec{H}_0 + \vec{H}_{\text{an}} + \vec{H}_I, \tag{2.73}$$

where $\vec{H}_0 = H_x\hat{x} + H_y\hat{y} + H_z\hat{z}$ is the applied field, the shape anisotropy field

$$\vec{H}_{\text{an}} = -M_{\text{s}}\left(N_{yy} - N_{xx}\right) m_y\hat{y} - M_{\text{s}}\left(N_{zz} - N_{xx}\right) m_z\hat{z} \tag{2.74}$$

$$\equiv -H_{yx}m_y\hat{y} - H_{zx}m_z\hat{z}, \tag{2.75}$$

with N_{ij} being the elements of a demagnetization tensor (assumed diagonal for simplicity, with $N_{xx} + N_{yy} + N_{zz} = 1$), and

$$\vec{H}_I = -aI(t)\hat{y} \tag{2.76}$$

is the spatially averaged field generated by the instantaneous current $I(t)$ flowing through the wire, with proportionality constant a. For our long wire (aligned along x), we assume $N_{xx} \ll N_{yy} \ll N_{zz} \sim 1$, such that $H_{yx} + H_{zx} \approx M_{\text{s}}$ is the effective magnetization.

2.12.2 Small-angle precession frequency

Our first goal is to estimate the resonant frequency for for small-angle precession when the applied field is sufficient to saturate m_y. To do so, we ignore dissipation and current in Eq. 2.72, and include an applied field with $H_x = 0$ (as in the experiment):

$$\begin{aligned}
\partial_t\hat{m} &= \gamma_0\mu_0\vec{H}_{\text{eff}} \times \hat{m} \\
\frac{\partial_t\hat{m}}{\gamma_0\mu_0} &= \left(\left(H_y - H_{yx}m_y\right)\hat{y} + \left(H_z - H_{zx}m_z\right)\hat{z}\right) \times \hat{m} \\
&= \begin{pmatrix} \left(H_y - H_{yx}m_y\right)m_z - \left(H_z - H_{zx}m_z\right)m_y \\ \left(H_z - H_{zx}m_z\right)m_x \\ -\left(H_y - H_{yx}m_y\right)m_x \end{pmatrix}.
\end{aligned} \tag{2.77}$$

We find the equilibrium values m_{x0} and m_{y0} of m_x and m_y by setting $\partial_t\hat{m} = 0$, which gives three equations and three unknowns. Assuming H_y is large enough that $m_x = 0$ leaves only the first equation, which can be written in terms of m_{z0} as

$$\frac{H_y}{\sqrt{1 - m_{z0}^2}} = \frac{H_z}{m_{z0}} + H_{yx} - H_{zx}. \tag{2.78}$$

We note that $H_z \sim 0.5$ T is required to saturate the magnetization along $\hat{z}$ meaning our ~ 10 mT fields will only slightly raise the magnetization out of the plane. As such, we assume $m_{z0} \ll 1$ so that $m_{y0} = \sqrt{1 - m_z^2} \approx 1 - \frac{1}{2} m_{z0}^2$. To first order in m_{z0}, this simplifies to

$$m_{z0} \approx \frac{H_z}{H_y + H_{zx} - H_{yx}}. \tag{2.79}$$

For our system's effective saturation fields $\mu_0 H_{yx} = 7.57$ mT and $\mu_0 H_{zx} = 517$ (see Sec. 2.13), a 35-mT field applied along the NV axis (35° out of plane), $m_{z0} \approx 0.04$ (2.3° out of plane). To find the natural precession frequency ν_{FMR}, we therefore apply the limit $m_x, m_z \ll 1$ and $m_y \approx 1$, to Eq. 2.77, which yields coupled differential equations for m_x and m_z:

$$\frac{\partial_t m_x}{\gamma_0 \mu_0} \approx (H_y + H_{zy})\, m_z - H_z \tag{2.80}$$

$$\frac{\partial_t m_z}{\gamma_0 \mu_0} \approx -\,(H_y - H_{yx})\, m_x, \tag{2.81}$$

with $H_{zy} = H_{zx} - H_{yx}$. Using the trial solution

$$m_x = X_0 \cos(2\pi \nu_{\mathrm{FMR}} t) \tag{2.82}$$

$$m_z = m_{z0} - Z_0 \sin(2\pi \nu_{\mathrm{FMR}} t) \tag{2.83}$$

with real-valued amplitudes X_0 and Z_0 yields

$$2\pi \nu_{\mathrm{FMR}} X_0 \approx \gamma_0 \mu_0 \,(H_y + H_{zy})\, Z_0 \tag{2.84}$$

$$2\pi \nu_{\mathrm{FMR}} Z_0 \approx \gamma_0 \mu_0 \,(H_y - H_{yx})\, X_0, \tag{2.85}$$

from which the amplitude ratio

$$\frac{X_0}{Z_0} = \sqrt{\frac{H_y + H_{zy}}{H_y - H_{yx}}} \tag{2.86}$$

and resonant frequency

$$\nu_{\mathrm{FMR}} = \frac{\gamma_0 \mu_0}{2\pi} \sqrt{(H_y - H_{yx})\,(H_y + H_{zx} - H_{yx})}. \tag{2.87}$$

Importantly, this is the same (Kittel) formula one would arrive at with a purely in-plane field, which makes sense in this small-m_z limit. Also, even for our maximal in-plane field $\mu_0 H_y = 33$ mT, $X_0/Z_0 \sim 4.7$, and this ratio increases at lower fields, diverging at $H_y = H_{yx}$, as expected. As such, the m_z-generated stray field power at the NV (i.e., the quantity responsible for the spin relaxation rates) is at least $(X_0/Z_0)^2 \sim 22$ times smaller than that of m_x (and much smaller at the fields of interest).

2.12.3 Linear susceptibility for magnetization approximately along the in-plane hard axis

We now derive the susceptibility of m_x to an oscillatory drive at frequency ν. Since we know the magnetization is saturated along $\hat{y}$ to good approximation (and behaves as though $H_z = 0$ for our parameter range; see Sec. 2.12.2), we consider an applied field $\vec{H}_0 \parallel \hat{y}$ for simplicity, and include a general infinitesimal drive torque

$$\partial_t \hat{m} = \gamma_0 \mu_0 \left(\delta_x \hat{x} + \delta_z \hat{z}\right) e^{i2\pi\nu t} \tag{2.88}$$

of amplitudes δ_x and δ_z. Equation 2.72 can then be written (replacing the current-induced terms with this torque) as

$$\frac{\partial_t \hat{m}}{\gamma_0 \mu_0} = \left(\vec{H}_0 + \vec{H}_{\text{an}} - \alpha\left(\vec{H}_0 + \vec{H}_{\text{an}}\right) \times \hat{m}\right) \times \hat{m} + \left(\delta_x \hat{x} + \delta_z \hat{z}\right) e^{i2\pi\nu t}. \tag{2.89}$$

In the limit $m_x, m_z \ll 1$ and $m_y \approx 1$ to first order, so this becomes

$$\frac{\partial_t \hat{m}}{\gamma_0 \mu_0} \approx \begin{pmatrix} -\alpha\left(H_y + H_{zy}\right) m_z \\ H_y - H_{yx} \\ -H_{zx} m_z + \alpha\left(H_y - H_{yx}\right) m_x \end{pmatrix} \times \begin{pmatrix} m_x \\ m_y \\ m_z \end{pmatrix} + \begin{pmatrix} \delta_x \\ 0 \\ \delta_z \end{pmatrix} e^{i2\pi\nu t} \tag{2.90}$$

or

$$\begin{aligned}
\frac{\partial_t m_x}{\gamma_0\mu_0} &\approx (H_y + H_{zy})\, m_z - \alpha\,(H_y - H_{yx})\, m_x + \delta_x e^{i2\pi\nu t} && (2.91)\\
\frac{\partial_t m_z}{\gamma_0\mu_0} &\approx -\alpha\,(H_y + H_{zy})\, m_z - (H_y - H_{yx})\, m_x + \delta_z e^{i2\pi\nu t}. && (2.92)
\end{aligned}$$

Using the trial solution

$$\begin{aligned}
m_x &= \tilde{X}_0 e^{i2\pi\nu t} && (2.93)\\
m_z &= \tilde{Z}_0 e^{i2\pi\nu t} && (2.94)
\end{aligned}$$

with complex amplitudes $\tilde{X}_0$ and $\tilde{Z}_0$ yields an in-plane steady state amplitude

$$\tilde{X}_0(\nu) \approx \left(\frac{\gamma_0\mu_0}{2\pi}\right)\left(\frac{\nu_{zy}\delta_z + i\nu\delta_x}{\nu_{\mathrm{FMR}}^2 - \nu^2 + i\nu\Delta\nu}\right) \tag{2.95}$$

with

$$\begin{aligned}
\Delta\nu &\equiv 2\alpha\frac{\gamma_0\mu_0}{2\pi}\left(H_y - H_{yx} + \frac{1}{2}H_{zx}\right) && (2.96)\\
\nu_{zy} &\equiv \frac{\gamma_0\mu_0}{2\pi}\,(H_y + H_{zy}) && (2.97)\\
\nu_{yx} &\equiv \frac{\gamma_0\mu_0}{2\pi}\,(H_y - H_{yx}) && (2.98)\\
\nu_{\mathrm{FMR}} &\equiv \sqrt{\nu_{zy}\nu_{yx}}. && (2.99)
\end{aligned}$$

The linewidth nominally depends on H_y, but H_{zx} is the dominant effect, and so $\Delta\nu$ should remain approximately constant over our (small) field range. Also, torques along $\hat{x}$ and $\hat{z}$ produce qualitatively different lineshapes, in principle enabling a torque vector measurement [224, 238, 239].

Mixdown voltage and FMR fit function

If the applied field is tilted slightly toward $\hat{x}$, the equilibrium magnetization will gain a small component m_{x0}. As long as $m_{x0} \ll 1$, the response $\tilde{X}_0(\nu)$ should not change to first order (by symmetry[8]). However such a tilt *does* provide access to an in-phase anisotropic magnetoresistance (AMR) oscillation with phase delay ψ, amplitude ΔR_{RF}, and in-phase component $\Delta R_{\mathrm{RF}} \cos\psi$ (see Sec. 2.10) proportional to the real part of $\tilde{X}_0$, which can be written (see Eq. 2.95)

$$\mathrm{Re}\left[\tilde{X}_0(\nu)\right] \approx \left(\frac{\gamma_0\mu_0}{2\pi}\right) \frac{\delta_z \nu_{zy} \left(\nu_{\mathrm{FMR}}^2 - \nu^2\right) + \delta_x \nu^2 \Delta\nu}{\left(\nu_{\mathrm{FMR}}^2 - \nu^2\right)^2 + \nu^2 \Delta\nu^2}. \tag{2.100}$$

For small-angle precession, the static change in resistance ΔR_0 should contribute very little to the FMR signal, but would scale as

$$\left|\tilde{X}_0(\nu)\right|^2 \propto \frac{\nu_{zy}^2 \delta_z^2 + \nu^2 \delta_x^2}{\left(\nu_{\mathrm{FMR}}^2 - \nu^2\right)^2 + \nu^2 \Delta\nu^2}, \tag{2.101}$$

which is close in form to $\mathrm{Re}\left[\tilde{X}_0(\nu)\right]$. As such, FMR spectra are well fit by

$$V_{\mathrm{MR}}(\nu) = \frac{a_z \left(\nu_{\mathrm{FMR}}^2 - \nu^2\right) + a_x \nu^2 \Delta\nu}{\left(\nu_{\mathrm{FMR}}^2 - \nu^2\right)^2 + \nu^2 \Delta\nu^2}, \tag{2.102}$$

with free parameters a_z, a_x, ν_{FMR}, and $\Delta\nu$.

Expected spectrum of Brownian magnetization noise

A thermal (Langevin) field [240] is typically assumed isotropic, exerting stochastic, uncorrelated torques with a white noise spectrum in all three dimensions. If the torque power spectral densities of each component are S_T (units of rad^2 sec^{-2} Hz^{-1}), then we expect the power spectral density of m_x to be scaled by the magnitude of the susceptibility squared:

$$\begin{aligned} S_{m_x} &\propto \left|\frac{\nu_{zy}}{\nu_{\mathrm{FMR}}^2 - \nu^2 + i\nu\Delta\nu}\right|^2 S_T + \left|\frac{i\nu}{\nu_{\mathrm{FMR}}^2 - \nu^2 + i\nu\Delta\nu}\right|^2 S_T \\ &\propto \frac{\nu_{zy}^2 + \nu^2}{\left(\nu_{\mathrm{FMR}}^2 - \nu^2\right)^2 + \left(\nu\Delta\nu\right)^2}. \end{aligned} \tag{2.103}$$

[8] The resonant frequency ν_{FMR} increases $\propto m_{x0}^2$ to lowest order, since the anisotropy field maximally opposes the applied field when aligned with $\hat{y}$.

2.12.4 Parametrically driven, large-amplitude oscillations

The transport technique used to measure the signals shown in Fig. 2 of the main text are most sensitive to the most spatially uniform magnetic oscillations. To gain some qualitative intuition about the observed large-amplitude, parametrically driven dynamics, we numerically integrate Eq. 2.72 with $\gamma_0 = 2\pi \times 29.25$ GHz/T (electron g-factor $g = 2.09$ for 10-nm-thick Py [241]), $\eta\theta_{\mathrm{SH}} = 0.055$ [224], layer resistivity ratio $\rho_{\mathrm{Py}}/\rho_{\mathrm{Pt}} = 2.977$, and $t_{\mathrm{Py}} = 10$ nm. From our fits (Sec. 2.13) we use $\mu_0 H_{yx} = 7.57$ mT and $\mu_0 H_{zx} = 517$ mT and effective magnetization $\mu_0 M_{\mathrm{s}} = 525$ mT for consistency. The proportionality constant for current-induced field $a = 1.72$ mT/mA is estimated from the required compensation field at 4.08 mA in Fig. 2 of the main text. In order to achieve a similar threshold for parametric oscillations (i.e., not needing unreasonably large currents), we choose $\alpha = 0.02$, which is approximately half the value estimated from our FMR fits. This discrepancy is under study, but we nominally think it is related to the actual device's nonuniform magnetization and / or other nonidealities such as material contamination (e.g., oxidization) and roughness.[9]

To mimic the red data in Fig. 2(a) of the text, we apply a field $\mu_0 H_0 = 23.5$ mT $\times \left(\sqrt{\frac{2}{3}}\hat{y} + \sqrt{\frac{1}{3}}\hat{z}\right)$ along the NV axis, and current

$$I(t) = I_0 + I_1 \cos(2\pi\nu_1 t) \tag{2.104}$$

with $I_0 = 4.08$ mA, $I_1 = 1$ mA, and ν_1 stepped from 1-3.5 GHz. At each frequency, the magnetization is initialized to within 0.1° of equilibrium (along $\hat{y}$ and canted 1.4° out of plane), and evolved for 100 ns to ensure steady state. The time-averaged change in voltage ΔV_{MR} due to magnetoresistance is then calculated as

$$\begin{aligned}
\Delta V_{\mathrm{MR}} &= \langle I(t)R(t) - I_0 R_0 \rangle & (2.105)\\
&= \langle \left(I_0 + I_1\cos(2\pi\nu_1 t)\right)\left(R_0 + \Delta R(t)\right) - I_0 R_0 \rangle & (2.106)\\
&= \langle I(t)\Delta R(t) \rangle, & (2.107)
\end{aligned}$$

[9] Macrospin models are often surprisingly accurate in describing actual nanostructured systems, but their results should always be considered with caution.

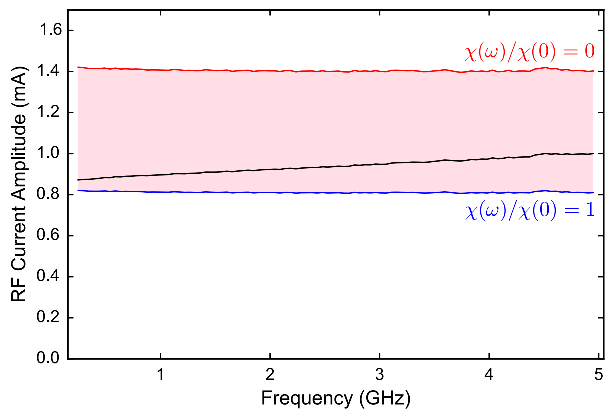

Figure 2.13: RF current amplitude I_1 calibrated from the data in Figs. 2.10-2.11 (Fig. 2 of the main text) and the simulated thermal response in Fig. 2.12 (black). Also shown is the model-independent calibration range (shaded region) bounded by the case $\chi(\omega)/\chi(0) = 0$ (red) and $\chi(\omega)/\chi(0) = 1$ (blue).

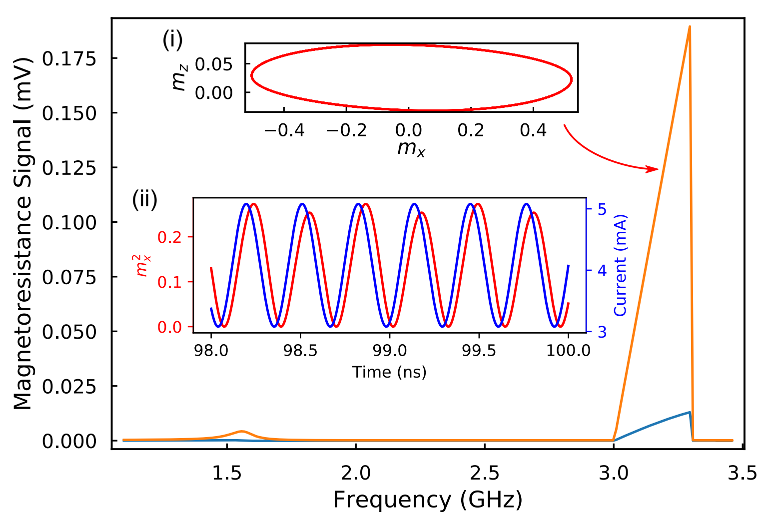

Figure 2.14: Simulated magnetoresistance signal ΔV_{MR} (orange) and the contribution ΔV_{mix} from mixing with RF current I_1 alone (blue). Simulation parameters are listed in the main text. At this value of DC bias $I_0 = 4.08$ mA, the signal is dominated by $I_0 \langle \Delta R(t) \rangle$, which has a different line shape at the fundamental frequency. (i) Trajectory of $\hat{m}$ at $\nu_1 = 3.1875$ GHz, where $\Delta V_{\mathrm{MR}} = 120$ μV. (ii) Time domain showing the relative phase of the resistance ($\propto m_x^2$) and current oscillations.

where R_0 is the undriven resistance, and

$$\Delta R(t) = R_0 \delta_{\mathrm{AMR}} m_x^2 \tag{2.108}$$

is the time-dependent resistance change due to precession, with $R_0\delta_{AMR} = 0.2\,\Omega$. Figure 2.14 shows ΔV_{MR} calculated using an integer number of oscillations in the last 10 ns of each simulation. A large-amplitude parametrically driven peak occurs near the second harmonic of the ferromagnetic resonance above 3 GHz, with a skew toward higher frequencies similar to the data in Fig. 2(a) of the main text. The magnitude is also quantitatively similar, corresponding to in-plane precession about the equilibrium offset ($m_z = 0.025$) amplitude of 30° when $\Delta V_{\mathrm{MR}} = 120$ μV, the trajectory of which is shown in inset (i). The peak is positive because the antidamping spin transfer torque (pointing away from the inset plot's origin) is, on average, larger when the angle is maximal, though the phase of the resistance oscillations lags behind the drive as shown in Fig. 2.14(ii). Finally, we note the presence of a much smaller directly-driven oscillation at ν_{FMR}, arising from the small equilibrium value $\langle m_z \rangle$ and the oscillatory current-induced field $\vec{H}_I$. This feature is visible in Fig. 4(a) of the main text.

Nanowire stray field along NV axis

In this section, we use the NV's field-dependent electron spin resonance (ESR) to estimate the strength of the stray field along the NV axis when the device is statically magnetized along $\hat{y}$. Figure 2.15 shows the photoluminescence (PL) spectra with field $\mu_0 H_0 = 22.5$ mT applied along the NV$_A$ axis for (blue data) NV$_A$, (green data) a reference NV$_{\mathrm{ref}}$ having the same orientation as NV$_A$ but positioned 5 μm from the device, where the stray field is negligible, and (orange data) NV$_A$ after the nanowire's demise, which removed all evidence of ferromagnetism (we suspect due to oxidization or destruction the Py layer). From the difference in fit ESR frequencies (see Table 2.1), we estimate the axial stray field at NV$_A$ most likely lies between 2.1 and 2.6 mT, and we use the "dead device" value 2.5 ± 0.1 mT as our best estimate.

Note the differences in the linewidths and contrasts are due in part to imperfect power coupling to the stripline, and inhomogeneity in the external field can only account for a maximum of 2 MHz of deviation between NV_A and NV_{ref}.

Table 2.1: Fit results from ESR resonances in Fig. 2.15. The net NV axial field is estimated assuming a the free electron gyromagnetic ratio $\gamma_{NV} = 2\pi \times 28.0$ GHz/T.

	$\Delta\nu$ (MHz)	$B_{\parallel}$ (mT)
NV_A, magnetized device	1362.0 ± 0.2	24.409 ± 0.003
NV_A, oxidized device	1222 ± 4	21.9 ± 0.1
NV_{ref}	1230 ± 10	22.1 ± 0.2

Estimating the parametric precession angle

Knowing the strength of the nanowire's stray field at NV_A (Sec. 2.12.4 above) allows us to estimate the parametric oscillation angle $\Delta\theta$ from the reduction in stray field shown in Fig. 3(a) of the main text, using the macrospin approximation. As discussed above, the steady-state trajectory is roughly sinusoidal and highly confined to the xy plane, so we approximate for simplicity

$$m_x \approx \sin\theta(t), \tag{2.109}$$

$$m_y \approx \cos\theta(t), \tag{2.110}$$

$$m_z \approx 0, \tag{2.111}$$

$$\theta(t) \approx \Delta\theta \cos(\pi\nu_{NW} t + \psi), \tag{2.112}$$

where $\theta(t)$ is the time-dependent in-plane angle from $\hat{y}$, $\Delta\theta$ is the steady-state amplitude, and ν_{NW} nanowire's drive frequency, equal to twice the parametric response frequency, and ψ is a steady-state phase shift. In this limit, we can calculate the time-averaged magnetization along $\hat{y}$, which will reduce the stray field experienced by NV_A as

$$\langle m_y \rangle \approx \langle \cos\left(\Delta\theta \cos(\pi\nu_{NW} t + \psi)\right)\rangle \tag{2.113}$$

$$= J_0(\Delta\theta) \tag{2.114}$$

where $J_0(\Delta\theta)$ ($\approx 1 - \frac{1}{4}\Delta\theta^2$) is the zeroth order Bessel function. Figure 3(a) in the main text shows an increase in the $m_s = 0 \to -1$ transition frequency of $\Delta\nu_- = 13$ MHz, which corresponds to a decrease in stray field of $\Delta B_{\text{stray}} \approx 0.5$ mT. Assuming the precession is sufficiently symmetric that the stray field orientation remains the same, the fractional change

$$\frac{\Delta B_{\text{stray}}}{B_{\text{stray}}} \approx 1 - \langle m_y \rangle. \tag{2.115}$$

Using $B_{\text{stray}} = 2.5$ mT from Sec. 2.12.4 at the same external field, we estimate $\Delta\theta \approx 60°$.

Under the same approximations, we can independently estimate $\Delta\theta$ from the magnetoresistance signal

$$\Delta R(t) = R_0 \delta_{\text{AMR}} \sin^2\left(\Delta\theta \cos(\omega_r t + \varphi)\right). \tag{2.116}$$

When current $I(t) = I_0 + I_{\text{RF}} \cos(\omega t)$ is sent through the device, with $I_0 \gtrsim 4$ mA and $I_{\text{RF}} \sim 1$, time-averaging the precession-induced voltage yields

$$\Delta V_{\text{MR}} \approx \frac{1}{2} R_0 \delta_{\text{AMR}} I_0 \left(1 - J_0(2\Delta\theta)\right), \tag{2.117}$$

where we have dropped the comparatively small "mixdown" term involving I_{RF} for simplicity (the I_{RF} term contributes $\lesssim 10\%$ to the total signal for this range of parameters, as shown in supplementary Sec. 2.12.4). In this limit, the peak measurement of $\Delta V_{\text{MR}} = 360$ µV in Fig. 3(a) of the main text ($I_0 = 4.9$ mA, $I_1 = 1.15$ mA, $R_0 \delta_{\text{AMR}} = 0.2\ \Omega$) corresponds to $\Delta\theta \approx 55°$. Similarly, the 120 µV parametric peak in Fig. 2(a) of the main text ($I_0 = 4.08$ mA) corresponds to $\Delta\theta \approx 32°$, in reasonable agreement with the macrospin simulation (Sec. 2.12.4).

2.13 Ferromagnetic resonance frequencies

Because the spin transfer drive and magnetoresistance signal both approximately vanish when the equilibrium value of $\hat{m}$ is (nearly) parallel to $\hat{y}$ (i.e., the field's in-plane angle $\theta = 0$, we cannot measure the ferromagnetic resonance (FMR) frequency ν_{FMR} directly. Instead, we measure $\nu_{\text{FMR}}(\theta)$ for a set of 8 to 9 small angles spanning $\pm 10°$ (maintaining the out-of-plane angle 35° as in the main text), and then fit the resulting frequencies to a symmetric polynomial to estimate $\nu_{\text{FMR}}(0)$ (and a misalignment angle θ_0).

Figure 2.16(a) shows a "typical" set of spin-transfer-driven FMR spectra with applied field $\mu_0 H_0 = 16.5$ mT, taken as discussed in Sec. 2.11.2, with the Joule heating background (Sec. 2.11) subtracted. Due to the frequency-dependence of the drive current (see Sec. 2.11.2), we fit only the data near the resonant feature to Eq. 2.102 to extract the frequency ν_{FMR} and width $\Delta\nu$. As expected, the signal increases with $|\theta|$. Also, as shown in Fig. 2.16(b), the frequency decreases as θ approaches zero, consistent with the shape anisotropy maximally opposing the applied field at $\theta = 0$. Exploiting the mirror symmetry of our geometry, we fit the observed angular dependence in Fig. 2.16(b) to a low-order symmetric polynomial of the form

$$\nu_{\text{FMR}}(\theta) = C_0 + C_2(\theta - \theta_0)^2 + C_4(\theta - \theta_0)^4, \tag{2.118}$$

with fit constants C_0, C_2, C_4, and offset angle θ_0. The offset angle ($\theta_0 = 0.4° \pm 0.1°$ for the shown data set) takes on values within $\pm 0.5°$ of $0°$ over the usable range of applied fields (14-35 mT). Completing the same analysis at each value of applied field produces the zero-angle frequency data $\nu_{\text{FMR}}(0)$ shown in Fig. 2.16(c). Clear fit systematics preclude the trustworthiness of frequencies so estimated below 14 mT. The "reliable" region (dark symbols) can then be fit to a variety of models to estimate material parameters of the permalloy (Py) layer.

2.13.1 Macrospin approximation to resonant frequency

To gain immediate insight, we first assume the magnetization simply behaves as a uniformly-magnetized ellipsoid with equilibrium magnetization $\hat{m}$ approximately parallel to $\hat{y}$. As

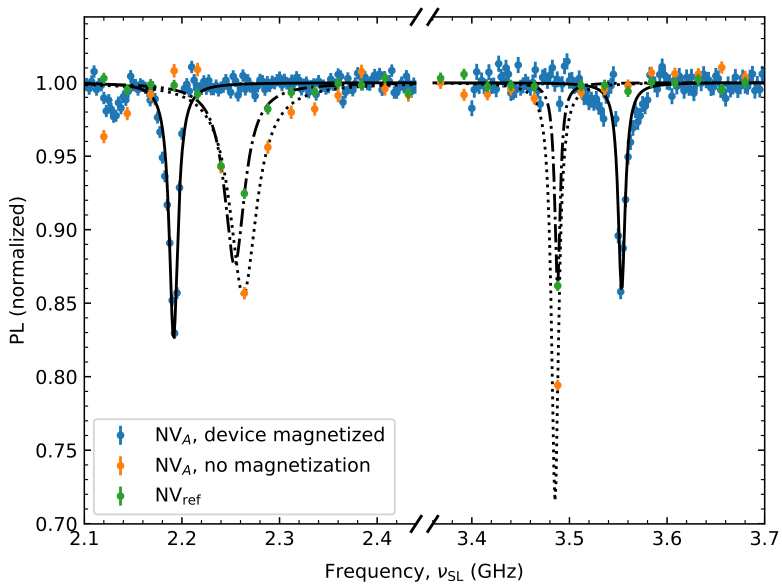

Figure 2.15: Nanowire stray field as measured by ESR. Measurements of the $m_s = 0 \to \pm 1$ transitions of NV$_A$ while the device was magnetized, after the device had oxidized, and of NV$_{\mathrm{ref}}$ are fit to Lorentzian profiles in the solid, dotted and dash-dotted lines respectively.

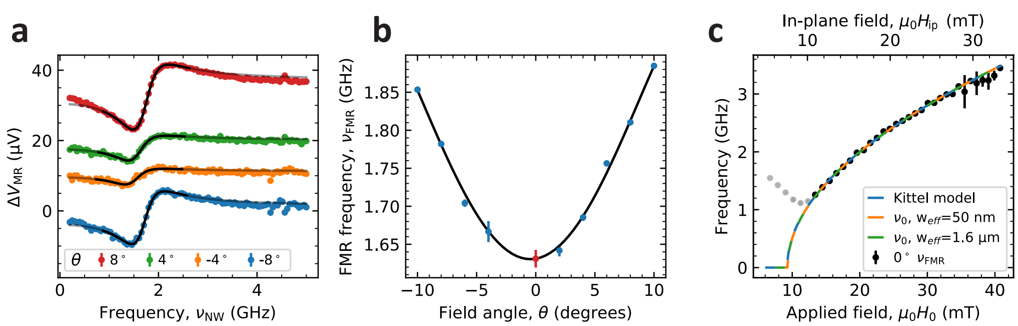

Figure 2.16: Estimating the ferromagnetic resonance (FMR) frequency ν_{FMR} at in-plane angle $\theta = 0$. (a) Spin-transfer-driven FMR spectra for $\theta = \pm 4°$ and $\pm 8°$ for static field $\mu_0 H_0 =$ 16.5 mT applied 35° out of plane, as in the main text. Traces are offset for clarity. Dark lines show Fano fits, and gray lines extend these fits outside the chosen range of frequencies. (b) Fitted frequencies (blue points) over the full range of angles, fit to a symmetric quartic function. (c) Summary of so-estimated $\nu_{\mathrm{FMR}}(0)$ 0°, with the range 14-35 mT fit with a simple Kittel model (blue curve), as well as a lowest-order spinwave model assuming the "extreme" values of fixed effective widths 50 nm (orange curve) and 1.6 μm (green curve).

derived in Sec. 2.12.2, the resonant frequency for our geometry (Eq. 2.87)

$$\nu_{\mathrm{FMR}} = \frac{\gamma_0\mu_0}{2\pi}\sqrt{(H_y - H_{yx})(H_y + H_{zx})}, \tag{2.119}$$

where $H_y = H_0\cos(35°)$ is the in-plane component of the applied field. Fitting the "reliable" range of data (blue curve in Fig. 2.16(c)) yields effective saturation fields $\mu_0 H_{yx} = 7.57 \pm 0.08$ mT and $\mu_0 H_{zx} = 517 \pm 4$ mT. The low value of H_{zx} (nominally close to the saturation magnetization) suggests non-uniform magnetic dynamics and / or other nonidealities of the Py layer.

2.13.2 Lowest-order spinwave approximation to resonant frequency

To get a sense of scale for the potential impact of nonuniform dynamics, we can also perform a fit to an approximate lowest-order (most uniform) spinwave resonance, which has frequency [48, 242]

$$\nu_{\mathbf{k}} = \frac{\gamma_0\mu_0}{2\pi}\sqrt{\left(H_y + M_{\mathrm{s}}\lambda_{\mathrm{ex}}k^2 - H_{\mathrm{d}}\right)\left(H_y + M_{\mathrm{s}}\lambda_{\mathrm{ex}}k^2 - H_{\mathrm{d}} + M_{\mathrm{s}}F_{\mathbf{k}}\right)}, \tag{2.120}$$

where $H_y = H_0\cos(35°)$ is the in-plane component of the applied field, H_{d} is an effective demagnetizing (dipole) field, M_{s} is Py's saturation magnetization, $\lambda_{\mathrm{ex}} = 2A_{\mathrm{ex}}/(\mu_0 M_{\mathrm{s}}^2)$, with exchange constant $A_{\mathrm{ex}} = 1.05 \times 10^{-11}$ J/m [243], k is the magnitude of the spin wave vector $\mathbf{k} = k_x\hat{x} + k_y\hat{y} + k_z\hat{z}$, and

$$F_{\mathbf{k}} = 1 + g_k\left(\sin^2\theta_k - 1\right) + \frac{M_{\mathrm{s}} g_k(1 - g_k)\sin^2\theta_k}{H_y - H_{\mathrm{d}} + M_{\mathrm{s}}\lambda_{ex}k^2}, \tag{2.121}$$

where θ_k is the angle between the equilibrium magnetization orientation $\langle\hat{m}\rangle$ and $\mathbf{k}$, and $g_k = 1 - \left(1 - e^{-kt_{\mathrm{Py}}}\right)/(kt_{\mathrm{Py}})$ with device thickness t_{Py}.

For our thin film, we expect $\hat{m}$ to be approximately uniform along z [242, 244] (we also ignore the small offset in the equilibrium out-of-plane component $\langle m_z\rangle$). The nanowire further constrains the longitudinal wavenumber as $k_x = n_x\pi/L_{\mathrm{eff}}$, with $n_x = 1, 2, 3, \ldots$ and $L_{\mathrm{eff}} \approx 8.05$ µm deviating slightly from the geometrical length due to effective dipolar boundary conditions on the wire [244, 245]. The remaining relevant wave number is often written $k_y = n_y\pi/w_{\mathrm{eff}}$ in terms of the transverse mode number $n_y = 1, 2, 3, \ldots$ and an effective width w_{eff}, which we expect to be *smaller* than the actual wire width when $\hat{m} \parallel \hat{y}$ [48,244,246]. The lowest frequency (and most spatially homogeneous) mode should have $n_x = n_y = 1$, so we treat the resonances measured in transport as having a wave vector $\mathbf{k}_{\mathrm{FMR}} = \frac{\pi}{L_{\mathrm{eff}}}\hat{x} + \frac{\pi}{w_{\mathrm{eff}}}\hat{y}$.

Equation 2.120 effectively contains two fit parameters, $M_{\mathrm{s}}\lambda_{\mathrm{ex}}k^2 - H_{\mathrm{d}}$ and $M_{\mathrm{s}}F_{\mathbf{k}}$, which themselves are composed of three unknown quantities, w_{eff}, M_{s}, and H_{d}. Table 2.2 shows the fit values of H_{d} for a wide range of assumed w_{eff}, with the corresponding fits for $w_{\mathrm{eff}} = 50$ nm (orange) and $w_{\mathrm{eff}} = 1.6$ μm (green) plotted in Fig. 2.16(c) showing negligible deviation from the macrospin model. As expected, as w_{eff} becomes large, the $H_{\mathrm{d}} \to H_{yx}$ and $M_{\mathrm{s}} \to H_{yx}+H_{zx}$ from the macrospin approximation (Sec. 2.13.1). We presume w_{eff} should not be smaller than 50 nm, and the low value of $\mu_0 M_{\mathrm{s}}$ still suggests some nonidealities in the Py layer, which will be the subject of future investigations and higher quality materials deposition. Note that modifying the parameters M_{s}, H_{d}, w_{eff} or A_{ex} by factors of order unity does not affect the key results – observed spin transfer threshold for parametric oscillations, observed stray fields (or lack thereof) at the NV, and observed spin transfer damping – of the main text.

Table 2.2: Fit results of lowest-ordered magnon modes with fixed w_{eff} to data in Fig. 2.16(c).

Fixed w_{eff} (nm)	$\mu_0 H_{\mathrm{d}}$ (mT)	$\mu_0 M_{\mathrm{s}}$ (mT)
50	155 ± 1	709 ± 6
100	50.1 ± 0.3	613 ± 5
200	19.17 ± 0.04	569 ± 5
400	10.81 ± 0.06	548 ± 5
800	8.79 ± 0.08	537 ± 5
1600	8.58 ± 0.09	532 ± 5

2.14 Magnon-induced NV spin relaxation rates

In this section, we use the spin-transfer-free relaxation rates $\Gamma(\nu, H)$ measured at a variety of NV probe frequencies ν and applied fields H to estimate the rates at other values of ν and H (i.e., the color scales in Fig. 5 of the main text). The basic idea can be understood by inspecting the phase space of spin wave modes shown in Fig. 2.17(a). Here, many spin wave mode frequencies $\nu_{\mathbf{k}}$ (where $\mathbf{k} = k_x\hat{x} + k_y\hat{y} + k_z\hat{z}$ is the mode wavenumber; see Sec. 2.13.2) are plotted over our range of applied fields. Importantly, all modes follow the same family of curves to good approximation, meaning one can use a measurement of $\Gamma(\nu, H)$ (taken at the filled symbols) to estimate the relaxation rate $\Gamma'(\nu', H')$ at another location along the nearest $\nu_{\mathbf{k}}$ curve; the quantities that vary the most along these curves are the field, frequency, density of states, and thermal occupancy, all of which are known or can be approximated, as discussed below.

First, we note that the *total* NV spin relaxation rate [148]

$$\Gamma(\nu, H) = \Gamma^0 + \frac{\gamma_{\mathrm{NV}}^2}{2} S_\perp(\nu, H) \tag{2.122}$$

$$\approx \frac{\gamma_{\mathrm{NV}}^2}{2} S_\perp(\nu, H) \tag{2.123}$$

comprises the sum of the NV's (small) internal rate $\Gamma^0_{-(+)} = 64 \pm 7$ Hz (54 ± 12 Hz) (as measured with NV_A at $\mu_0 H_0 = 22.5$ mT after the device magnetization disappeared) and the rate $\gamma_{\mathrm{NV}}^2 S_\perp/2$ ($\sim$ kHz) driven by the magnetization's stray field noise power spectral density $S_\perp(\nu, H)$ (units of T^2/Hz), where γ_{NV} is the magnitude of the NV spin's gyromagnetic ratio and the subscript $\perp$ reminds us that it is the fields perpendicular to the NV axis that drive the transitions. Each spin wave mode contributes noise power in proportion to its thermal occupancy $\bar{n}(\nu_{\mathbf{k}})$, and so we can write

$$S_\perp(\nu, H) = \sum_{\mathbf{k}} \bar{n}(\nu_{\mathbf{k}}) f_{\mathbf{k}} P_{\mathbf{k}}(\nu, H), \tag{2.124}$$

where $f_{\mathbf{k}}$ is a mode-dependent geometrical constant converting occupancy to noise power at the NV (units of T^2/magnon), and $P_{\mathbf{k}}(\nu, H)$ is a unity-normalized density function (units of

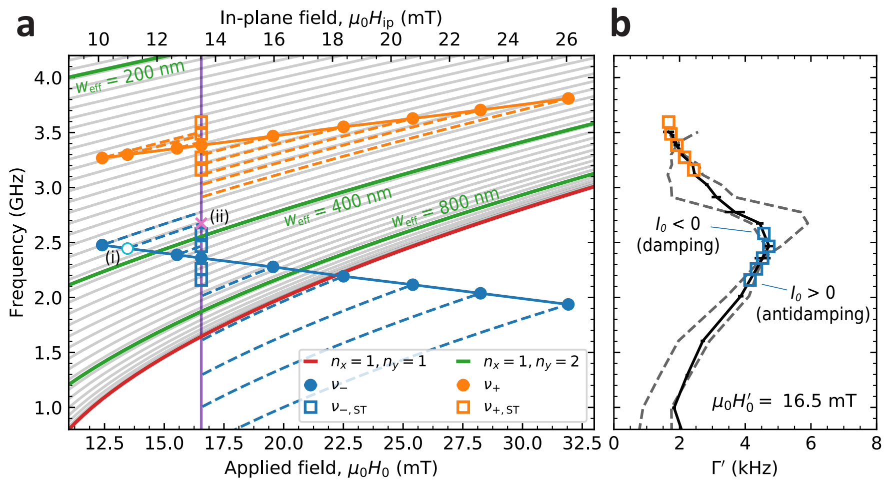

Figure 2.17: Reconstructing the field and frequency dependence of the NV spin relaxation rate Γ' in the absence of spin transfer effects. (a) Spectrum of spin wave mode frequencies for the first transverse mode ($n_y = 1$, $n_x = 1, 2, 3, ...$, gray lines), and NV resonance frequencies ν_+ (orange) and ν_- (blue) when varying only the field (filled circles) or varying the DC bias while compensating the field at the Py layer (hollow squares). The fundamental mode ($n_x = n_y = 1$) is highlighted in red, and the green lines correspond to the second fundamental transverse mode ($n_x = 1, n_y = 2$) for different assumed effective widths w_{eff} (labeled); all modes follow the same family of curves to good approximation (deviating from each other by much less than a spin wave linewidth) over the studied range. The vertical line at $\mu_0 H_0 = 16.5$ mT indicates the field at which the spin transfer effects were probed in Fig. 5(right) of the main text. Dashed lines highlight which NV measurements (filled symbols) are used to estimate Γ' at which frequencies along the vertical line. (b) Reconstructed spin-transfer-free relaxation rates (solid line) along the vertical line cut in (a) with error bars from the bias-free measured values (solid points in (a)). The dashed lines represent the absolute (and quite extreme) bounds of the analysis. Orange (blue) squares correspond to Γ'_+ (Γ'_-) in Fig. 5(b) of the main text.

1/Hz) describing how this power is distributed over the frequency domain (i.e., a normalized version of the mode's power susceptibility, such as Eq. 2.103).

To simplify the analysis, we assume the mode profiles do not change much over our range of applied fields, so that $f_{\mathbf{k}}$ is approximately independent of field. We *do* expect $f_{\mathbf{k}}$ to depend on $\mathbf{k}$ and the exact location of the NV relative to the nanowire, taking on the largest values when $1/|\mathbf{k}|$ is comparable to the wire-NV distance d [210, 213].

To simplify further, we note that the observed linewidth $\Delta\nu \sim 600$ MHz of the fundamental mode is approximately constant over our field range, consistent with the behavior predicted by the macrospin approximation (Sec. 2.12.3). We therefore assume the distributions $P_{\mathbf{k}}(\nu, H)$ depend only on $\nu_{\mathbf{k}}(H)$ and the probe frequency ν. Figure 2.18(a) shows an example $P_{\mathbf{k}}$ for applied field $\mu_0 H_0 = 16.5$ mT along the NV axis. Summing across k_x, we then define a total "linewidth-broadened density of modes" $g(\nu, H)$, which is shown in Fig. 2.18(b).

If we imagine following one of the $\nu_{\mathbf{k}}(H)$ curves in Fig. 2.17(a), we notice two important quantities change – the mode frequencies $\nu_{\mathbf{k}}(H)$ and the density of states $g(\nu, H)$, suggesting that, if we factor these trends from Eq. 2.124, we can write

$$S_{\perp}(\nu, H) = \bar{n}(\nu) g(\nu, H) \sum_{\mathbf{k}} w_{\mathbf{k}}(\nu, H) f_{\mathbf{k}}, \tag{2.125}$$

in terms of a "weighting factor"

$$w_{\mathbf{k}}(\nu, H) \equiv \frac{\bar{n}(\nu_{\mathbf{k}}) P_{\mathbf{k}}(\nu, H)}{\bar{n}(\nu) g(\nu, H)} \tag{2.126}$$

that should be fairly insensitive to the distance traveled along a given $\nu_{\mathbf{k}}$ curve. Of particular relevance to the cooling argument of the main text, Fig. 2.19(a) shows these weights for the direct measurement at point (i) in Fig. 2.17(a) (cyan circles) as well as the location of maximum cooling (ii) (magenta markers). As we have engineered, both peaks occur at the same value of k_x (7 rad/μm), which is a restatement of the fact that we have moved along a $\nu_{\mathbf{k}}$ curve. Importantly, the distributions at these two extremes look very similar, with individual weights differing by at most 34%, as shown in Fig. 2.19(b). We remind ourselves that these weights are multiplied by values of $f_{\mathbf{k}}$ expected to oscillate with k_x underneath a smooth envelope, such that the summed effect is more likely of order the $w_{\mathbf{k}}$-weighted average of the ratio in Fig. 2.19(b) (i.e., ∼3%). The presence of additional transverse modes having comparable values of will *not* have an impact beyond that of Fig. 2.19(b) unless their mode frequencies deviate from the fundamental mode's family of $\nu_{\mathbf{k}}(H)$ curves (gray lines in Fig. 2.17(a)) by an amount comparable to $\Delta\nu$ over the length of the dotted blue line. Even including a more complicated spin wave model or micromagnetic simulations, we do not expect to find modes so strongly deviating from these trends over so small a field range.

We can now convert the directly-measured values of Γ at frequencies ν and fields H (filled circles in Fig. 2.17(a)) into estimates at other values ν' and H' using the ratio

$$\frac{\Gamma'(\nu', H')}{\Gamma(\nu, H)} = \frac{S_\perp(\nu', H')}{S_\perp(\nu, H)} = \frac{\bar{n}(\nu')}{\bar{n}(\nu)} \frac{g(\nu', H')}{g(\nu, H)} \frac{\sum_{\mathbf{k}} w_{\mathbf{k}}(\nu', H') f_{\mathbf{k}}}{\sum_{\mathbf{k}} w_{\mathbf{k}}(\nu, H) f_{\mathbf{k}}}. \tag{2.127}$$

The first ratio $\bar{n}(\nu')/\bar{n}(\nu) = (e^{h\nu/k_BT} - 1)/(e^{h\nu'/k_BT} - 1)$, with Planck constant h, Boltzmann constant k_B, and temperature T. The second ratio can be calculated as in Fig. 2.18, and the final ratio should be comparable to 1, as discussed above. The resulting reconstruction is plotted (solid line) for $\mu_0 H_0 = 16.5$ mT, i.e., the field at which the spin transfer measurements were made in Fig. 2.17(b). Similar curves can be generated at other values of field, as is plotted on the color scales in Fig. 5 of the main text. Also plotted in Fig. 2.17(b) are upper and lower bounds (dashed curves) corresponding to worst-case-scenario systematic errors in the final ratio, calculated by assuming the *only* contributing mode is the one having the *largest* and *smallest* values of $w_{\mathbf{k}}(H')/w_{\mathbf{k}}(H)$ in Fig. 2.19(b). Importantly, the expected bias-dependent changes in $\Gamma'_\pm$ for Fig. 5(b) of the main text (the probe frequencies of which are indicated by orange and blue squares in Fig. 2.19) is much smaller than what is observed, and has the opposite trend with applied current.

Figure 2.20(a) shows the same calculations for effective widths spanning a wide range. As expected, the presence of different transverse mode structure has little effect on these estimates.

Note that, below the fundamental resonance, there is no obvious choice for the blue dashed curves, but there *are* still modes whose tails contribute to $S_\perp$. As such, we have chosen to fix the *difference* from the fundamental mode frequency ν_{FMR} (where the density of modes is

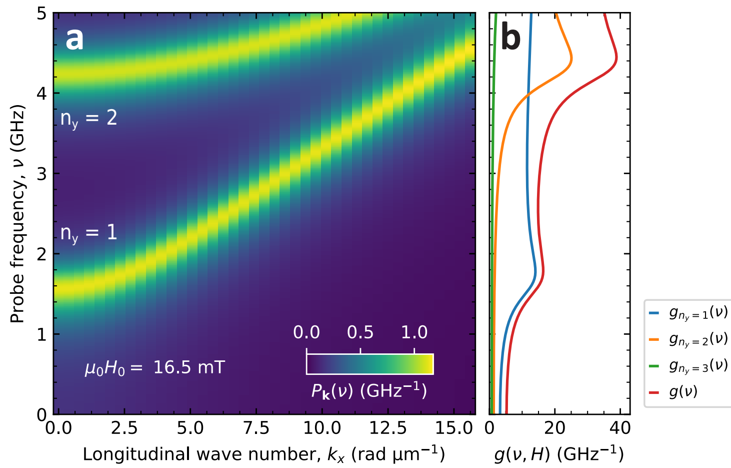

Figure 2.18: Spin wave dispersion and broadened density of modes assuming an effective width $w_{\text{eff}} = 200$ nm. (a) Noise distribution $P_{\mathbf{k}}$ versus frequency ν and longitudinal wavenumber k_x, showing the first ($n_y = 1$) and second ($n_y = 2$) transverse modes at an applied field of $\mu_0 H_0 = 16.5$ mT along the NV axis. (b) Broadened density of modes $g(\nu)$, and the contributions from the first ($g_{n_y=1}(\nu)$), second ($g_{n_y=2}(\nu)$), and third ($g_{n_y=3}(\nu)$) modes.

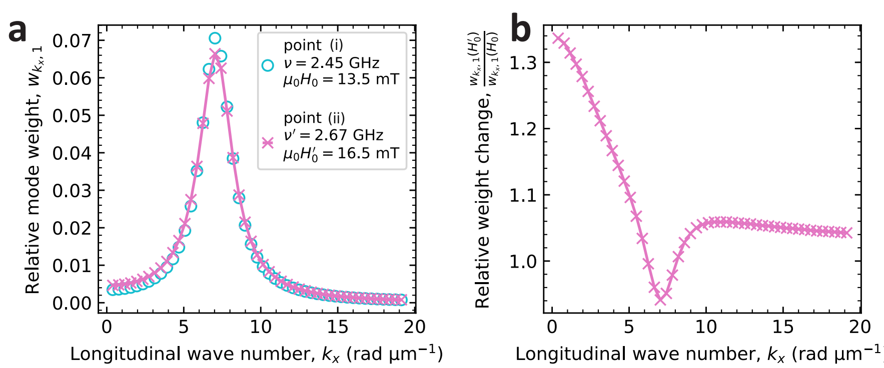

Figure 2.19: Magnon transfer function weights at points (i) and (ii) in Fig. 2.17(a). (a) Relative magnon weights $w_{\mathbf{k}}$ probed at frequencies $\nu_{\mathbf{k}} = 2.45$ GHz (13.5 mT) and $\nu'_{\mathbf{k}} = 2.67$ GHz (16.5 mT) versus k_x, which peaks at $k_x = 7$ rad/µm (as indicated in Fig. 2.18 for $\mu_0 H'_0 = 16.5$ mT). (b) Ratio of weights for these two fields.

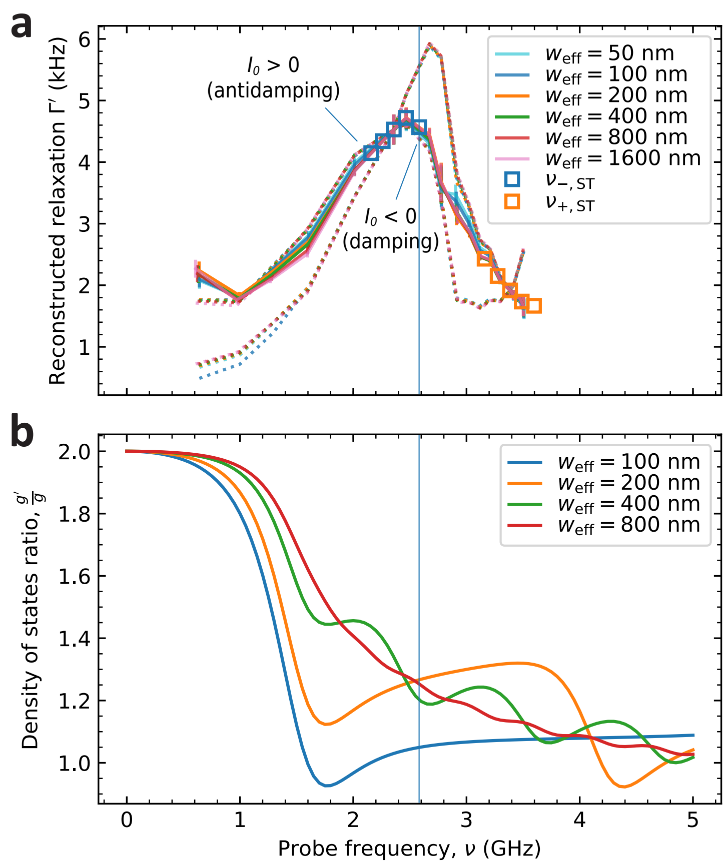

Figure 2.20: Reconstructed relaxation rates Γ' for a range of effective widths w_{eff}. (a) Γ' at $\mu_0 H_0 = 16.5$ mT for different assumed values of w_{eff}, illustrating a minimal impact from changes in mode structure, in particular near the spin-transfer probe frequencies of $\nu_{\pm,\text{ST}}$. (b) Ratio of the linewidth-broadened density of states at the same field for a factor of 2 increase in $\Delta\nu$, illustrating that the total density of states increases at the probe frequency $\nu_{-} = 2.58$ GHz of maximal cooling (vertical line).

highest). In this region, the approximation that the final ratio in Eq. 2.127 is ≈ 1 becomes increasingly incorrect – mainly because the occupation at the probing frequency no longer matches the occupation of the nearest magnon modes – as evidenced by Γ' exceeding the upper bounds at frequencies below $\nu_{\mathrm{FMR}} = 1.64$ GHz.

This "spin-transfer-free" approximation is valid to the specified tolerances provided the linewidth $\Delta\nu$ is constant. When damped by spin transfer, however, we expect the linewidth to broaden, which can redistribute noise away from $\nu_{\mathbf{k}}$ and potentially reduce Γ without cooling. However, as shown in Fig. 2.20(b), the broadened density of modes actually increases under the conditions of maximal spin transfer cooling (vertical line), where the linewidth changes by at most a factor of $\sim$2. In the worst shown scenario, where the effective width $w_{\mathrm{eff}} = 100$ nm, such that the second transverse mode is well above the probe frequency, the broadened density of modes at the probe frequency $\nu_- = 2.58$ GHz still increases due to the tails of the modes away from ν_-. As w_{eff} increases, the higher-order transverse mode frequencies approach ν_-, and g is found to increase by as much as $\sim 25\%$. Therefore, if we assume that $f_{\mathbf{k}}$ does not vary significantly over the resonance linewidth (and / or varies linearly), then the sum in Eq. 2.125 should remain roughly the same or increase (in opposition to the observed trend) as a result of the increased $\Delta\nu$. Combined with the fact that the maximum temperature change due to Joule heating $\Delta T \lesssim 5$ K (see Sec. 2.11.2), we expect this is not a dominant issue.

Chapter 3

Single-spin readout of spontaneous and phase-locked spin torque oscillator dynamics

Adrian Solyom[†], Michael Caouette-Mansour[†], Brandon Ruffolo[†], Patrick Braganca[‡], Jack C. Sankey[†], and Lilian I. Childress[†]

[†] Department of Physics, McGill University, Montreal, Quebec H3A 2T8, Canada

[‡] Western Digital, San Jose CA, 95119 USA

The manuscript presented in this chapter is available on arXiv and has been submitted to the journal of Physical Review Applied.
Citation: arXiv:2307.16049

Recently, a spin torque oscillator (STO) formed from a bilayer of Yttrium-Iron-Garnet (YIG) and Pt was probed with an N-V center [183], causing the spin relaxation of the latter to reach rates of $\sim 1\ \mu\text{s}^{-1}$ when it was in tune with the auto-oscillations of two low-frequency magnon modes. Despite having dimensions much larger than those of our previous Py/Pt device, which displayed no evidence of auto-oscillation, the Yttrium-Iron-Garnet YIG system was able to achieve this behaviour due to its low intrinsic damping when compared to permalloy (Py). Studies of Py/Pt nanowires have shown that such devices have an upper limit on the device dimensions that allows for auto-oscillatory dynamics, particularly at room temperature [35]. In this paper, we manage to create a Py/Pt STO by reducing the length, width and thickness from our previous design. We measured decay rates of $\sim 1\ \mu\text{s}^{-1}$ when the auto-oscillations of the device were resonant with the N-V spin, showing we achieved similar levels of coupling to the YIG/Pt STO system.

To create the smaller devices, we revised our nanofabrication process flow to address the limitations of our previous devices. In our first work (Chapter 2) we used a lift-off procedure—where we evaporated our Py/Pt bilayers on a mask defined by electron beam lithography—that was only able to achieve device widths as small as $\sim$ 400 nm having significant edge burrs. We switched to using an alumina mask and argon ion milling to subtractively define nanowires on diamond with smaller geometries and better material properties. The ion milling reduced the spin contrast of the near-surface N-Vs; we used an oxygen plasma to repair the diamond surface and showed that it did not cause any degradation of the quality of the device.

An additional advantage to reducing the geometry of our device under study was that the normal modes of the nanomaget could be spectrally resolved. Interpreting the magnon occupation from the N-V relaxometry data in our previous study was complicated by the many degenerate spin-wave modes that affected the spin relaxation rate. The power spectral density of spin wave noise was not only dependent on the magnon occupation, but also on the linewidth of the modes which varied as well. By reducing the length of the nanowire from 8 μm down to 3 μm, we are able to resolve two longitudinal magnetic modes with sharp linewidths when they were subjected to antidamping torques. These modes exhibited four distinct methods of driving the N-V ODMR: parametric pumping the device below the STO threshold, parametric phase locking the auto-oscillation above the STO threshold, unlocked auto-oscillations of the STO, and beat tones arising between the parametric drive and the unlocked STO. We also detect evidence of power sapping from auto-oscillations of the lowest mode when we parametrically drive the second mode.

This paper explores the ODMR features observed in the fluorescence of an N-V in close proximity to a parametrically driven STO. We use a combination of ST-FMR measurements and magnetic simulations to understand the N-V fluorescence in this regime, making it possible to use these features for future characterization and study of such devices.

Author contributions

Adrian Solyom: Designed the experiment, acquired and analyzed the data, simulated the measurement, and wrote the manuscript. Contributed equally with Brandon Ruffolo in microfabricating device connections.

Michael Caouette-Mansour: Performed intial characterization of N-Vs in proximity of candidate device to select for microfabricating connections.

Brandon Ruffolo: Contributed equally with Adrian Solyom to the development of microfabricating device connections.

Patrick Braganca: Developed the subtractive nanofabrication process for patterning nanowire devices on diamond.

Jack Sankey: Contributed to experimental design, interpretation of experimental results, manuscript revision, and wrote the magnetic domain solver on which simulations were based.

Lilian Childress: Contributed to experimental design, interpretation of experimental results, and manuscript revision.

Abstract

We employ N-V magnetometry to measure the stray field dynamics of a ferromagnetic permalloy nanowire driven by spin-orbit torques. Specifically, we observe the optically detected magnetic resonance (ODMR) signatures of both spontaneous DC-driven magnetic oscillations and phase-locking to a second harmonic drive, developing a simple macrospin model that captures the salient features. We also observe signatures of dynamics beyond the macrospin model, including an additional ODMR feature (associated with a second SW mode) and one mode sapping power from another. Our results provide additional insight into N-V-spin wave coupling mechanisms, and represent a new modality for sub-wavelength N-V scanned probe microscopy of nanoscale magnetic oscillators.

3.1 Introduction

When compared to architectures employing field-effect transistors, logical devices using spin degrees of freedom to store and carry information show promise for energy-efficient processing [5, 59, 100, 247]. Moreover, the non-linear nature of such magnetic devices offers potential new avenues for massively parallel neuromorphic computing [71–74, 78–80]. The development of this new technology requires characterization methods appropriate for a range of devices, such as logic gates [59] and oscillator arrays [248]. Established techniques such as magnetoresistive readout [26, 32, 84–86], Brillouin light scattering [103–105], x-ray scattering [249, 250], and time-resolved magneto-optic Kerr effect measurements [100–102] allow for excited magnetic spin-waves (SWs) to be detected and measured in frequency space, but each method naturally causes backaction on the device and / or is limited in spatial resolution. To address these two issues, solid state spins have been developed as atomic-scale, minimally invasive probes of the stray fields surrounding SW excitations. Among spin-based magnetometers, the nitrogen-vacancy (N-V) defect in diamond is currently the most studied, and can be placed within nanometers of the sample, enabling scanned probe readout of SWs with small wavelengths. To date, N-Vs have been used to probe ferromagnetic phenomena, including vortex cores [119, 251, 252], domain walls [162], oscillators [183], magnetic tunnel junctions [184], SW dispersion [160, 189], and SW scattering [253].

In this study, we employ N-V magnetometry to measure the stray field of a metallic ferromagnetic nanowire driven by DC and microwave spin-orbit torques (plus associated magnetic fields) generated by current in a platinum capping layer. Following Refs. [178, 189, 254], we parametrically drive SW modes at twice their natural frequency, directly observing the response in the N-V's optically detected magnetic resonance (ODMR) spectrum at the SW frequency (without directly driving the N-V transistions). To extend previous work, we design the present device with dimensions small enough to suppress Suhl instabilities [34, 255], allowing it to act as a spin-torque oscillator (STO) with large-amplitude SW oscillations driven by DC bias alone. Below the STO threshold current, we observe parametrically driven large-angle precession in the ODMR spectrum, and resolve two SW modes, one of of which produces a signature of auto-oscillation above the threshold current. In this regime, the ODMR spectrum also exhibits evidence of coupling between the modes, as parametrically driving the second saps power from the the first. Furthermore, we identify the ODMR spectral signature of phase locking between auto-oscillations and a second-harmonic drive by comparing our ODMR spectra with a simple model coupling a macrospin [254] to an N-V, and find semi-quantitative agreement with the behavior of the fundamental SW mode. Finally, we perform spin relaxometry with the N-V to observe the magnetic noise from the SW modes as the bias is increased above the STO threshold. The results from this simple testbed system demonstrate the potential utility of N-V magnetometry in STO characterization that should be especially useful when applied in a scanned-probe measurement [125, 126, 187–189].

3.2 Device fabrication and transport characterization

We study Py($Ni_{80}Fe_{20}$, 5 nm)/Pt(5 nm) nanowires with nominal lateral dimensions 3 μm × 0.3 μm fabricated on an electronic-grade diamond substrate (see Appendix 3.6.1 for fabrication details). Figure 3.1(a) shows an optical micrograph of the device after the electrical leads have been deposited with a 300-nm overlap on either side of the nanowire. The dashed area in Fig. 3.1(b) is a confocal fluorescence image taken (by focusing green 532-nm light to a scanned point and collecting red fluorescence with the same objective) before depositing the

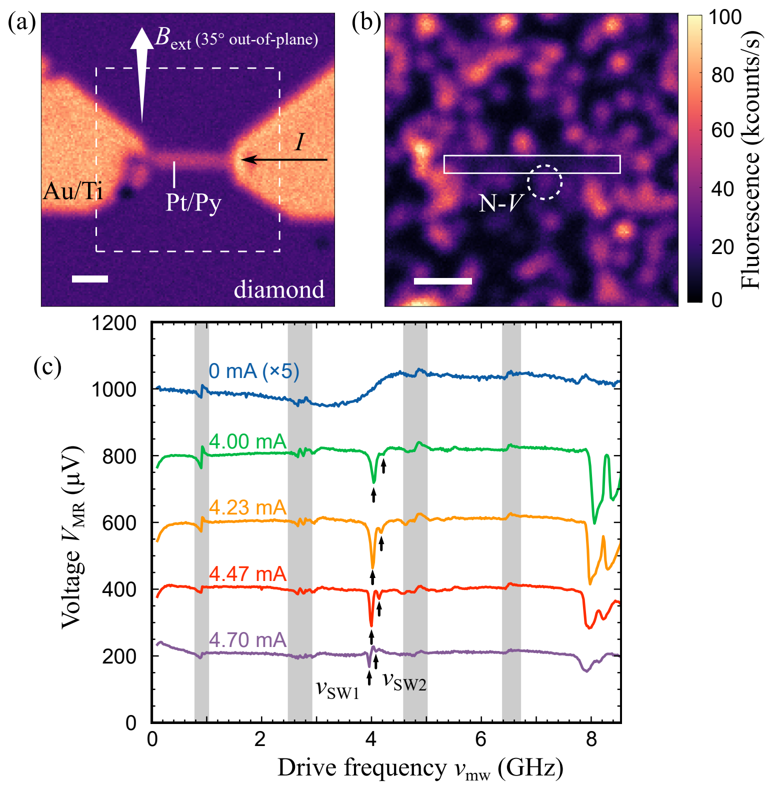

Figure 3.1: **Device geometry and transport measurements** (a) Reflection confocal image of device with overlapping leads attached. The dashed box indicated the region imaged in (b). (b) Fluorescence confocal image of N-V centers near the device, taken prior to the definition of the electrical leads. The white rectangle indicates the location of the device (seen as a shadow in fluorescence), while the dotted circle highlights the location of the N-V center used for measurements in this study. Scale bars in (a) and (b) are 1 μm each. (c) ST-FMR measurements performed with $B_{\text{ext}} = 41$ mT, $I_{\text{mw}} = 1$ mA, and with varying I_{bias}. Arrows mark the narrow synchronized response of the first (second) STO modes at ν_{SW1} (ν_{SW2}). The gray shaded regions indicate frequency ranges with low transmission to the device. Zero-bias features are scaled by a factor of 5 to enhance features.

leads. Individual N-V centers appear as bright spots. The device, which blocks light from entering or leaving the diamond substrate, appears as a shadow highlighted with a white rectangle, and the N-V used to probe the stray field is located within the dotted white circle. Throughout this study, a magnetic field is applied along the diamond's [111] direction, which is orthogonal to the current flow in the nanowire and parallel to the N-V symmetry axis (canted approximately 35 degrees out of plane) [254].

We electrically characterize the magnetic modes by performing spin-transfer ferromagnetic resonance (ST-FMR), using a pulse-modulated lock-in technique [254]. The measurement works by detecting the average voltage V_{MR} resulting from the mix-down between an applied microwave (MW) current and magnetoresistance oscillations associated with magnetic precession (averaged over the volume of the magnetic layer). Figure 3.1(c) shows such measurements performed on the device while sweeping the drive frequency ν_{MW} and applying a magnetic field of $B_{\mathrm{ext}} = 41$ mT with current $I(t) = I_{\mathrm{MW}} \cos(2\pi\nu_{\mathrm{MW}} t) + I_{\mathrm{bias}}$ comprising microwave drive amplitude $I_{\mathrm{MW}} = 1$ mA and a dc bias I_{bias}. At zero bias (top blue curve, scaled by factor of 5 for clarity), we observe a characteristic Fano line shape at 4 GHz, as expected for ferromagnetic resonance driven by a combination of spin Hall torque and field generated by the current [254]. The small signal is due to the minimal drive and readout efficiency occurring when the magnetization is oriented mostly along the in-plane hard axis. (The omnipresent features in the gray regions are artifacts arising from antenna modes of the waveguides and wirebond, and should be ignored.)

With increased DC bias, spin-orbit torques (SOTs) from the platinum layer effectively antidamp the Py layer's magnetic motion, permitting excitation of large-amplitude, narrow-linewidth SW oscillation, and parametrically driven oscillations near twice the fundamental frequency (8 GHz) [254]. In this regime, evidence of two spin-wave modes (SW1 and SW2) can be resolved. A second (subtle) change in lineshape near and above 4.47 mA *might* suggest the onset of DC-driven auto-oscillations phase-locked to the drive (similar to the changes observed in Ref. [84]).

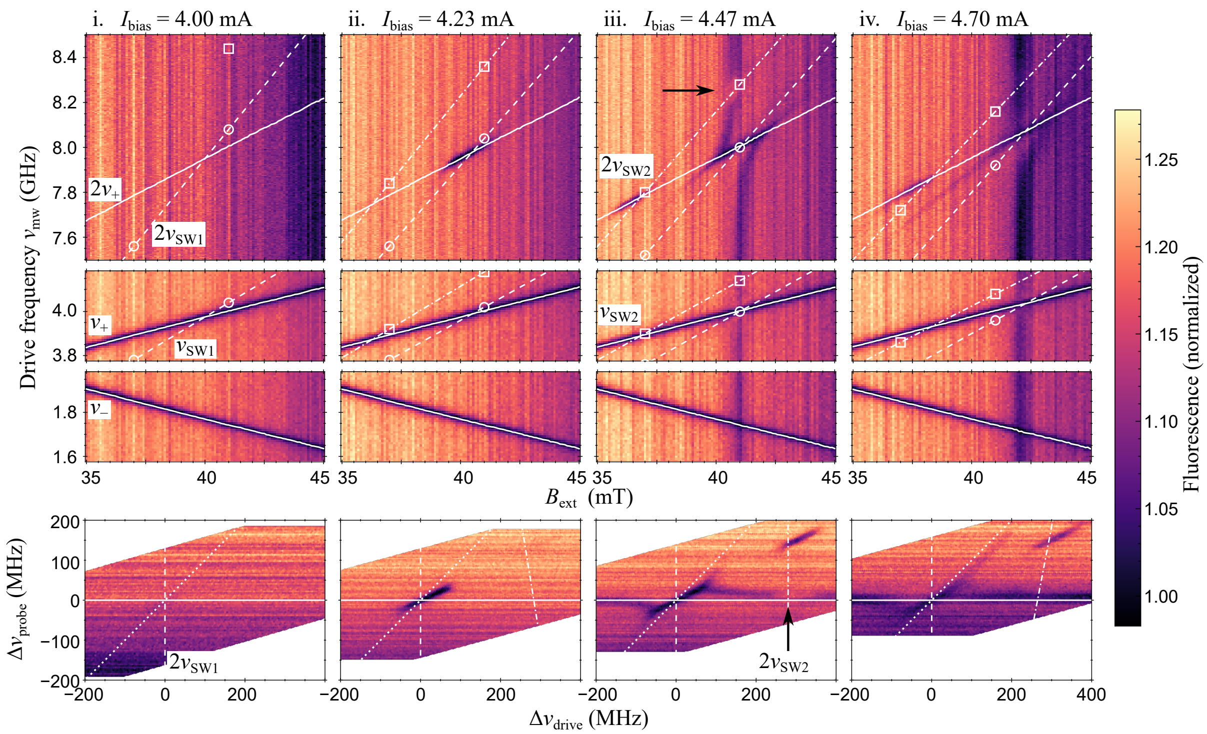

Figure 3.2: **ODMR measurements** (a-c) ODMR measurements of the probe N-V center near the STO resonance. Circles (squares) represent the ν_{SW1} (ν_{SW2}) mode frequency measured in transport (as shown in Fig. 3.1(c)), while the dash-dotted (dashed) lines are guides to the eye connecting the measurements. Solid white lines are the frequencies fit to the ν_+ and ν_- N-V transitions in rows (b) and (c), and represent $2\nu_+$ in the row (a). Each vertical slice of data is normalized by the mixed-state fluorescence of the $\nu_\pm$ transitions. (d) Same data as in (a), but transformed into axes of probe vs drive detunings from the SW1 mode. The dotted diagonal line shows where $\Delta\nu_{\mathrm{probe}} = \Delta\nu_{\mathrm{drive}}$. Columns i-iv show the evolution of the measurement as the bias is swept from 4.0 to 4.7 mA. The black arrows in (a)iii and (d)iii show evidence of power sapping from the STO when parametrically driving SW2.

3.3 ODMR measurements

In contrast to the electrical measurements above, the onset of auto-oscillation and phase locking presents a qualitatively distinctive feature in the ODMR spectrum of a single proximal N-V spin. In this detection modality, the N-V is continuously excited with green 532 nm laser light focused through a 0.95 NA air objective, while the resulting fluorescent emission (filtered by a 635 nm long pass) is collected by the same lens and monitored by a single-photon counter. The optical excitation polarizes the N-V into the $m_s = 0$ spin state, which fluoresces more brightly than the ± 1 states. Then, any oscillating magnetic fields (coherent or noisy) at frequencies near the spin resonance can drive the N-V into a spin mixture with reduced fluorescence.

Figure 3.2(a)-(c) shows fluorescence data obtained by continuously applying a microwave current $I_{\mathrm{MW}} = 0.5$ mA through the wire while sweeping the applied field B_{ext} and microwave frequency ν_{MW}. Columns i-iv are the same data taken at varied I_{bias} to show the transition through the SW's critical current ∼4.4 mA. The frequency ranges in Fig. 3.2(b)-(c) shows the "standard" ODMR response from driving the N-V spin transition at frequencies of $\nu_{\pm}$ (the splitting of which increases with field due to the Zeeman effect) directly with the field from I_{MW}. Each vertical slice is simultaneously fit to two Lorentzian dips of the same width and depth to extract the frequencies $\nu_{\pm}$, as well as the magnitude of the (mixed-spin) fluorescence that occurs on resonance, which is subsequently used to normalize all vertical slices in Fig. 3.2 (this normalization compensates for slow drifts in laser power and alignment during data acquisition), including the data near the second harmonics in row (a). Note that the gradual reduction in fluorescence at higher B_{ext} arises from optically induced spin mixing associated with fields orthogonal to the N-V near the excited-state level anti-crossing [192]. Spin-wave frequencies ν_{SW1} (ν_{SW2}) obtained by ST-FMR are superimposed as open circle (square) symbols and connected with guide lines in Fig. 3.2(b), while the second harmonics of these same frequencies are plotted in Fig. 3.2(a). The solid lines show $\nu_{\pm}$ and their harmonics for reference. In contrast to the magnetoresistive readout above, here we have reduced I_{MW} to 0.5 mA so that it is insufficient to parametrically drive the SW modes with 4 mA of bias (Fig. 3.2(a)i).

Operating near the second harmonic offers an attractive method of probing for magnetic signatures, as the N-V is insensitive to the direct drive from I_{MW}, while maintaining sensitivity to the SW stray fields near $\nu_{\mathrm{SW1,2}}$. For example, as I_{bias} approaches the STO threshold (ii), the expected feature appears in (a) at $B_{\mathrm{ext}} = 40$ mT where the parametrically driven SW1 and N-V frequencies are in resonance [254]. As the bias is increased beyond the STO threshold (iii), several new features emerge. First, SW auto-oscillations directly drive the N-V spin at 41 mT (independent of I_{MW}), when $\nu_{\mathrm{SW1}} \approx \nu_+$, leading to a vertical stripe of reduced fluorescence. The stripe bends as the drive frequency approaches $2\nu_{\mathrm{SW1}}$ producing tails that extend well beyond the resonance condition. As discussed below, these features are reasonably captured by a simple macrospin model, but we can also anticipate the behavior qualitatively. At field strengths where $\nu_{\mathrm{SW1}} = \nu_+$, i.e., when the drive frequency ν_{MW} approaches twice the STO resonance frequency, the magnetic oscillations can phase lock with the drive, pulling their frequency out of resonance with ν_+ and returning the fluorescence to the higher $m_s = 0$ value, e.g., near 8 GHz at 41 mT. When the phase-locked SW mode is driven to resonance with $\nu_{\mathrm{MW}} = 2\nu_+$ again, it drives N-V transitions, and the fluorescence returns to the lower mixed-state value. At fields away from 41 mT, where $\nu_{\mathrm{SW1}} \neq \nu_+$, the non-resonant drive *modulates* the auto-oscillating spin wave, producing sidebands that can drive the NV transitions, generating the tails. This is most easily seen in Fig. 3.2(d), which shows the same data as in (a), but transformed onto axes of N-V "probe" detuning

$$\Delta\nu_{\mathrm{probe}} = \nu_+ - \nu_{\mathrm{SW1}} \tag{3.1}$$

and "drive" detuning

$$\Delta\nu_{\mathrm{drive}} = \nu_{\mathrm{MW}} - 2\nu_{\mathrm{SW1}} \tag{3.2}$$

taken relative to $2\nu_{\mathrm{SW1}}$, with an added dotted line along $\Delta\nu_{\mathrm{drive}} = \Delta\nu_{\mathrm{probe}}$ for reference. As expected for a second-harmonic drive, the parametrically driven and phase-locked dips in (ii) and (iii) occur at probe detunings of $\Delta\nu_{\mathrm{probe}} = \Delta\nu_{\mathrm{drive}}/2$. Above the STO threshold (iii and iv), we also see auto-oscillations as a horizontal line at $\Delta\nu_{\mathrm{probe}} = 0$, while the tails asymptote toward unity slope, consistent with I_{MW} adding modulation sidebands to the SW oscillation. Between the phase-locked and asymptotic regime, the ODMR feature transitions continuously, indicating the drive may be pulling the oscillator frequency without fully phase-locking. We note that this spectral feature is suppressed in (iii) near the first harmonic (in (b)), as expected by symmetry for our geometry; the spin-orbit torques are nearly aligned with the average magnetization of the SW oscillations, and so directly driving its precession is inefficient.

In Fig. 3.2(a,iii), we also observe a second dip at $B_{\text{ext}} = 36$ mT near the resonance condition $\nu_{\text{SW2}} = \nu_+$ for SW2. As such, we associate this feature with parametric driving of SW2. Interestingly, when the N-V is resonant with the auto-oscillations of SW1 (41 mT), we observe a brightening of the fluorescence (arrow in (a,iii) and (d,iii)) while driving near $2\nu_{\text{SW2}}$, suggesting our parametric drive of SW2 has quenched the auto-oscillations of SW1.

Finally, as the bias is further increased (iv), we see the SW features darken and broaden, with the modulation tail visible over a greater range of fields. Additionally, the brightening associated with driving SW2 parametrically while probing SW1 is suppressed, suggesting that SW1 is no longer fully quenched.

3.4 Macrospin modeling

The signatures of parametric drive, auto-oscillations, and phase locking are reasonably captured by a simple model coupling macrospin (uniform) magnetization dynamics to an N-V probe via the stray field. Specifically, the magnetization's unit vector $\mathbf{m}$ follows the Landau-Lifshitz equation

$$\frac{d\mathbf{m}}{dt} = -\frac{\gamma}{\mu_0}\mathbf{m} \times \mathbf{B_{eff}} - \frac{\alpha}{\mu_0}\mathbf{m} \times (\mathbf{m} \times \mathbf{B_{eff}}) + \mathbf{q_{SOT}} \tag{3.3}$$

with gyromagnetic ratio $\gamma = 28$ GHz/T, vacuum permitivity μ_0, Gilbert damping coefficient $\alpha = 0.04$ (estimated from ST-FMR measurements [254]), plus an added spin-orbit torque (Fig. 3.3(a))

$$\mathbf{q_{SOT}} = \frac{\Theta_{\text{SH}}}{M_s L_y L_z^2}\frac{\mu_0 \gamma \hbar}{2e} I_{\text{Pt}} \hat{y} \tag{3.4}$$

with effective spin Hall angle $\Theta_{\rm SH} = 0.1$ in the Pt layer (chosen so that the observed and modelled STO threshold currents match), Py saturation magnetization $M_s = 760$ [256], magnetic layer width $L_y = 300$ nm and thickness $L_z = 5$ nm, and Pt current

$$I_{\rm Pt} = \frac{\rho_{\rm Py}}{\rho_{\rm Pt} + \rho_{\rm Py}} I, \tag{3.5}$$

where $\rho_{\rm Pt} = 21.9$ µΩ · cm and $\rho_{\rm Py} = 65.2$ µΩ · cm [225]. The first term in Eq. 3.3 describes precession about an effective field

$$\mathbf{B_{eff}} = \mathbf{B_I} + \mathbf{B_{ext}} + \mathbf{B_{demag}} + \mathbf{B_{therm}}, \tag{3.6}$$

where

$$\mathbf{B_I} = \eta I \hat{y}, \tag{3.7}$$

is the average current-generated field experienced by $\mathbf{m}$ with efficiency $\eta = 1$ T/A (roughly estimated from the geometry and resistivities of the metals, and consistent with the ST-FMR lineshape [254]),

$$\mathbf{B_{ext}} = B_{\rm ext}\left(\sqrt{\frac{2}{3}}\hat{y} + \frac{1}{\sqrt{3}}\hat{z}\right), \tag{3.8}$$

is the externally applied field (magnitude $B_{\rm ext}$),

$$\mathbf{B_{demag}} = -\mu_0 M_s \mathbf{N} \cdot \mathbf{m} \tag{3.9}$$

is the demagnetizing field with (shape-defined) tensor $\mathbf{N}$, approximated here as that of an ellipsoid with only diagonal elements $N_{xx} = 0$, $N_{yy} = L_z/(L_y + L_z)$, and $N_{zz} = L_y/(L_y + L_z)$ [254,257], and $\mathbf{B_{therm}}$ is a stochastic Langevin field [240] drawn from a Gaussian distribution of standard deviation $\sqrt{4\mu_0 \alpha k_B T/\gamma M_s V \Delta t}$ at each time step (of duration Δt) and dimension separately, with Boltzmann constant k_B, temperature $T = 300$ K, and magnetic volume $V = L_x L_y L_z = 4.5 \times 10^{-21}$ m^3 (estimated from the nominal Py dimensions). The second term in Eq. 3.3 describes the magnetization's descent down the potential energy gradient due to damping α. For each applied field and drive current, we allow the simulation to reach a steady state, then average the power spectral densities over 16 iterations of $T_{\rm sim} = 20$ µs each.

Once the time-dependent magnetization is computed, the resulting N-V dynamics are modeled from the local field at the position of the N-V, comprising the static applied field $\mathbf{B}_{\mathrm{ext}}$, the Oersted field $\mathbf{B}_{\mathrm{Oe}}$ from the current in both layers of the wire, and the dipolar field $\mathbf{B}_{\mathrm{dip}}$ from the magnetic layer. The Oersted field is computed assuming translational symmetry along $\hat{x}$, while the dipolar field is obtained by assuming uniform magnetization of the Py along $\mathbf{m}$ and integrating over the layer's volume (see Fig. 3.3(b)). We use $\mathbf{r_{NV}} = -(240, 300, 60)$ nm for the position of the N-V probe relative to the center of the device, estimated from the optical measurements in Fig. 3.1(b) (determines xy) and SRIM calculations to determine the implantation depth [254]. The resulting time-dependent field at the N-V is then used to calculate three relevant quantities: First, the N-V spin transition frequency is set by the time-averaged field

$$\langle B_j \rangle = \frac{1}{T_{\mathrm{sim}}} \int_0^{T_{\mathrm{sim}}} \mathbf{B}_{\mathrm{dip}} \cdot \mathbf{e}_j dt, \tag{3.10}$$

where T_{sim} is the simulation's duration and $\mathbf{e}_j$ are three orthogonal unit vectors

$$\mathbf{e}_X = \hat{x} \tag{3.11}$$

$$\mathbf{e}_Y = \frac{1}{\sqrt{3}}(\hat{y} - \sqrt{2}\hat{z}) \tag{3.12}$$

$$\mathbf{e}_Z = \frac{1}{\sqrt{3}}(\sqrt{2}\hat{y} + \hat{z}) \tag{3.13}$$

reckoned relative to the N-V symmetry axis $\mathbf{e}_Z$; second, the Rabi frequency

$$\Omega_R = 4\pi\gamma_{NV} \frac{\int_0^{T_{\mathrm{sim}}} \mathbf{B}_{\mathrm{dip}} \cdot \sigma(\nu_{\mathrm{MW}}/2) dt}{\int_0^{T_{\mathrm{sim}}} \sigma(\nu_{\mathrm{MW}}/2) \cdot \sigma(\nu_{\mathrm{MW}}/2) dt} \tag{3.14}$$

is calculated from coherent, synchronized magnetic oscillations at half the microwave drive frequency ν_{MW}, where $\gamma_{NV} = 28$ GHz/T is the N-V spin's gyromagnetic ratio and $\sigma(\nu) = e^{i2\pi\nu t}\mathbf{e}_X + ie^{i2\pi\nu t}\mathbf{e}_Y$ is the transverse component of the spin's co-rotating frame; third, the

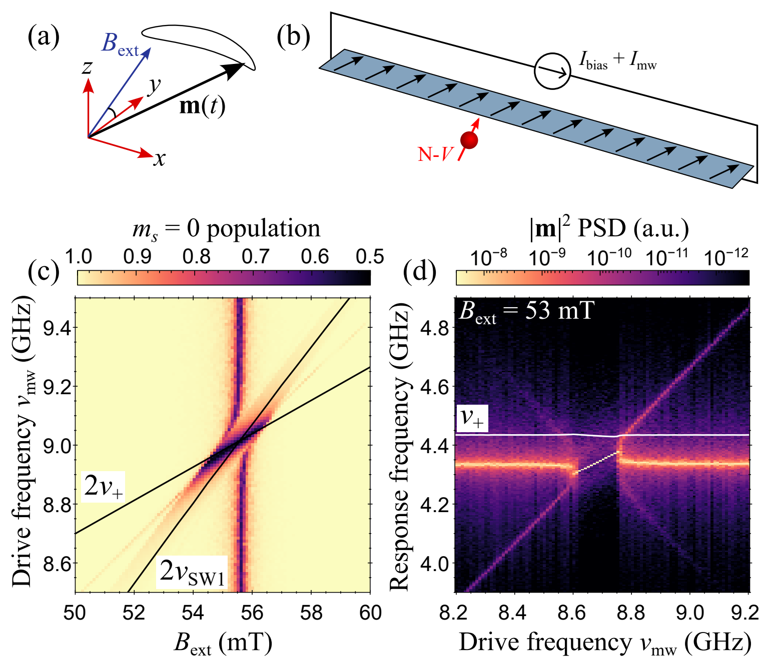

Figure 3.3: **Simulated ODMR** (a) Typical large-amplitude trajectory of the magnetization $\mathbf{m}(t)$ in the macro-spin simulation. (b) The time-varying magnetic field at the N-V probe location—which determines its population and fluorescence—arises from the magnetic layer's integrated dipolar field and the Oersted field from applied currents. (c) Calculated $m_s = 0$ population when the nanowire is driven with $I_{\text{bias}} = 4.47$ mA and $I_{\text{mw}} = 0.5$ mA, which reproduces the STO "vertical stripe", phase locking region, and modulation sideband tails observed in Fig. 3.2(a)iii. (d) Power spectral density (PSD) of the macro-spin model under the same conditions as (c), with a fixed magnetic field of $B_{\text{ext}} = 53$ mT, clearly showing the phase-locked region from 8.6-8.75 GHz drive, frequency pulling near this region, and the modulation sidebands outside this region. The white line shows the N-V frequency, which is only slightly affected by the changing average magnetization.

induced relaxation rate

$$\Gamma_1 = 4\pi\gamma_{NV}^2 T_{\text{sim}} \left| \frac{\int_0^{T_{\text{sim}}} \mathbf{B}_{\text{dip}} \cdot \sigma(\nu_+) dt}{\int_0^{T_{\text{sim}}} \sigma(\nu_+) \cdot \sigma(\nu_+) dt} \right|^2 \tag{3.15}$$

is found from the transverse field noise spectrum at the transition frequency ν_+. With these parameters, we can estimate the steady state $m_s = 0$ population using a two-level optical Bloch equation [115] (see Appendix 3.6.3).

By varying the applied field and drive frequency, we simulate data in Fig. 3.3(c) over the same parameter range as the measurement in Fig. 3.2(a,iii). For the chosen parameters, the simulation provides somewhat quantitative agreement with the key features in the measured ODMR spectrum, though there are some exceptions. First, the macrospin approximation precludes additional SW modes or associated interactions. Second, the simulated resonance between the N-V and the magnet occurs at higher fields than experimentally observed, since the macrospin mode generally has lower frequency than a spatially varying mode that is "stiffened" by the exchange field.

Despite this, our simple toy model validates the above interpretation of the ODMR signatures associated with phase-locking and freely-oscillating STO regimes, including frequency pulling near the phase locking regime, and a strong phase-locked response at $2\nu_+$. We also clearly see the modulation sidebands occurring at the expected frequencies. To make these features more explicit, Fig. 3.3(d) shows the power spectral density (PSD) of the simulated macrospin (the summed contributions of $\mathbf{m}$'s x-, y-, and z-components), with the same axes as those of Fig. 3.2(d), but a color scale associated with $\mathbf{m}$ instead of N-V fluorescence. At $\nu_{\text{MW}} = 4.35$ GHz, we observe the expected free-running STO, whose frequency is pulled down as the drive approaches 8.6 GHz, at which point the magnetization locks phase with the drive, following the frequency $\nu_{\text{MW}}/2$ until it unlocks at 8.75 GHz drive, where the STO is again free-running at a higher-than-unperturbed frequency. Modulation sidebands appear when the response (probe) and drive detunings are equal, as expected. As a caveat, note that this comparison is only rigorously valid outside the phase-locked regime, since, within it, the large Rabi frequency of the magnetization drive broadens the N-V's ODMR linewidth rather than producting a delta-function frequency response expected from a coherent oscillation.

3.5 Lifetime measurements

Finally, we can study STO dynamics in the absence of microwave driving by performing all-optical relaxometry with the N-V probe. Specifically, we perform lifetime measurements using the pulse sequence shown in Fig. 3.4(a), first initializing the N-V into $m_s = 0$ with a 532 nm laser pulse, then allowing variable "dark" evolution time τ between 5 and 25 μs, and finally reading out the new spin state with another laser pulse. The signal fluorescence is normalized to the counts measured during a later "reference" time to minimize slow drifts in the optical paths. A simplified single-decay model (Fig. 3.4(b)) is used to extract the relaxation rate Γ_+ assuming that the STO is the dominant source of relaxation during the evolution time and that it only drives relaxation between spin states 0 and +1.

Figures 3.4(c) and (d) show the fluorescence from the relaxation measurements with $\tau = 5$ and 25 μs as the external field and bias are swept. Open circles (squares) shown the bias and magnetic field conditions where the probe and spin-wave frequencies are in resonance $\nu_+ = \nu_{\mathrm{SW1}}$ ($\nu_+ = \nu_{\mathrm{SW2}}$). Immediately apparent are the dips in fluorescence that occur at biases near and above the STO thresholds. (Note that the apparent increase in fluorescence above $I_{\mathrm{bias}} = 4.5$ mA in Fig. 3.4(d) is an artifact of the normalization procedure: when Γ_+ exceeds the polarization rate during the laser pulse, the initialization fidelity is diminished, which reduces the reference counts, increasing the normalized signal.)

Next, we fit time-series data spanning 5 μs $< \tau <$ 25 μs at each applied field and bias to a single-exponential decay in order to extract the relaxation rate Γ_+ shown in Fig. 3.4(e). We note that, while the all-optical relaxometry approach is experimentally simple to implement, parameter extraction from the fluorescence measurements is susceptible to crosstalk from other noise sources, such as spin mixing between 0 and -1 states near the excited-state level anti-crossing at $B_{\mathrm{ext}} = 50.4$ mT during optical pumping. Furthermore, the restriction of $\tau \in [5, 25]$ μs limits our ability to discern relaxation rates far outside the range 0.04 to 0.2 μs^{-1}. Nevertheless, the simplistic approach to decay fitting is in agreement with our interpretation of the N-V probing two spin-wave modes and confirms the STO threshold at $I_{\mathrm{bias}} = 4.3$ mA above which the measured magnetic-noise-induced relaxation rate increases by orders of magnitude. The measured value $\Gamma_+ > 1$ μs^{-1} when SW1 undergoes auto-oscillation

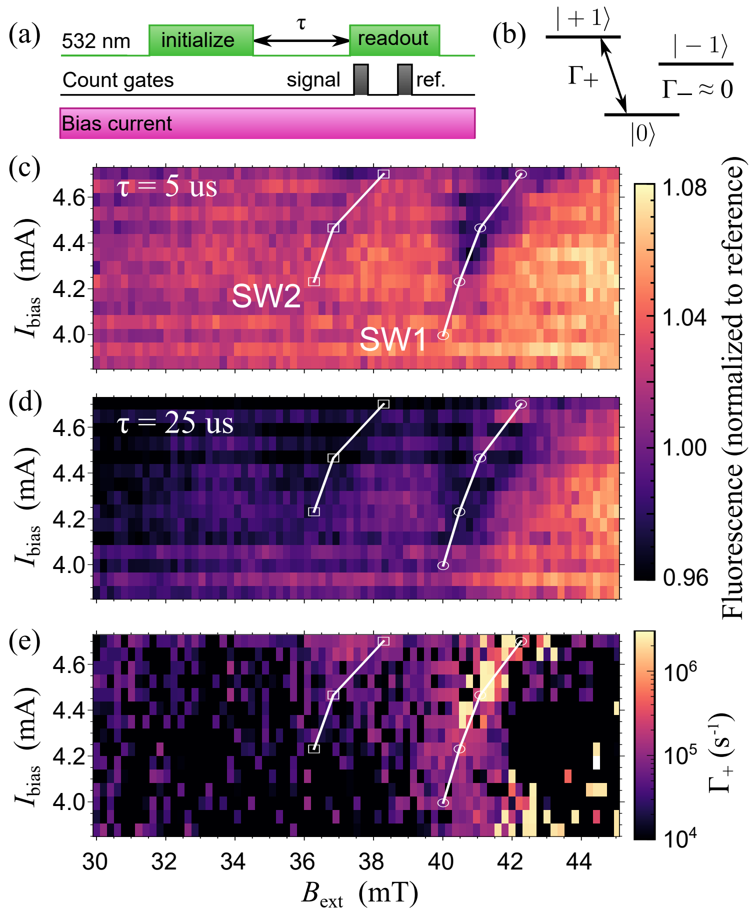

Figure 3.4: **Relaxation measurements** (a) Pulse measurement scheme used for relaxometry. (b) Simplified population relaxation rate diagram. (c), (d) Measured fluorescence during relaxometry for $\tau = 5$ µs and $\tau = 25$ µs, respectively. Fluorescence is normalized by the "reference" counts, and decreases when the the magnetic noise from a SW mode is resonant with the N-V. (e) Results to fitting a single-exponential decay model to the fluorescence data using $\tau \in \{5, 10, 15, 20, 25\}$ µs. Open circles (squares) denote the resonance conditions between the N-V and SW1 (SW2) for (c), (d) and (e).

are also consistent with the rates needed to form the features seen in ODMR, since the relaxation rates required to see any features in the latter must be comparable to the spin polarization rate of ~ 5 MHz from optical pumping.

3.6 Conclusion

We report N-V ODMR and spin relaxation measurements of a free-running spin torque oscillator (STO), and the ODMR spectral signatures of parametric phase-locking, near resonant frequency STO frequency pulling and modulation, and the quenching of one STO mode by another spin wave (SW). The interpretation of all but the last (multi-SW) feature are validated by a simple macrospin simulation. Beyond these demonstrations, pulsed ODMR might enable distinguishing between coherent phase locking and noisy auto-oscillations, and relaxometry protocols can be improved and expedited with MW spin preparation and adaptive pulse pattern generation [149].

To maximize the utility of these testbed-system results, these techniques should be implemented in scanning probe systems, enabling one to resolve the spatial distribution of SW modes below the diffraction limit of laser light. In particular, this would complement and improve upon existing Brillouin light scattering techniques used to determine the localization of mutual synchronization in STO arrays [39]. Even using standard ODMR, we demonstrate a measurement capable of observing STO dynamics far beyond what is possible with device-scale resistive readout.

Appendix

3.6.1 Device fabrication

We use an electronic grade diamond (element6) with a (001) surface as the substrate for the nanofabricated device. The diamond has been implanted with a densely populated layer of N-V centers created via $^{15}N^+$ ion implantation described in our previous experiment [254]. We fabricate the device in this study using a two-step process. To define the nanowires, 5 nm layers of permalloy and platinum are deposited by electron beam evaporation uniformly over the diamond surface, and a 10-nm-thick alumina mask in the shape of the nanowire is deposited by e-beam lithography and liftoff. The surrounding metal is then removed with an argon ion mill. We find this step greatly reduces the N-V spin state fluorescence contrast, but that an oxygen plasma "asher" can recover the spin contrast without damaging the magnetic structures (see Appendix 3.6.2). Finally, KOH is used to remove the alumina layer, allowing for top electrical contact. We then select devices with a well-coupled N-Vs nearby, and optically re-image their positions relative to the nearby alignment marks (compensating for the systematic drift during their initial patterning, e.g., due to charging effects). Without this realignment step, deviations by up to 1 μm from design specification precludes reliably creating lead overlaps of 0.3 μm.

3.6.2 N-V ODMR contrast recovery

Following the argon ion milling step above, we wirebond a stripline above the diamond approximately 100 μm from the devices of interest and use this to generate microwave fields for testing nearby emitters. We noticed that ODMR contrasts from all N-V centers were reduced by a factor of ∼8 (from 16% to 2%) as shown in Fig. 3.5, presumably from the ion mill step, consistent with an altered surface chemistry known to decrease the charge stability of the negatively charged N-Vs and favor the magnetically-insensitive neutral state [258,259]. To repair the damaged surface termination, we expose the patterned diamond surface to an oxygen plasma [260] from a plasma asher (Nanoplas DSB6000, 400 W RF power, 40 sccm O2 flow, 0.4 Torr chamber pressure at 45°C). By wirebonding a stripline across the surface between each plasma exposure and measuring the ODMR contrast, we observe that the contrast measured over 40 emitters (not the same emitters as before the ion etch) recovers the nominal value after ∼50 minutes of exposure. Note the variation in observed contrast across the sampled N-Vs may be partially due to variation in the local environments, as well as variation in the Rabi frequency, which was not controlled, as each emitter may have a different orientation relative to the microwave magnetic field.

While the plasma asher was shown to repair the measured spin contrast for the near-surface N-Vs, we also verified that the processing was compatible with our fabrication flow. Specifically, we conducted AFM measurements of the alumina/Pt/Py trilayer patterned devices after each exposure, as well as after the alumina was removed by a KOH etch, in order to verify that the plasma did not etch the surface or patterned materials. Additionally, the ashing process was shown to not noticeably affect the magnetization of the Py (eg, by oxidization through the side walls) by measuring the splitting of N-Vs spin resonances (partially set by the dipole field of the Py layer) at two locations near the nanowire after each step. At each step of the process, the so-inferred stray field from the Py was unchanged from the original value within our $\sim 10\%$ measurement uncertainty.

3.6.3 Simulation parameters of ODMR

Following the treatment by Dréau et al [115], we model the N-V steady-state spin population under continuous wave excitation to simulate an analogue of the measured fluorescence. Specifically, we model the steady-state populations p_0 and p_1 of the $m_s = 0$ and $m_s = 1$ states respectively as

$$p_1 = \frac{\Gamma_1 \left[(2\pi)^2(\nu_{\mathrm{MW}} - \nu_1)^2 + \Gamma_2^2\right] + \Gamma_2 \Omega_R^2/2}{(2\Gamma_1 + \Gamma_p)\left[(2\pi)^2(\nu_{\mathrm{MW}} - \nu_1)^2 + \Gamma_2^2\right] + \Gamma_2\Omega_R^2}, \tag{3.16}$$

$$p_0 = 1 - p_1. \tag{3.17}$$

Ω_R and Γ_1 are the Rabi frequency and relaxation rate defined in the main text; $\Gamma_p = \Gamma_p^\infty \frac{s}{1+s}$ is the optically induced polarization rate and $\Gamma_2 = \Gamma_2^* + \Gamma_c^\infty \frac{s}{1+s} + \frac{1}{2}\Gamma_1$ is the spin dephasing rate. These in turn depend on the saturation parameter $s = 0.5$ (corresponding to the optical intensity used in these experiments), the optically induced polarization rate at saturation of $\Gamma_p^\infty = 5 \times 10^6\ \mathrm{s}^{-1}$, the optical cycling rate at saturation of $\Gamma_c^\infty = 8 \times 10^7\ \mathrm{s}^{-1}$, and the inhomogeneous dephasing rate $\Gamma_2^* = 2 \times 10^5\ \mathrm{s}^{-1}$.

As discussed in the main text, we decompose the time-dependent field from the simulated magnetization at the N-V's position into left- and right-circulating drives, which we note can lead to double-counting of the spin flipping dynamics under some parameter ranges. Specifically, when the STO is phase-locked to the parametric drive, the magnet will drive coherent oscillations in the N-V such that $\Omega_R > 0$, but if the drive frequency is exactly resonant with the N-V's harmonic as $\nu_{\mathrm{MW}} = 2\nu_1$ then the Fourier transform definition for

$\Gamma_1 > 0$ also plays a role in mixing the spin. Because this double counting only occurs for values of $|\nu_{\mathrm{MW}} - 2\nu_1| < \Delta\nu_{\mathrm{FFT}}$ (where $\Delta\nu_{\mathrm{FFT}} = 5$ MHz is the resolution of the Fourier transform), we neglect it, as it does not qualitatively change the results.

3.6.4 Transport verification of the STO

To confirm that the fabrication process leads to coherent, free-running STOs with signals detectable by conventional means, we use a spectrum analyzer having a resolution bandwidth of 22 MHz to measure the power spectral density of microwave electrical currents induced by the mixture of oscillating magnetoresistance with the bias currents [32]. Although the device studied in this article was destroyed before we could perform this test, we measured the electrical spectrum in a device from the same chip and fabrication run with lateral dimensions of 6×0.3 μm as shown in Fig. 3.6. As the bias current is increased above the STO threshold of ~ 3.6 mA, a spectral line with a with < 50 MHz linewidth appears and decreases in frequency with bias, consistent with the macrospin model. This measurement further validates that the features in the N-V fluorescence data can be attributed to the auto-oscillations of an STO.

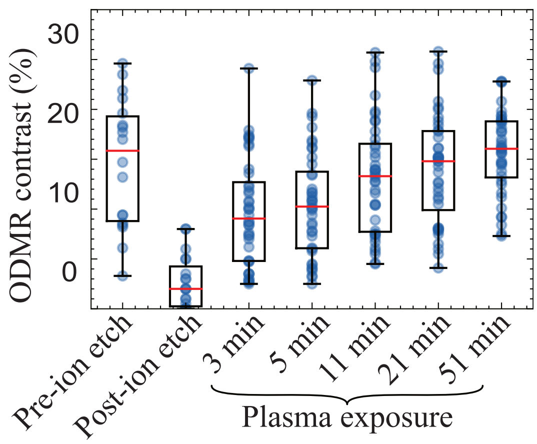

Figure 3.5: **ODMR contrast damage and recovery** Box and whisker plot of measured NV ODMR contrast for each process step. Each dot is a measurement of a fluorescent emitter's ODMR contrast, and the box plot shows the four quadrants in which the data lie.

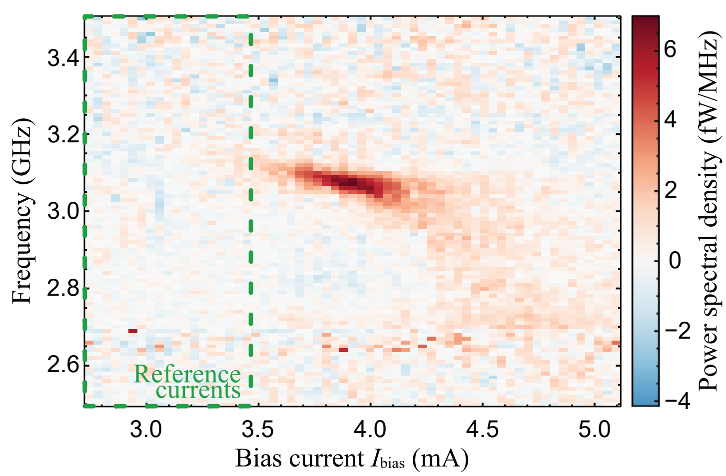

Figure 3.6: **Power spectral density of a second device** Spectrum analyzer measurement of a STO-response from the same chip as the device studied in this paper. The power spectral density is shown relative to the measured values averaged over the reference currents shown in the green dashed box.

Chapter 4

Discussion

4.1 Summary of study themes

4.1.1 Spin current control of a magnetic nanowire

In this work, we explored how N-V magnetometry can be used to detect magnetic dynamics in the presence of spin currents. We fabricated Py/Pt nanowires on a diamond chip substrate and probed the ferromagnetic modes using a single N-V centre. We observed large-amplitude magnetic oscillations driven by a parametric drive, a nonlinear method of excitation possible when a system parameter such as damping is periodically varied at approximately twice the natural frequency [52, 56]. These excitations were only possible in our device thanks to the large spin-orbit torque (SOT) from the Pt layer which enabled strong microwave driving and a bias-induced damping reduction. We detected the magnetic signal using resonant and off-resonance ODMR and compared it with standard ST-FMR measurements [84, 261] to validate our measurements. Finally, we used relaxometry measurements of the N-V's spin to measure the local noise temperature, where we achieved SOT-cooling of the magnetic modes from room temperature to ~ 150 K.

Using metallic permalloy as our magnetic layer allowed us to characterize the FMR of our device via transport measurements. The established technique of ST-FMR [84, 261] enabled determination of the FMR frequency by fitting the frequency-dependent voltage to a Fano peak. We compared the FMR frequencies versus the swept magnetic field to the Kittel model [262] to estimate the coercive fields of the device. When we applied above-threshold SOT antidamping we observed parametric driving at twice the fundamental FMR frequency. We compared ST-FMR measurements of the parametric oscillator to the maximally observed AMR to estimate a precession angle of $55°$.

We used the ST-FMR findings to guide and interpret our measurements with the N-V. We observed that off-resonant, large-angle parametric oscillations affected the ODMR frequency due to a decrease in the average local field at the location of the N-V. The change in average field relative to the overall stray field implied a precession angle of 60°, which corroborated out measurements done in transport. Similar styles of measurements have previously been performed on a Py microdisk by van der Sar [174], though we note that our measurement extended the technique to large-angle dynamics enabled by SOTs.

More interestingly, we also resonantly drove the N-V ODMR using the stray field from the parametrically excited FMR. We observed a decrease in fluorescence when we drove the magnet at exactly twice the ODMR frequency, but only when the natural FMR frequency was equal to or below that of the N-V. Unlike resonant driving, which could only effectively drive the fundamental mode, parametric driving was able to excite higher-order modes, which interacted with the N-V over a large range of tuning fields. The observed fluorescence dip was only visible when we applied bias exceeding the same threshold for parametric driving that we saw in ST-FMR, confirming our interpretation of the excitation mechanism. Exciting the N-V in this manner presented a direct way of using optically detected ferromagnetic resonance (ODFMR) without crosstalk from the drive which was at twice the N-V frequency. Other measurements have accomplished this isolation between pump and probe by exciting FMR far below the probe frequencies [175–179, 187], an affect attributed to multi-magnon scattering that distributes the input energy into the higher-frequency modes [177]. We do not observe ODFMR at sub-resonant drive frequencies in our system, indicating that the reduced geometry of our system may inhibit these multi-magnon decay channels. Our detection of parametric ODFMR, however, shows that this method can continue to provide pump-probe isolation in even in nanomagnetic devices, and has since been observed in other devices [178, 189].

We lastly used spin relaxometry to detect the magnetic noise spectrum from the thermally occupied magnon modes. Similar to other characterizations of magnetic devices via relaxometry [159, 174], we observed a maximum in the detected noise spectrum when the N-V's transition frequency was just above that of the fundamental FMR, namely when the N-V interacted with the highest density of well-coupled magnon modes. Damping and antidamping SOTs gave us efficient control over the magnon occupancy, which resulted in order of magnitude changes in relaxation rate of the N-V sensor. We found that the application of a negative bias (associated with SOT damping) decreased the effective magnon temperature to ~ 150 K; at the time of the paper's publication, this was the largest SOT-mediated decrease in magnon temperature when detected by N-V relaxometry [159] or BLS [193]. Since the publication of this chapter, N-V measurements of MTJ geometries have seen an even greater reduction in the relaxation rate as damping-SOTs are applied [184].

4.1.2 Parametric synchronization of a spin torque oscillator

In this next work, we used N-V magnetometry to map out the parametric synchronization of an STO. By switching our fabrication process to a subtractive approach on diamond we were able to achieve smaller device sizes, which allowed us to spectrally resolve the lowest frequency magnetic modes. Smaller dimensions meant that the spin currents could now enable spin-torque auto-oscillations capable of significantly decreasing the N-V fluorescence even while subjected to continuous repolarization via optical pumping. ODFMR spectra showed the synchronization of the STO to a parametric drive, which we validated by comparing against ST-FMR measurements and magnetic simulations. Lastly, we observed large relaxation rates in excess of 1 μs^{-1} as the device was made to auto-oscillate.

A subtractive device fabrication approach allowed us to build smaller devices than we had achieved in our previous work. We opted for a thinner Py(5 nm)/Pt(5 nm) bilayer stack compared to the 10 nm on 10 nm used previously, which was uniformly evaporated onto the diamond chip. Next, alumina masking followed by an argon ion milling step enabled the definition of the shorter and narrower devices. Subsequent measurements revealed that ion milling drastically reduced the ODMR contrast, which we attributed to a changing surface chemistry altering the N-V charge state populations [263–265]. Exposing the surface to the oxygen of a plasma asher was shown to repair the ODMR contrast to the nominal value without affecting the magnetic properties of the devices.

The smaller device dimensions enabled by our subtractive process meant that antidamping SOTs sharpened the two lowest frequency modes of oscillation, enabling ST-FMR measurements to resolve them when excited either resonantly or parametrically. CW-ODMR measurements by the N-V also detected resolvable spin-wave dynamics, and parametric ODFMR revealed two distinct modes in contrast to the continuum we observed in our previous work. Above a specific threshold, we saw that the N-V fluorescence decreased when the lowest mode was resonant with the N-V, even when the drive frequency was far detuned. We attributed this decrease to incoherent relaxation of the N-V by auto-oscillations of the magnetics. This work thus marks the second demonstration of N-V detection of spin-torque oscillations after Zhang measured an STO consisting of a YIG/Pt bilayer [183], and the first in a metallic device where corroborating transport measurements are possible.

Near the critical bias threshold, we demonstrated parametric control of two resolvable magnon modes which we detect using parametric ODFMR. By monitoring the N-V fluorescence as the bias, field, and drive frequency were swept, we not only observed the interaction with the coherent parametric oscillator, but we also observed features which we attribute to the incoherent noise spectrum of the auto-oscillations when the bias was above threshold. When microwaves were applied just outside the parametric synchronization range, the oscillation frequency of the STO was seen to deflect. Furthermore, we observed extended tails in the spectra which we attribute to beat tones between the STO and the applied drive. Only the lowest-frequency mode was seen to auto-oscillate, yet parametric driving of the second mode reduced the amplitude of the STO. This power-sapping effect disappeared when the bias was increased further above the bias threshold, showcasing the N-V's ability to probe spin-wave coupling in magnetic devices operating near their critical points.

Our observation of the parametric synchronization in the ODMR spectra demonstrated a rich feature set, so we used a macrospin magnetic model to simulate the measurement and help corroborate our interpretations. We modelled the Lindau-Lifshitz-Gilbert (LLG) equations to solve the magnetic trajectory of a single dipole subjected to the fields and spin torques in the experiment. We then mapped that trajectory onto the device dimensions to solve for how the stray field at the N-V location would affect the fluorescence of the emitter. The simulation replicated the same qualitative features we saw in the fluorescence spectrum, namely synchronization of the auto-oscillating mode to a parametric drive and the creation of beat-tones between the STO and drive capable of driving ODMR.

Finally, measuring spin relaxometry while sweeping the applied field and bias allowed us to detect the STO using an all-optical N-V approach. When the STO was resonant with the N-V spin transition, we observed decay rates of order 1 μs^{-1}. These rates are comparable to the optical repolarization rate of the N-V, and are therefore consistent with our observation of STO-induced fluorescence quenching in our continuously excited ODMR measurements.

4.2 Limitations of the studies

Both experimental designs had limitations that complicated analysis. Our ODMR techniques were operated in CW for experimental simplicity, but without well designed reference measurements it was difficult to separate spin mixing from drifts in optical alignment. Multiple sources of spin mixing also complicated our interpretation of the relaxometry measurements in Chap. 3, which made it difficult to estimated the parameters over the high dynamic range of our data. Equally limiting was our choice of sensing architecture, where we used N-Vs embedded in the diamond substrate on which we fabricated our devices, as the stochastic process of finding a suitable device with a well-coupled N-V probe reduced the experimental yields. Importantly, the patterned devices were susceptible to failure mechanisms, which limited our ability to fully characterize their behaviour before their demise.

Our CW-ODMR were susceptible to drifts in optical alignment, and required renormalization of the fluorescence between fast sweeps in post. While this was feasible in Chap. 2 by comparing the many fluorescent points when driving with far off-resonant frequencies, the same was not possible in our Chap. 3 because the onset of spin torque oscillations drove the N-V even when the drive frequency was far detuned. Better measurement designs would also have included a reference pulse during which the device bias was turned off, as variation in the N-V fluorescence from optical drifts would be more easily distinguished from variation caused by the STO coming into resonance with the N-V. Instead, we had to renormalize the fluorescence against the fully-mixed state of the N-V when the microwaves drove the $\nu_\pm$ transitions. As fewer datapoints defined these transitions than the background, systemic noise was introduced between fast sweeps, which could have been avoided with proper reference pulses built into the experiment.

Interpreting the magnon occupancy via the measured relaxation rates in Chap. 2 was difficult because the N-V was always interacting with a bath of unresolved magnon modes. Applying bias not only changed the thermal occupation of the modes, it also affected the linewidths of each mode, the relative frequency detuning from the N-V probe, and the density of interacting states. In order to extract an effective magnon temperature, we needed to place further assumptions on how the N-V interacted with the changing magnon density of states (see Section 2.14).

Our relaxometry measurements in Chap. 3 also had issues between distinguishing real signals from the STO and other sources of spin mixing such as was induced by the proximity to the excited state level anti-crossing [233]. We used an all-optical approach to initialize and read out the spin state after a variable dark time. This process should have resulted in a single-exponential decay in fluorescence as only the transition between $m_s = 0$ and $+1$ was strongly affected by the STO noise. Our data did not always fit well to such a model because off-axis fields near the excited state level anti-crossing mixed the $m_s = 0$ and -1 states during optical initialization [192]. Furthermore, when the STO began to auto-oscillate in resonance with the N-V, it mixed the spins faster than the optical pumping could repolarize them. Calibration of π-pulses to enable initialization into any of the spin states would have mitigated many of these discrepancies between the data and our fitting procedure, though automation of the process would be required as the frequency of the π-pulse would need to be recalibrated for each value of field and bias.

Finally, we note that while our sample-on-a-diamond-chip approach to detecting spin-waves with N-Vs required less overhead than other methods of interfacing the spin sensor such as mechanically ground nanodiamonds, it introduced its own set of challenges. Magnetic circuits were fabricated on diamond rather than typical industrial substrates such as silicon, as such most process steps needed to be tested for use with diamond. Electron beam lithography in particular was limited in resolution and accuracy due to charging effects of the insulating diamond, affecting the achievable feature sizes in our first study. Furthermore, relatively few devices (circa 40) with wirebondable pads could be produced on each 4.5 mm $\times$ 4.5 mm diamond chip, and viable devices needed to have an N-V within tens of nanometers of the device and with the correct crystallographic orientation. The low fabrication yield made the eventual death via of working devices more painful; we had several devices slowly or rapidly degrade before causing an open circuit, which we attributed to electromigration in the nanowire from Chap. 2 and electrostatic shock killing the device in Chap. 3.

4.3 Directions for future research

The methods demonstrated in this thesis can be extended to detecting spin waves in more complicated magnonic circuits. Parametric ODFMR offers an avenue for controlling and magnetic dynamics while isolating the drive field from the measurement. We have also seen evidence of coupling between spin-wave modes at critical antidamping, where further research is needed to understand the interplay. ODFMR could also be used as a future method for efficient quantum state control in N-Vs. Most promisingly, STO detection schemes should be extended to scanning probe systems to uncover the behaviour of nanoscale arrays and other interesting geometries.

By isolating the excitation frequency of the pump from the N-V probe frequency, parametric ODFMR can help isolate the spin-wave dynamics we wish to detect. Similar pump-probe separation has been accomplished in large sheets of magnetic materials by pumping the fundamental FMR, which in turn excites higher-order modes by three- or four-wave mixing [159, 177], but we were unable to detect this mechanism in any of our devices. This shows that parametric ODFMR offers a new tool for crosstalk-free spin-wave measurement that extends to small scales where the continuum of spin-wave modes becomes discretized. Furthermore, while FMR-pumped ODMR drives the N-V through the incoherently scattered spin waves, parametric pumping intrinsically preserves the phase between the magnetic response and the drive.

In both of our works probing devices of different sizes, we observed evidence for magnon-magnon interactions via parametric ODFMR. Despite this, the nature of these interactions near the critical antidamping point remains poorly understood. In Chap. 3, we detect that driving a second resolved magnetic mode sapped the energy from the mode undergoing auto-oscillations, but only very near the threshold bias. Future work should map this interplay in greater detail, for instance by measuring the phase space of power and detuning needed to synchronize the STO as a function of bias current, similarly to what has been done in nanocontact systems measured in transport [56] or has been studied using N-Vs and resonant driving in YIG/Pt STOs [183].

The ease with which large-angle oscillations can drive N-V dynamics shows the potential for ODFMR as an energy efficient and miniature method for quantum control. We demonstrated that STOs can achieve large relaxation rates of the N-V, but what remains to be seen is whether phase-locking an STO to a coherent input drive can also manipulate the N-V spin. Pulsing of the coherent drive, the control bias, or both simultaneously needs to be tested to verify if they can control coherent Rabi oscillations of the spin state. This would enable new modalities for devices to offer for magnonic control of quantum interfaces like the N-V, in complement with recently demonstrated techniques using adiabatic passage mediated by a ferromagnetic vortex to implement $\pi/2$ control [266].

Most importantly, the high spatial resolution that can be achieved using scanning probe implementations of N-V magnetometry offers the greatest opportunities to extend the work performed in this thesis. To show practical uses, magnonic devices are scaling down in size while they simultaneously increase in complexity, requiring improved sensing to test whether they operate as expected. Spatial information would improve our own understanding of our nanowire systems, as measuring the spatial correlations to parametric ODFMR would uncover the spatial mode profiles for each of the synchronized modes by adapting magnetic texture reconstruction techniques [127] to maps of the parametric ODFMR Rabi frequency. Furthermore, while the self-synchronization of STO arrays [39] has been verified using spectrometer readout of the electric current and by focused-BLS detection of magnetic oscillations, the former technique is non-locally averaged over the entire device while the resolution of the latter exceeded the feature sizes of the array. N-V scanning probes measuring in either relaxometry [169] or parametric ODFMR detection modes should be operated over such devices in order to resolve the activity of the individual STOs within the array, such as the case where not all oscillators are mutually synchronized. To that end, properly designed pulse sequences can result in measurements insensitive to drifts in optical alignment, and Bayesian inference can drastically speed up the measurement when the relaxation rate is not known in advance [149].

Chapter 5

Conclusion

The work in this thesis set out to deepen our understanding and control of spin-current-based magnetic devices through the development of new quantum sensing protocols. We developed nanofabrication techniques to build metallic magnet bilayers on diamond, where the magnetic dynamics were strongly affected by SOTs injected from a heavy metal layer. We used ODMR from proximal N-Vs to map the magnetic resonances, which we then validated against established ST-FMR techniques. We developed parametric ODFMR to measure nonlinear control of magnetic devices without being affected by crosstalk from a degenerate pump. Using spin relaxometry, we detected order-of-magnitude changes in the magnon thermal occupation by applying damping and antidamping SOTs. Extending these methods to smaller devices, we detected strong relaxation-induced fluorescence quenching from our N-V probe when a proximal STO began to auto-oscillate. By sweeping a parametric pump, we mapped the synchronization space of the STO by observing how the coherent and incoherent drives affect the N-V fluorescence, and we validated our understanding against simulations.

These findings improve our understanding of quantum sensing protocols in the presence of strongly-driven magnetic devices, which is crucial to mapping the technique to more complicated systems. By understanding the interaction between the N-V probe and magnetic modes of a simple magnetic nanowire, we can take the next steps towards measuring self-interacting systems like STO arrays used for neuromorphic computing. Furthermore, extending our work to develop a magnetic parametric amplifier may enable new and efficient ways of interfacing spin waves with spin qubits.

Bibliography

[1] D C Ralph and M D Stiles. Spin transfer torques. *Journal of Magnetism and Magnetic Materials*, 320:1190–1216, 2008. 2, 3

[2] Sabpreet Bhatti, Rachid Sbiaa, Atsufumi Hirohata, Hideo Ohno, Shunsuke Fukami, and S. N. Piramanayagam. Spintronics based random access memory: a review. *Materials Today*, 20:530–548, 11 2017. 2

[3] S. Ikeda, J. Hayakawa, Y. Ashizawa, Y. M. Lee, K. Miura, H. Hasegawa, M. Tsunoda, F. Matsukura, and H. Ohno. Tunnel magnetoresistance of 604diffusion in cofebmgocofeb pseudo-spin-valves annealed at high temperature. *Applied Physics Letters*, 93:082508, 8 2008. 2, 3

[4] Minh Hai Nguyen, D. C. Ralph, and R. A. Buhrman. Spin torque study of the spin hall conductivity and spin diffusion length in platinum thin films with varying resistivity. *Physical Review Letters*, 116:126601, 3 2016. 2

[5] A. V. Chumak, V. I. Vasyuchka, A. A. Serga, and B. Hillebrands. Magnon spintronics. *Nature Physics 2014 11:6*, 11:453–461, 6 2015. 2, 88

[6] Philipp Pirro, Vitaliy I. Vasyuchka, Alexander A. Serga, and Burkard Hillebrands. Advances in coherent magnonics. *Nature Reviews Materials 2021 6:12*, 6:1114–1135, 7 2021. 2, 7

[7] William Thomson. Xix. on the electro-dynamic qualities of metals:—effects of magnetization on the electric conductivity of nickel and of iron. *Proceedings of the Royal Society of London*, 8:546–550, 12 1857. 2

[8] T. R. McGuire and R. I. Potter. Anisotropic magnetoresistance in ferromagnetic 3d alloys. *IEEE Transactions on Magnetics*, 11:1018–1038, 1975. 2

[9] Karel Výborný, Jan Kučera, Jairo Sinova, A. W. Rushforth, B. L. Gallagher, and T. Jungwirth. Microscopic mechanism of the noncrystalline anisotropic magnetoresis-

tance in (ga,mn)as. *Physical Review B - Condensed Matter and Materials Physics*, 80:165204, 10 2009. 2

[10] Chong Jun Zhao, Lei Ding, Jia Shun Huangfu, Jing Yan Zhang, and Guang Hua Yu. Research progress in anisotropic magnetoresistance. *Rare Metals*, 32:213–224, 6 2013. 2

[11] M. N. Baibich, J. M. Broto, A. Fert, F. Nguyen Van Dau, F. Petroff, P. Eitenne, G. Creuzet, A. Friederich, and J. Chazelas. Giant magnetoresistance of (001)fe/(001)cr magnetic superlattices. *Physical Review Letters*, 61:2472–2475, 11 1988. 3

[12] G. Binasch, P. Grünberg, F. Saurenbach, and W. Zinn. Enhanced magnetoresistance in layered magnetic structures with antiferromagnetic interlayer exchange. *Physical Review B*, 39:4828, 3 1989. 3

[13] T. Miyazaki and N. Tezuka. Giant magnetic tunneling effect in fe/al2o3/fe junction. *Journal of Magnetism and Magnetic Materials*, 139:L231–L234, 1 1995. 3

[14] J. S. Moodera, Lisa R. Kinder, Terrilyn M. Wong, and R. Meservey. Large magnetoresistance at room temperature in ferromagnetic thin film tunnel junctions. *Physical Review Letters*, 74:3273, 4 1995. 3

[15] A. Gupta, T. R. McGuire, P. R. Duncombe, M. Rupp, J. Z. Sun, W. J. Gallagher, and Gang Xiao. Growth and giant magnetoresistance properties of la-deficient laxmno3 (0.67x1) films. *Applied Physics Letters*, 67:3494, 6 1995. 3

[16] Lijun Zhu, Daniel C. Ralph, and Robert A. Buhrman. Maximizing spin-orbit torque generated by the spin hall effect of pt. *Applied Physics Reviews*, 8:031308, 8 2021. 4

[17] Stuart S.P. Parkin, Masamitsu Hayashi, and Luc Thomas. Magnetic domain-wall racetrack memory. *Science*, 320:190–194, 4 2008. 4, 5

[18] J. C. Slonczewski. Current-driven excitation of magnetic multilayers. *Journal of Magnetism and Magnetic Materials*, 159:L1–L7, 6 1996. 5

[19] L. Berger. Emission of spin waves by a magnetic multilayer traversed by a current. *Physical Review B*, 54:9353, 10 1996. 5

[20] E. B. Myers, D. C. Ralph, J. A. Katine, R. N. Louie, and R. A. Buhrman. Current-induced switching of domains in magnetic multilayer devices. *Science*, 285:867–870, 8 1999. 5

[21] Andrew D. Kent and Daniel C. Worledge. A new spin on magnetic memories. *Nature Nanotechnology 2015 10:3*, 10:187–191, 3 2015. 5

[22] Masamitsu Hayashi, Luc Thomas, Charles Rettner, Rai Moriya, Yaroslaw B. Bazaliy, and Stuart S.P. Parkin. Current driven domain wall velocities exceeding the spin angular momentum transfer rate in permalloy nanowires. *Physical Review Letters*, 98:037204, 1 2007. 5

[23] Pietro Gambardella and Ioan Mihai Miron. Current-induced spin-orbit torques. *Philosophical Transactions of the Royal Society A: Mathematical, Physical and Engineering Sciences*, 369:3175–3197, 8 2011. 5

[24] Rajagopalan Ramaswamy, Jong Min Lee, Kaiming Cai, and Hyunsoo Yang. Recent advances in spin-orbit torques: Moving towards device applications. *Applied Physics Reviews*, 5:031107, 9 2018. 5

[25] Qiming Shao, Peng Li, Luqiao Liu, Hyunsoo Yang, Shunsuke Fukami, Armin Razavi, Hao Wu, Kang Wang, Frank Freimuth, Yuriy Mokrousov, Mark D. Stiles, Satoru Emori, Axel Hoffmann, Johan Akerman, Kaushik Roy, Jian Ping Wang, See Hun Yang, Kevin Garello, and Wei Zhang. Roadmap of spin-orbit torques. *IEEE Transactions on Magnetics*, 57, 7 2021. 5

[26] Luqiao Liu, Takahiro Moriyama, D. C. Ralph, and R. A. Buhrman. Spin-torque ferromagnetic resonance induced by the spin hall effect. *Physical Review Letters*, 106:036601, 1 2011. 6, 10, 88

[27] P. Laczkowski, Y. Fu, H. Yang, J. C. Rojas-Sánchez, P. Noel, V. T. Pham, G. Zahnd, C. Deranlot, S. Collin, C. Bouard, P. Warin, V. Maurel, M. Chshiev, A. Marty, J. P.

Attané, A. Fert, H. Jaffrès, L. Vila, and J. M. George. Large enhancement of the spin hall effect in au by side-jump scattering on ta impurities. *Physical Review B*, 96:140405, 10 2017. 6

[28] Sachin Pathak, Chanyoung Youm, and Jongill Hong. Impact of spin-orbit torque on spin-transfer torque switching in magnetic tunnel junctions. *Scientific Reports 2020 10:1*, 10:1–8, 2 2020. 6

[29] J. Byun, D. H. Kang, and M. Shin. Switching performance comparison between conventional sot and stt-sot write schemes with effect of shape deformation. *AIP Advances*, 11:015035, 1 2021. 6

[30] Ashish Sura and Vikas Nehra. Performance comparison of single level stt and sot mram cells for cache applications. *2021 25th International Symposium on VLSI Design and Test, VDAT 2021*, 9 2021. 6

[31] Viola Krizakova, Manu Perumkunnil, Sébastien Couet, Pietro Gambardella, and Kevin Garello. Spin-orbit torque switching of magnetic tunnel junctions for memory applications. *Journal of Magnetism and Magnetic Materials*, 562:169692, 11 2022. 6

[32] S. I. Kiselev, J. C. Sankey, I. N. Krivorotov, N. C. Emley, R. J. Schoelkopf, R. A. Buhrman, and D. C. Ralph. Microwave oscillations of a nanomagnet driven by a spin-polarized current. *Nature 2003 425:6956*, 425:380–383, 9 2003. 6, 10, 88, 105

[33] Oleksandr Prokopenko, Elena Bankowski, Thomas Meitzler, Vasil Tiberkevich, and Andrei Slavin. Spin-torque nano-oscillator as a microwave signal source. *IEEE Magnetics Letters*, 2, 2011. 6

[34] Zahra Haghshenasfard, Hoa T. Nguyen, and Michael G. Cottam. Suhl instabilities for spin waves in ferromagnetic nanostripes and ultrathin films. *Journal of Magnetism and Magnetic Materials*, 426:380–389, 3 2017. 6, 20, 89

[35] Andrew Smith, Kemal Sobotkiewich, Amanatullah Khan, Eric A. Montoya, Liu Yang, Zheng Duan, Tobias Schneider, Kilian Lenz, Jürgen Lindner, Kyongmo An, Xiaoqin Li,

and Ilya N. Krivorotov. Dimensional crossover in spin hall oscillators. *Physical Review B*, 102:054422, 8 2020. 6, 85

[36] Joo Von Kim, Vasil Tiberkevich, and Andrei N. Slavin. Generation linewidth of an auto-oscillator with a nonlinear frequency shift: Spin-torque nano-oscillator. *Physical Review Letters*, 100:017207, 1 2008. 6

[37] S. Sani, J. Persson, S. M. Mohseni, Ye Pogoryelov, P. K. Muduli, A. Eklund, G. Malm, M. Käll, A. Dmitriev, and J. Akerman. Mutually synchronized bottom-up multi-nanocontact spin–torque oscillators. *Nature Communications 2013 4:1*, 4:1–7, 11 2013. 6

[38] Sumito Tsunegi, Tomohiro Taniguchi, Romain Lebrun, Kay Yakushiji, Vincent Cros, Julie Grollier, Akio Fukushima, Shinji Yuasa, and Hitoshi Kubota. Scaling up electrically synchronized spin torque oscillator networks. *Scientific Reports 2018 8:1*, 8:1–7, 9 2018. 6

[39] Mohammad Zahedinejad, Ahmad A. Awad, Shreyas Muralidhar, Roman Khymyn, Himanshu Fulara, Hamid Mazraati, Mykola Dvornik, and Johan Åkerman. Two-dimensional mutually synchronized spin hall nano-oscillator arrays for neuromorphic computing. *Nature Nanotechnology 2019 15:1*, 15:47–52, 12 2019. 6, 8, 9, 11, 102, 114

[40] M. A. Castro, D. Mancilla-Almonacid, B. Dieny, S. Allende, L. D. Buda-Prejbeanu, and U. Ebels. Mutual synchronization of spin-torque oscillators within a ring array. *Scientific Reports 2022 12:1*, 12:1–8, 7 2022. 6

[41] S. Urazhdin, V. E. Demidov, H. Ulrichs, T. Kendziorczyk, T. Kuhn, J. Leuthold, G. Wilde, and S. O. Demokritov. Nanomagnonic devices based on the spin-transfer torque. *Nature Nanotechnology 2014 9:7*, 9:509–513, 5 2014. 7

[42] Vladislav E. Demidov, Sergei Urazhdin, Ronghua Liu, Boris Divinskiy, Andrey Telegin, and Sergej O. Demokritov. Excitation of coherent propagating spin waves by pure spin currents. *Nature Communications 2016 7:1*, 7:1–6, 1 2016. 7

[43] M. Evelt, L. Soumah, A. B. Rinkevich, S. O. Demokritov, A. Anane, V. Cros, Jamal Ben Youssef, G. De Loubens, O. Klein, P. Bortolotti, and V. E. Demidov. Emission of coherent propagating magnons by insulator-based spin-orbit-torque oscillators. *Physical Review Applied*, 10:041002, 10 2018. 7

[44] Boris Divinskiy, Vladislav E Demidov, Sergei Urazhdin, Ryan Freeman, Anatoly B Rinkevich, Sergej O Demokritov B Divinskiy, V E Demidov, S O Demokritov, S Urazhdin, R Freeman, and A B Rinkevich. Excitation and amplification of spin waves by spin–orbit torque. *Advanced Materials*, 30:1802837, 8 2018. 7

[45] N. Locatelli, V. Cros, and J. Grollier. Spin-torque building blocks. *Nature Materials 2014 13:1*, 13:11–20, 12 2014. 7

[46] M. Evelt, V. E. Demidov, V. Bessonov, S. O. Demokritov, J. L. Prieto, M. Muñoz, J. Ben Youssef, V. V. Naletov, G. De Loubens, O. Klein, M. Collet, K. Garcia-Hernandez, P. Bortolotti, V. Cros, and A. Anane. High-efficiency control of spin-wave propagation in ultra-thin yttrium iron garnet by the spin-orbit torque. *Applied Physics Letters*, 108:172406, 4 2016. 7

[47] Hugo Merbouche, Boris Divinskiy, Diane Gouéré, Romain Lebrun, Aya El-Kanj, Vincent Cros, Paolo Bortolotti, Abdelmadjid Anane, Sergej O. Demokritov, and Vladislav E. Demidov. True amplification of spin waves in magnonic nano-waveguides. 3 2023. 7

[48] T. Brächer, P. Pirro, and B. Hillebrands. Parallel pumping for magnon spintronics: Amplification and manipulation of magnon spin currents on the micron-scale. *Phys. Rep.*, 699:1–34, 2017. 7, 75, 76

[49] Roman Verba, Mario Carpentieri, Giovanni Finocchio, Vasil Tiberkevich, and Andrei Slavin. Excitation of propagating spin waves in ferromagnetic nanowires by microwave voltage-controlled magnetic anisotropy. *Scientific Reports 2016 6:1*, 6:1–9, 4 2016. 7

[50] Yu Jin Chen, Han Kyu Lee, Roman Verba, Jordan A. Katine, Igor Barsukov, Vasil Tiberkevich, John Q. Xiao, Andrei N. Slavin, and Ilya N. Krivorotov. Parametric

resonance of magnetization excited by electric field. *Nano Letters*, 17:572–577, 1 2017. 7

[51] A. V. Sadovnikov, A. A. Grachev, S. E. Sheshukova, Yu P. Sharaevskii, A. A. Serdobintsev, D. M. Mitin, and S. A. Nikitov. Magnon straintronics: Reconfigurable spin-wave routing in strain-controlled bilateral magnetic stripes. *Physical Review Letters*, 120:257203, 6 2018. 7

[52] Frederic R. Morgenthaler. Survey of ferromagnetic resonance in small ferrimagnetic ellipsoids. *Journal of Applied Physics*, 31:S95, 8 2009. 7, 107

[53] T. Brächer, P. Pirro, B. Obry, B. Leven, A. A. Serga, and B. Hillebrands. Mode selective parametric excitation of spin waves in a ni81fe19 microstripe. *Applied Physics Letters*, 99:162501, 10 2011. 7, 11

[54] Morteza Mohseni, Martin Kewenig, Roman Verba, Qi Wang, Michael Schneider, Björn Heinz, Felix Kohl, Carsten Dubs, Bert Lägel, Alexander A. Serga, Burkard Hillebrands, Andrii V. Chumak, and Philipp Pirro. Parametric generation of propagating spin waves in ultrathin yttrium iron garnet waveguides. *physica status solidi (RRL) – Rapid Research Letters*, 14:2000011, 4 2020. 7

[55] V. E. Demidov, H. Ulrichs, S. V. Gurevich, S. O. Demokritov, V. S. Tiberkevich, A. N. Slavin, A. Zholud, and S. Urazhdin. Synchronization of spin hall nano-oscillators to external microwave signals. *Nature Communications 2014 5:1*, 5:1–6, 1 2014. 7, 11

[56] Sergei Urazhdin, Vasil Tiberkevich, and Andrei Slavin. Parametric excitation of a magnetic nanocontact by a microwave field. *Physical Review Letters*, 105:237204, 12 2010. 7, 107, 114

[57] P. Dürrenfeld, E. Iacocca, J. Åkerman, and P. K. Muduli. Modulation-mediated unlocking of a parametrically phase-locked spin torque oscillator. *Applied Physics Letters*, 105:252404, 12 2014. 7

[58] Anjan Barman, Gianluca Gubbiotti, S. Ladak, A. O. Adeyeye, M. Krawczyk, J. Grafe, C. Adelmann, S. Cotofana, A. Naeemi, V. I. Vasyuchka, B. Hillebrands, S. A. Niki-

tov, H. Yu, D. Grundler, A. V. Sadovnikov, A. A. Grachev, S. E. Sheshukova, J. Y. Duquesne, M. Marangolo, G. Csaba, W. Porod, V. E. Demidov, S. Urazhdin, S. O. Demokritov, E. Albisetti, D. Petti, R. Bertacco, H. Schultheiss, V. V. Kruglyak, V. D. Poimanov, S. Sahoo, J. Sinha, H. Yang, M. Münzenberg, T. Moriyama, S. Mizukami, P. Landeros, R. A. Gallardo, G. Carlotti, J. V. Kim, R. L. Stamps, R. E. Camley, B. Rana, Y. Otani, W. Yu, T. Yu, G. E.W. Bauer, C. Back, G. S. Uhrig, O. V. Dobrovolskiy, B. Budinska, H. Qin, S. Van Dijken, A. V. Chumak, A. Khitun, D. E. Nikonov, I. A. Young, B. W. Zingsem, and M. Winklhofer. The 2021 magnonics roadmap. *Journal of Physics: Condensed Matter*, 33:413001, 8 2021. 7

[59] Q. Wang, M. Kewenig, M. Schneider, R. Verba, F. Kohl, B. Heinz, M. Geilen, M. Mohseni, B. Lägel, F. Ciubotaru, C. Adelmann, C. Dubs, S. D. Cotofana, O. V. Dobrovolskiy, T. Brächer, P. Pirro, and A. V. Chumak. A magnonic directional coupler for integrated magnonic half-adders. *Nature Electronics 2020 3:12*, 3:765–774, 10 2020. 8, 9, 88

[60] Yutaka Tabuchi, Seiichiro Ishino, Atsushi Noguchi, Toyofumi Ishikawa, Rekishu Yamazaki, Koji Usami, and Yasunobu Nakamura. Coherent coupling between a ferromagnetic magnon and a superconducting qubit. *Science*, 349:405–408, 7 2015. 8, 9

[61] Marc Vogel, Andrii V. Chumak, Erik H. Waller, Thomas Langner, Vitaliy I. Vasyuchka, Burkard Hillebrands, and Georg Von Freymann. Optically reconfigurable magnetic materials. *Nature Physics 2014 11:6*, 11:487–491, 5 2015. 7

[62] A. V. Chumak, P. Pirro, A. A. Serga, M. P. Kostylev, R. L. Stamps, H. Schultheiss, K. Vogt, S. J. Hermsdoerfer, B. Laegel, P. A. Beck, and B. Hillebrands. Spin-wave propagation in a microstructured magnonic crystal. *Applied Physics Letters*, 95:262508, 12 2009. 7

[63] S. A. Nikitov, Ph Tailhades, and C. S. Tsai. Spin waves in periodic magnetic structures—magnonic crystals. *Journal of Magnetism and Magnetic Materials*, 236:320–330, 11 2001. 7

[64] Björn Obry, Philipp Pirro, Thomas Brächer, Andrii V. Chumak, Julia Osten, Florin Ciubotaru, Alexander A. Serga, Jürgen Fassbender, and Burkard Hillebrands. A micro-structured ion-implanted magnonic crystal. *Applied Physics Letters*, 102:202403, 5 2013. 7

[65] Alexey B. Ustinov, Andrei V. Drozdovskii, Andrey A. Nikitin, Alexander A. Semenov, Dmytro A. Bozhko, Alexander A. Serga, Burkard Hillebrands, Erkki Lähderanta, and Boris A. Kalinikos. Dynamic electromagnonic crystal based on artificial multiferroic heterostructure. *Communications Physics 2019 2:1*, 2:1–7, 11 2019. 7

[66] A. V. Chumak, A. A. Serga, and B. Hillebrands. Magnonic crystals for data processing. *Journal of Physics D: Applied Physics*, 50:244001, 5 2017. 7

[67] Andrey A. Nikitin, Alexey B. Ustinov, Alexander A. Semenov, Andrii V. Chumak, Alexander A. Serga, Vitaliy I. Vasyuchka, Erkki Lähderanta, Boris A. Kalinikos, and Burkard Hillebrands. A spin-wave logic gate based on a width-modulated dynamic magnonic crystal. *Applied Physics Letters*, 106:102405, 3 2015. 9

[68] Taichi Goto, Takuya Yoshimoto, Bungo Iwamoto, Kei Shimada, Caroline A. Ross, Koji Sekiguchi, Alexander B. Granovsky, Yuichi Nakamura, Hironaga Uchida, and Mitsuteru Inoue. Three port logic gate using forward volume spin wave interference in a thin yttrium iron garnet film. *Scientific Reports 2019 9:1*, 9:1–11, 11 2019. 9

[69] Bivas Rana and Yoshichika Otani. Voltage-controlled reconfigurable spin-wave nanochannels and logic devices. *Physical Review Applied*, 9:014033, 1 2018. 9

[70] Abdulqader Mahmoud, Florin Ciubotaru, Frederic Vanderveken, Andrii V. Chumak, Said Hamdioui, Christoph Adelmann, and Sorin Cotofana. Introduction to spin wave computing. *Journal of Applied Physics*, 128:161101, 10 2020. 9

[71] J. Grollier, D. Querlioz, K. Y. Camsari, K. Everschor-Sitte, S. Fukami, and M. D. Stiles. Neuromorphic spintronics. *Nature Electronics 2020 3:7*, 3:360–370, 3 2020. 9, 88

[72] Seungmo Yang, Jeonghun Shin, Taeyoon Kim, Kyoung Woong Moon, Jaewook Kim, Gabriel Jang, Da Seul Hyeon, Jungyup Yang, Chanyong Hwang, Yeon Joo Jeong, and Jin Pyo Hong. Integrated neuromorphic computing networks by artificial spin synapses and spin neurons. *NPG Asia Materials 2021 13:1*, 13:1–10, 1 2021. 9, 88

[73] Catherine D. Schuman, Shruti R. Kulkarni, Maryam Parsa, J. Parker Mitchell, Prasanna Date, and Bill Kay. Opportunities for neuromorphic computing algorithms and applications. *Nature Computational Science 2022 2:1*, 2:10–19, 1 2022. 9, 88

[74] Miguel Romera, Philippe Talatchian, Sumito Tsunegi, Flavio Abreu Araujo, Vincent Cros, Paolo Bortolotti, Juan Trastoy, Kay Yakushiji, Akio Fukushima, Hitoshi Kubota, Shinji Yuasa, Maxence Ernoult, Damir Vodenicarevic, Tifenn Hirtzlin, Nicolas Locatelli, Damien Querlioz, and Julie Grollier. Vowel recognition with four coupled spin-torque nano-oscillators. *Nature 2018 563:7730*, 563:230–234, 10 2018. 9, 88

[75] Xiaobin Wang, Yiran Chen, Hai Xi, Hai Li, and Dimitar Dimitrov. Spintronic memristor through spin-thorque-induced magnetization motion. *IEEE Electron Device Letters*, 30:294–297, 2009. 9

[76] Mrigank Sharad, Charles Augustine, Georgios Panagopoulos, and Kaushik Roy. Spin-based neuron model with domain-wall magnets as synapse. *IEEE Transactions on Nanotechnology*, 11:843–853, 2012. 9

[77] A. Yamaguchi, T. Ono, S. Nasu, K. Miyake, K. Mibu, and T. Shinjo. Real-space observation of current-driven domain wall motion in submicron magnetic wires. *Physical Review Letters*, 92:077205, 2 2004. 9

[78] Steven Lequeux, Joao Sampaio, Vincent Cros, Kay Yakushiji, Akio Fukushima, Rie Matsumoto, Hitoshi Kubota, Shinji Yuasa, and Julie Grollier. A magnetic synapse: multilevel spin-torque memristor with perpendicular anisotropy. *Scientific Reports 2016 6:1*, 6:1–7, 8 2016. 9, 88

[79] Tatsuo Shibata, Tetsuhito Shinohara, Takuya Ashida, Minoru Ohta, Kuniyasu Ito, Shogo Yamada, Yukio Terasaki, and Tomoyuki Sasaki. Linear and symmetric conduc-

tance response of magnetic domain wall type spin-memristor for analog neuromorphic computing. *Applied Physics Express*, 13:043004, 3 2020. 9, 88

[80] Saima A. Siddiqui, Sumit Dutta, Astera Tang, Luqiao Liu, Caroline A. Ross, and Marc A. Baldo. Magnetic domain wall based synaptic and activation function generator for neuromorphic accelerators. *Nano Letters*, 20:1033–1040, 2 2020. 9, 88

[81] H. Y. Yuan, Yunshan Cao, Akashdeep Kamra, Rembert A. Duine, and Peng Yan. Quantum magnonics: When magnon spintronics meets quantum information science. *Physics Reports*, 965:1–74, 6 2022. 9

[82] Dany Lachance-Quirion, Samuel Piotr Wolski, Yutaka Tabuchi, Shingo Kono, Koji Usami, and Yasunobu Nakamura. Entanglement-based single-shot detection of a single magnon with a superconducting qubit. *Science*, 367:425–428, 1 2020. 9

[83] Alexy D. Karenowska, A. V. Chumak, A. A. Serga, and Burkard Hillebrands. Magnon spintronics. *Handbook of Spintronics*, pages 1–38, 2015. 10

[84] J. C. Sankey, P. M. Braganca, A. G.F. Garcia, I. N. Krivorotov, R. A. Buhrman, and D. C. Ralph. Spin-transfer-driven ferromagnetic resonance of individual nanomagnets. *Physical Review Letters*, 96:227601, 6 2006. 10, 24, 88, 91, 107

[85] Zheng Duan, Andrew Smith, Liu Yang, Brian Youngblood, Jürgen Lindner, Vladislav E. Demidov, Sergej O. Demokritov, and Ilya N. Krivorotov. Nanowire spin torque oscillator driven by spin orbit torques. *Nature Communications 2014 5:1*, 5:1–7, 12 2014. 10, 88

[86] S. I. Kiselev, J. C. Sankey, I. N. Krivorotov, N. C. Emley, A. G.F. Garcia, R. A. Buhrman, and D. C. Ralph. Spin-transfer excitations of permalloy nanopillars for large applied currents. *Physical Review B*, 72:064430, 8 2005. 10, 88

[87] T. Schneider, A. A. Serga, T. Neumann, B. Hillebrands, and M. P. Kostylev. Phase reciprocity of spin-wave excitation by a microstrip antenna. *Physical Review B - Condensed Matter and Materials Physics*, 77:214411, 6 2008. 10

[88] Vladislav E. Demidov, Mikhail P. Kostylev, Karsten Rott, Patryk Krzysteczko, Guenter Reiss, and Sergej O. Demokritov. Excitation of microwaveguide modes by a stripe antenna. *Applied Physics Letters*, 95:112509, 9 2009. 10

[89] H. Schultheiss, J. E. Pearson, S. D. Bader, and A. Hoffmann. Thermoelectric detection of spin waves. *Physical Review Letters*, 109:237204, 12 2012. 10

[90] Haiming Yu, G. Duerr, R. Huber, M. Bahr, T. Schwarze, F. Brandl, and D. Grundler. Omnidirectional spin-wave nanograting coupler. *Nature Communications 2013 4:1*, 4:1–9, 11 2013. 10

[91] Y. V. Khivintsev, Y. A. Filimonov, and S. A. Nikitov. Spin wave excitation in yttrium iron garnet films with micron-sized antennas. *Applied Physics Letters*, 106:052407, 2 2015. 10

[92] H. S. Körner, J. Stigloher, and C. H. Back. Excitation and tailoring of diffractive spin-wave beams in nife using nonuniform microwave antennas. *Physical Review B*, 96:100401, 9 2017. 10

[93] Marek Vaňatka, Krzysztof Szulc, Ondřej Wojewoda, Carsten Dubs, Andrii V. Chumak, Maciej Krawczyk, Oleksandr V. Dobrovolskiy, Jarosław W. Kłos, and Michal Urbánek. Spin-wave dispersion measurement by variable-gap propagating spin-wave spectroscopy. *Physical Review Applied*, 16:054033, 11 2021. 10

[94] Giacomo Talmelli, Thibaut Devolder, Nick Träger, Johannes Förster, Sebastian Wintz, Markus Weigand, Hermann Stoll, Marc Heyns, Gisela Schütz, Iuliana P. Radu, Joachim Gräfe, Florin Ciubotaru, and Christoph Adelmann. Reconfigurable submicrometer spin-wave majority gate with electrical transducers. *Science Advances*, 6:4042–4060, 12 2020. 10

[95] E. Saitoh, M. Ueda, H. Miyajima, and G. Tatara. Conversion of spin current into charge current at room temperature: Inverse spin-hall effect. *Applied Physics Letters*, 88:182509, 5 2006. 10

[96] O. Mosendz, V. Vlaminck, J. E. Pearson, F. Y. Fradin, G. E.W. Bauer, S. D. Bader, and A. Hoffmann. Detection and quantification of inverse spin hall effect from spin pumping in permalloy/normal metal bilayers. *Physical Review B*, 82:214403, 12 2010. 10

[97] K. Ando, S. Takahashi, J. Ieda, Y. Kajiwara, H. Nakayama, T. Yoshino, K. Harii, Y. Fujikawa, M. Matsuo, S. Maekawa, and E. Saitoh. Inverse spin-hall effect induced by spin pumping in metallic system. *Journal of Applied Physics*, 109:103913, 5 2011. 10

[98] O. D'Allivy Kelly, A. Anane, R. Bernard, J. Ben Youssef, C. Hahn, A. H. Molpeceres, C. Carrétéro, E. Jacquet, C. Deranlot, P. Bortolotti, R. Lebourgeois, J. C. Mage, G. De Loubens, O. Klein, V. Cros, and A. Fert. Inverse spin hall effect in nanometer-thick yttrium iron garnet/pt system. *Applied Physics Letters*, 103:082408, 8 2013. 10

[99] B. F. Miao, S. Y. Huang, D. Qu, and C. L. Chien. Inverse spin hall effect in a ferromagnetic metal. *Physical Review Letters*, 111:066602, 8 2013. 10

[100] V. V. Kruglyak, P. S. Keatley, A. Neudert, R. J. Hicken, J. R. Childress, and J. A. Katine. Imaging collective magnonic modes in 2d arrays of magnetic nanoelements. *Physical Review Letters*, 104:027201, 1 2010. 10, 23, 88

[101] Y. Au, T. Davison, E. Ahmad, P. S. Keatley, R. J. Hicken, and V. V. Kruglyak. Excitation of propagating spin waves with global uniform microwave fields. *Applied Physics Letters*, 98:122506, 3 2011. 10, 88

[102] H. G. Bauer, J. Y. Chauleau, G. Woltersdorf, and C. H. Back. Coupling of spinwave modes in wire structures. *Applied Physics Letters*, 104:102404, 3 2014. 10, 88

[103] S. O. Demokritov, B. Hillebrands, and A. N. Slavin. Brillouin light scattering studies of confined spin waves: linear and nonlinear confinement. *Physics Reports*, 348:441–489, 7 2001. 11, 88

[104] Sergej O. Demokritov and Vladislav E. Demidov. Micro-brillouin light scattering spectroscopy of magnetic nanostructures. *IEEE Transactions on Magnetics*, 44:6–12, 2007. 11, 88

[105] A. A. Serga, A. V. Chumak, and B. Hillebrands. Yig magnonics. *Journal of Physics D: Applied Physics*, 43:264002, 6 2010. 11, 23, 88

[106] V. E. Demidov, S. Urazhdin, B. Divinskiy, V. D. Bessonov, A. B. Rinkevich, V. V. Ustinov, and S. O. Demokritov. Chemical potential of quasi-equilibrium magnon gas driven by pure spin current. *Nature Comm.*, 8(1), 2017. 11, 27, 34

[107] Marcus W Doherty, Neil B Manson, Paul Delaney, Fedor Jelezko, Jörg Wrachtrup, and Lloyd C L Hollenberg. The nitrogen-vacancy colour centre in diamond. *Physics Reports*, 528:1–45, 2013. The nitrogen-vacancy colour centre in diamond. 11, 12, 14, 24

[108] J. M. Taylor, P. Cappellaro, L. Childress, L. Jiang, D. Budker, P. R. Hemmer, A. Yacoby, R. Walsworth, and M. D. Lukin. High-sensitivity diamond magnetometer with nanoscale resolution. *Nature Physics 2008 4:10*, 4:810–816, 9 2008. 11, 24

[109] L. Rondin, J. P. Tetienne, T. Hingant, J. F. Roch, P. Maletinsky, and V. Jacques. Magnetometry with nitrogen-vacancy defects in diamond. *Reports on Progress in Physics*, 77:056503, 5 2014. 11, 12, 14, 15, 16, 24

[110] Stephanie Wehner, David Elkouss, and Ronald Hanson. Quantum internet: A vision for the road ahead. *Science*, 362, 10 2018. 11

[111] A. Gruber, A. Dräbenstedt, C. Tietz, L. Fleury, J. Wrachtrup, and C. Von Borczyskowski. Scanning confocal optical microscopy and magnetic resonance on single defect centers. *Science*, 276:2012–2014, 6 1997. 12

[112] Sébastien Pezzagna, Jan Meijer, Sébastien Pezzagna, and Jan Meijer. High-resolution ion implantation from kev to mev. *Ion Implantation*, 5 2012. 12

[113] Jason M. Smith, Simon A. Meynell, Ania C. Bleszynski Jayich, and Jan Meijer. Colour centre generation in diamond for quantum technologies. *Nanophotonics*, 8:1889–1906, 11 2019. 12

[114] J. Achard, V. Jacques, and A. Tallaire. Chemical vapour deposition diamond single crystals with nitrogen-vacancy centres: a review of material synthesis and technology for quantum sensing applications. *Journal of Physics D: Applied Physics*, 53:313001, 5 2020. 12

[115] A. Dréau, M. Lesik, L. Rondin, P. Spinicelli, O. Arcizet, J. F. Roch, and V. Jacques. Avoiding power broadening in optically detected magnetic resonance of single nv defects for enhanced dc magnetic field sensitivity. *Physical Review B - Condensed Matter and Materials Physics*, 84:195204, 11 2011. 12, 13, 15, 16, 99, 104

[116] Thomas Wolf, Philipp Neumann, Kazuo Nakamura, Hitoshi Sumiya, Takeshi Ohshima, Junichi Isoya, and Jörg Wrachtrup. Subpicotesla diamond magnetometry. *Physical Review X*, 5:041001, 10 2015. 12

[117] Felix M. Stürner, Andreas Brenneis, Thomas Buck, Julian Kassel, Robert Rölver, Tino Fuchs, Anton Savitsky, Dieter Suter, Jens Grimmel, Stefan Hengesbach, Michael Förtsch, Kazuo Nakamura, Hitoshi Sumiya, Shinobu Onoda, Junichi Isoya, and Fedor Jelezko. Integrated and portable magnetometer based on nitrogen-vacancy ensembles in diamond. *Advanced Quantum Technologies*, 4:2000111, 4 2021. 12

[118] Zhecheng Wang, Fei Kong, Pengju Zhao, Zhehua Huang, Pei Yu, Ya Wang, Fazhan Shi, and Jiangfeng Du. Picotesla magnetometry of microwave fields with diamond sensors. *Science Advances*, 8:8158, 8 2022. 12

[119] M. S. Wolf, R. Badea, and J. Berezovsky. Fast nanoscale addressability of nitrogen-vacancy spins via coupling to a dynamic ferromagnetic vortex. *Nature Communications 2016 7:1*, 7:1–7, 6 2016. 12, 20, 88

[120] M. S. Wolf, R. Badea, M. Tader, and J. Berezovsky. Strong driving of a single coherent spin by a proximal chiral ferromagnet. *Physical Review B*, 96:014424, 7 2017. 12

[121] Paolo Andrich, Charles F. de las Casas, Xiaoying Liu, Hope L. Bretscher, Jonson R. Berman, F. Joseph Heremans, Paul F. Nealey, and David D. Awschalom. Long-range spin wave mediated control of defect qubits in nanodiamonds. *npj Quantum Information 2017 3:1*, 3:1–7, 7 2017. 12, 13, 21

[122] A. Gardill, M. C. Cambria, and S. Kolkowitz. Fast relaxation on qutrit transitions of nitrogen-vacancy centers in nanodiamonds. *Physical Review Applied*, 13:034010, 2 2020. 12

[123] Michael J. Burek, Nathalie P. De Leon, Brendan J. Shields, Birgit J.M. Hausmann, Yiwen Chu, Qimin Quan, Alexander S. Zibrov, Hongkun Park, Mikhail D. Lukin, and Marko Lončar. Free-standing mechanical and photonic nanostructures in single-crystal diamond. *Nano Letters*, 12:6084–6089, 12 2012. 12

[124] Yufan Li, Fabian A. Gerritsma, Samer Kurdi, Nina Codreanu, Simon Gröblacher, Ronald Hanson, Richard Norte, and Toeno van der Sar. A fiber-coupled scanning magnetometer with nitrogen-vacancy spins in a diamond nanobeam. 2 2023. 12

[125] C. L. Degen. Scanning magnetic field microscope with a diamond single-spin sensor. *Applied Physics Letters*, 92:243111, 6 2008. 12, 89

[126] P. Maletinsky, S. Hong, M. S. Grinolds, B. Hausmann, M. D. Lukin, R. L. Walsworth, M. Loncar, and A. Yacoby. A robust scanning diamond sensor for nanoscale imaging with single nitrogen-vacancy centres. *Nature Nanotechnology 2012 7:5*, 7:320–324, 4 2012. 12, 13, 18, 89

[127] Francesco Casola, Toeno Van Der Sar, and Amir Yacoby. Probing condensed matter physics with magnetometry based on nitrogen-vacancy centres in diamond. *Nature Reviews Materials 2018 3:1*, 3:1–13, 1 2018. 13, 18, 114

[128] L Du Preez. Electron paramagnetic resonance and optical investigations of defect centres in diamond, 1965. 12

[129] M. L. Goldman, A. Sipahigil, M. W. Doherty, N. Y. Yao, S. D. Bennett, M. Markham, D. J. Twitchen, N. B. Manson, A. Kubanek, and M. D. Lukin. Phonon-induced popu-

lation dynamics and intersystem crossing in nitrogen-vacancy centers. *Physical Review Letters*, 114:145502, 4 2015. 14

[130] Lucio Robledo, Hannes Bernien, Ilse Van Weperen, and Ronald Hanson. Control and coherence of the optical transition of single nitrogen vacancy centers in diamond. *Physical Review Letters*, 105:177403, 10 2010. 14

[131] A. Batalov, C. Zierl, T. Gaebel, P. Neumann, I. Y. Chan, G. Balasubramanian, P. R. Hemmer, F. Jelezko, and J. Wrachtrup. Temporal coherence of photons emitted by single nitrogen-vacancy defect centers in diamond using optical rabi-oscillations. *Physical Review Letters*, 100:077401, 2 2008. 14

[132] A. Gupta, L. Hacquebard, and L. Childress. Efficient signal processing for time-resolved fluorescence detection of nitrogen-vacancy spins in diamond. *JOSA B, Vol. 33, Issue 3, pp. B28-B34*, 33:B28–B34, 3 2016. 14

[133] Michal Gulka, Daniel Wirtitsch, Viktor Ivády, Jelle Vodnik, Jaroslav Hruby, Goele Magchiels, Emilie Bourgeois, Adam Gali, Michael Trupke, and Milos Nesladek. Room-temperature control and electrical readout of individual nitrogen-vacancy nuclear spins. *Nature Communications 2021 12:1*, 12:1–8, 7 2021. 14

[134] I. Meirzada, S. A. Wolf, A. Naiman, U. Levy, and N. Bar-Gill. Enhanced spin state readout of nitrogen-vacancy centers in diamond using infrared fluorescence. *Physical Review B*, 100:125436, 9 2019. 14

[135] B. J. Shields, Q. P. Unterreithmeier, N. P. De Leon, H. Park, and M. D. Lukin. Efficient readout of a single spin state in diamond via spin-to-charge conversion. *Physical Review Letters*, 114:136402, 3 2015. 14

[136] Qi Zhang, Yuhang Guo, Wentao Ji, Mengqi Wang, Jun Yin, Fei Kong, Yiheng Lin, Chunming Yin, Fazhan Shi, Ya Wang, and Jiangfeng Du. High-fidelity single-shot readout of single electron spin in diamond with spin-to-charge conversion. *Nature Communications 2021 12:1*, 12:1–6, 3 2021. 14

[137] Norman F. Ramsey. A molecular beam resonance method with separated oscillating fields. *Physical Review*, 78:695, 6 1950. 16

[138] Till Lenz, Arne Wickenbrock, Fedor Jelezko, Gopalakrishnan Balasubramanian, and Dmitry Budker. Magnetic sensing at zero field with a single nitrogen-vacancy center. *Quantum Science and Technology*, 6:034006, 6 2021. 16

[139] G. De Lange, D. Ristè, V. V. Dobrovitski, and R. Hanson. Single-spin magnetometry with multipulse sensing sequences. *Physical Review Letters*, 106:080802, 2 2011. 16

[140] H. J. Mamin, M. Kim, M. H. Sherwood, C. T. Rettner, K. Ohno, D. D. Awschalom, and D. Rugar. Nanoscale nuclear magnetic resonance with a nitrogen-vacancy spin sensor. *Science*, 339:557–560, 2 2013. 16

[141] H. Y. Carr and E. M. Purcell. Effects of diffusion on free precession in nuclear magnetic resonance experiments. *Physical Review*, 94:630, 5 1954. 16

[142] S. Meiboom and D. Gill. Modified spin-echo method for measuring nuclear relaxation times. *Review of Scientific Instruments*, 29:688–691, 12 1958. 16

[143] Shlomi Kotler, Nitzan Akerman, Yinnon Glickman, Anna Keselman, and Roee Ozeri. Single-ion quantum lock-in amplifier. *Nature 2011 473:7345*, 473:61–65, 5 2011. 16

[144] Guoqing Wang, Yi Xiang Liu, Yuan Zhu, and Paola Cappellaro. Nanoscale vector ac magnetometry with a single nitrogen-vacancy center in diamond. *Nano Letters*, 21:5143–5150, 6 2021. 16

[145] Alexander Stark, Nati Aharon, Thomas Unden, Daniel Louzon, Alexander Huck, Alex Retzker, Ulrik L. Andersen, and Fedor Jelezko. Narrow-bandwidth sensing of high-frequency fields with continuous dynamical decoupling. *Nature Communications 2017 8:1*, 8:1–6, 10 2017. 16

[146] A. Jarmola, V. M. Acosta, K. Jensen, S. Chemerisov, and D. Budker. Temperature- and magnetic-field-dependent longitudinal spin relaxation in nitrogen-vacancy ensembles in diamond. *Physical Review Letters*, 108:197601, 5 2012. 16

[147] Aldona Mzyk, Alina Sigaeva, and Romana Schirhagl. Relaxometry with nitrogen vacancy (nv) centers in diamond. *Accounts of Chemical Research*, 55:3572–3580, 12 2022. 16

[148] C. P. Slichter. *Principles of Magnetic Resonance*. Springer Berlin Heidelberg, 1990. 17, 77

[149] Michael Caouette-Mansour, Adrian Solyom, Brandon Ruffolo, Robert D Mcmichael, Jack Sankey, and Lilian Childress. Robust spin relaxometry with fast adaptive bayesian estimation. *PHYSICAL REVIEW APPLIED*, 17:64031, 2022. 17, 102, 114

[150] Saravanan Sengottuvel, Mariusz Mrózek, Mirosław Sawczak, Maciej J. Głowacki, Mateusz Ficek, Wojciech Gawlik, and Adam M. Wojciechowski. Wide-field magnetometry using nitrogen-vacancy color centers with randomly oriented micro-diamonds. *Scientific Reports 2022 12:1*, 12:1–9, 10 2022. 17

[151] Natascha Hedrich, Dominik Rohner, Marietta Batzer, Patrick Maletinsky, and Brendan J. Shields. Parabolic diamond scanning probes for single-spin magnetic field imaging. *Physical Review Applied*, 14:064007, 12 2020. 18

[152] Y. Dovzhenko, F. Casola, S. Schlotter, T. X. Zhou, F. Büttner, R. L. Walsworth, G. S.D. Beach, and A. Yacoby. Magnetostatic twists in room-temperature skyrmions explored by nitrogen-vacancy center spin texture reconstruction. *Nature Communications 2018 9:1*, 9:1–7, 7 2018. 18, 19

[153] K. Chang, A. Eichler, J. Rhensius, L. Lorenzelli, and C. L. Degen. Nanoscale imaging of current density with a single-spin magnetometer. *Nano Letters*, 17:2367–2373, 4 2017. 18

[154] Jean Philippe Tetienne, Nikolai Dontschuk, David A. Broadway, Alastair Stacey, David A. Simpson, and Lloyd C.L. Hollenberg. Quantum imaging of current flow in graphene. *Science Advances*, 3, 4 2017. 18

[155] Mark J.H. Ku, Tony X. Zhou, Qing Li, Young J. Shin, Jing K. Shi, Claire Burch, Laurel E. Anderson, Andrew T. Pierce, Yonglong Xie, Assaf Hamo, Uri Vool, Huil-

iang Zhang, Francesco Casola, Takashi Taniguchi, Kenji Watanabe, Michael M. Fogler, Philip Kim, Amir Yacoby, and Ronald L. Walsworth. Imaging viscous flow of the dirac fluid in graphene. *Nature 2020 583:7817*, 583:537–541, 7 2020. 18

[156] Alec Jenkins, Susanne Baumann, Haoxin Zhou, Simon A. Meynell, Yang Daipeng, Kenji Watanabe, Takashi Taniguchi, Andrew Lucas, Andrea F. Young, and Ania C. Bleszynski Jayich. Imaging the breakdown of ohmic transport in graphene. *Physical Review Letters*, 129:087701, 8 2022. 18

[157] Uri Vool, Assaf Hamo, Georgios Varnavides, Yaxian Wang, Tony X. Zhou, Nitesh Kumar, Yuliya Dovzhenko, Ziwei Qiu, Christina A.C. Garcia, Andrew T. Pierce, Johannes Gooth, Polina Anikeeva, Claudia Felser, Prineha Narang, and Amir Yacoby. Imaging phonon-mediated hydrodynamic flow in wte2. *Nature Physics 2021 17:11*, 17:1216–1220, 9 2021. 18

[158] L. Thiel, D. Rohner, M. Ganzhorn, P. Appel, E. Neu, B. Müller, R. Kleiner, D. Koelle, and P. Maletinsky. Quantitative nanoscale vortex imaging using a cryogenic quantum magnetometer. *Nature Nanotechnology 2016 11:8*, 11:677–681, 5 2016. 18

[159] Chunhui Du, Toeno van der Sar, Tony X. Zhou, Pramey Upadhyaya, Francesco Casola, Huiliang Zhang, Mehmet C. Onbasli, Caroline A. Ross, Ronald L. Walsworth, Yaroslav Tserkovnyak, and Amir Yacoby. Control and local measurement of the spin chemical potential in a magnetic insulator. *Science*, 357:195–198, 7 2017. 19, 20, 21, 22, 24, 108, 109, 113

[160] Iacopo Bertelli, Joris J. Carmiggelt, Tao Yu, Brecht G. Simon, Coosje C. Pothoven, Gerrit E.W. Bauer, Yaroslav M. Blanter, Jan Aarts, and Toeno Van Der Sar. Magnetic resonance imaging of spin-wave transport and interference in a magnetic insulator. *Science Advances*, 6:3556–3567, 11 2020. 19, 21, 89

[161] J. P. Tetienne, T. Hingant, J. V. Kim, L. Herrera Diez, J. P. Adam, K. Garcia, J. F. Roch, S. Rohart, A. Thiaville, D. Ravelosona, and V. Jacques. Nanoscale imaging and control of domain-wall hopping with a nitrogen-vacancy center microscope. *Science*, 344:1366–1369, 6 2014. 18

[162] J. P. Tetienne, T. Hingant, L. J. Martínez, S. Rohart, A. Thiaville, L. Herrera Diez, K. Garcia, J. P. Adam, J. V. Kim, J. F. Roch, I. M. Miron, G. Gaudin, L. Vila, B. Ocker, D. Ravelosona, and V. Jacques. The nature of domain walls in ultrathin ferromagnets revealed by scanning nanomagnetometry. *Nature Communications 2015 6:1*, 6:1–6, 4 2015. 18, 88

[163] Natascha Hedrich, Kai Wagner, Oleksandr V. Pylypovskyi, Brendan J. Shields, Tobias Kosub, Denis D. Sheka, Denys Makarov, and Patrick Maletinsky. Nanoscale mechanics of antiferromagnetic domain walls. *Nature Physics 2021 17:5*, 17:574–577, 2 2021. 18

[164] J. Y. Chauleau, T. Chirac, S. Fusil, V. Garcia, W. Akhtar, J. Tranchida, P. Thibaudeau, I. Gross, C. Blouzon, A. Finco, M. Bibes, B. Dkhil, D. D. Khalyavin, P. Manuel, V. Jacques, N. Jaouen, and M. Viret. Electric and antiferromagnetic chiral textures at multiferroic domain walls. *Nature Materials 2019 19:4*, 19:386–390, 11 2019. 18

[165] A. Haykal, J. Fischer, W. Akhtar, J. Y. Chauleau, D. Sando, A. Finco, F. Godel, Y. A. Birkhölzer, C. Carrétéro, N. Jaouen, M. Bibes, M. Viret, S. Fusil, V. Jacques, and V. Garcia. Antiferromagnetic textures in bifeo3 controlled by strain and electric field. *Nature Communications 2020 11:1*, 11:1–7, 4 2020. 18

[166] L. Rondin, J.-P. Tetienne, S. Rohart, A. Thiaville, T. Hingant, P. Spinicelli, J.-F. Roch, and V. Jacques. Stray-field imaging of magnetic vortices with a single diamond spin. *Nature Comm.*, 4:ncomms3279, 2013. 18

[167] M. S. Wolf, R. Badea, M. Tader, and J. Berezovsky. Strong driving of a single coherent spin by a proximal chiral ferromagnet. *Phys. Rev. B*, 96(1):014424, 2017. 18

[168] I. Gross, W. Akhtar, A. Hrabec, J. Sampaio, L. J. Martínez, S. Chouaieb, B. J. Shields, P. Maletinsky, A. Thiaville, S. Rohart, and V. Jacques. Skyrmion morphology in ultrathin magnetic films. *Physical Review Materials*, 2:024406, 2 2018. 18

[169] Aurore Finco, Angela Haykal, Rana Tanos, Florentin Fabre, Saddem Chouaieb, Waseem Akhtar, Isabelle Robert-Philip, William Legrand, Fernando Ajejas, Karim Bouzehouane, Nicolas Reyren, Thibaut Devolder, Jean Paul Adam, Joo Von Kim,

Vincent Cros, and Vincent Jacques. Imaging non-collinear antiferromagnetic textures via single spin relaxometry. *Nature Communications 2021 12:1*, 12:1–6, 2 2021. 18, 114

[170] L. Thiel, Z. Wang, M. A. Tschudin, D. Rohner, I. Gutiérrez-Lezama, N. Ubrig, M. Gibertini, E. Giannini, A. F. Morpurgo, and P. Maletinsky. Probing magnetism in 2d materials at the nanoscale with single-spin microscopy. *Science*, 364:973–976, 6 2019. 18

[171] F. Fabre, A. Finco, A. Purbawati, A. Hadj-Azzem, N. Rougemaille, J. Coraux, I. Philip, and V. Jacques. Characterization of room-temperature in-plane magnetization in thin flakes of crte2 with a single-spin magnetometer. *Physical Review Materials*, 5:034008, 3 2021. 18

[172] Umberto Celano, Hai Zhong, Florin Ciubotaru, Laurentiu Stoleriu, Alexander Stark, Peter Rickhaus, Felipe Fávaro de Oliveira, Mathieu Munsch, Paola Favia, Maxim Korytov, Patricia Van Marcke, Patrick Maletinsky, Christoph Adelmann, and Paul van der Heide. Probing magnetic defects in ultra-scaled nanowires with optically detected spin resonance in nitrogen-vacancy center in diamond. *Nano Letters*, 21:10409–10415, 12 2021. 18

[173] W. S. Huxter, M. L. Palm, M. L. Davis, P. Welter, C. H. Lambert, M. Trassin, and C. L. Degen. Scanning gradiometry with a single spin quantum magnetometer. *Nature Communications 2022 13:1*, 13:1–9, 6 2022. 20

[174] Toeno Van Der Sar, Francesco Casola, Ronald Walsworth, and Amir Yacoby. Nanometre-scale probing of spin waves using single electron spins. *Nature Communications 2015 6:1*, 6:1–8, 8 2015. 20, 24, 108

[175] C. S. Wolfe, S. A. Manuilov, C. M. Purser, R. Teeling-Smith, C. Dubs, P. C. Hammel, and V. P. Bhallamudi. Spatially resolved detection of complex ferromagnetic dynamics using optically detected nitrogen-vacancy spins. *Applied Physics Letters*, 108:232409, 6 2016. 20, 108

[176] C. S. Wolfe, V. P. Bhallamudi, H. L. Wang, C. H. Du, S. Manuilov, R. M. Teeling-Smith, A. J. Berger, R. Adur, F. Y. Yang, and P. C. Hammel. Off-resonant manipulation of spins in diamond via precessing magnetization of a proximal ferromagnet. *Physical Review B - Condensed Matter and Materials Physics*, 89:180406, 5 2014. 20, 24, 108

[177] M. R. Page, B. A. McCullian, C. M. Purser, J. G. Schulze, T. M. Nakatani, C. S. Wolfe, J. R. Childress, M. E. McConney, B. M. Howe, P. C. Hammel, and V. P. Bhallamudi. Optically detected ferromagnetic resonance in diverse ferromagnets via nitrogen vacancy centers in diamond. *Journal of Applied Physics*, 126:124902, 9 2019. 20, 24, 108, 113

[178] Eric Lee-Wong, Ruolan Xue, Feiyang Ye, Andreas Kreisel, Toeno Van Der Sar, Amir Yacoby, and Chunhui Rita Du. Nanoscale detection of magnon excitations with variable wavevectors through a quantum spin sensor. *Nano Letters*, 20:3284–3290, 5 2020. 20, 89, 108

[179] Brendan A. McCullian, Ahmed M. Thabt, Benjamin A. Gray, Alex L. Melendez, Michael S. Wolf, Vladimir L. Safonov, Denis V. Pelekhov, Vidya P. Bhallamudi, Michael R. Page, and P. Chris Hammel. Broadband multi-magnon relaxometry using a quantum spin sensor for high frequency ferromagnetic dynamics sensing. *Nature Communications 2020 11:1*, 11:1–8, 10 2020. 20, 24, 108

[180] B. Flebus and Y. Tserkovnyak. Quantum-impurity relaxometry of magnetization dynamics. *Physical Review Letters*, 121:187204, 11 2018. 20

[181] Hailong Wang, Shu Zhang, Nathan J. McLaughlin, Benedetta Flebus, Mengqi Huang, Yuxuan Xiao, Chuanpu Liu, Mingzhong Wu, Eric E. Fullerton, Yaroslav Tserkovnyak, and Chunhui Rita Du. Noninvasive measurements of spin transport properties of an antiferromagnetic insulator. *Science Advances*, 8:8562, 1 2022. 20

[182] Xiaoche Wang, Yuxuan Xiao, Chuanpu Liu, Eric Lee-Wong, Nathan J. McLaughlin, Hanfeng Wang, Mingzhong Wu, Hailong Wang, Eric E. Fullerton, and Chunhui Rita Du. Electrical control of coherent spin rotation of a single-spin qubit. *npj Quantum Information 2020 6:1*, 6:1–6, 9 2020. 21

[183] H. Zhang, M. J.H. Ku, F. Casola, C. H.R. Du, T. Van Der Sar, M. C. Onbasli, C. A. Ross, Y. Tserkovnyak, A. Yacoby, and R. L. Walsworth. Spin-torque oscillation in a magnetic insulator probed by a single-spin sensor. *Physical Review B*, 102:024404, 7 2020. 21, 22, 85, 88, 110, 114

[184] Gerald Q. Yan, Senlei Li, Tatsuya Yamamoto, Mengqi Huang, Nathan J. McLaughlin, Takayuki Nozaki, Hailong Wang, Shinji Yuasa, and Chunhui Rita Du. Electric-field-induced coherent control of nitrogen-vacancy centers. *Physical Review Applied*, 18:064031, 12 2022. 21, 88, 109

[185] Dwi Prananto, Yuta Kainuma, Kunitaka Hayashi, Norikazu Mizuochi, Ken Ichi Uchida, and Toshu An. Probing thermal magnon current mediated by coherent magnon via nitrogen-vacancy centers in diamond. *Physical Review Applied*, 16:064058, 12 2021. 21

[186] Iacopo Bertelli, Brecht G. Simon, Tao Yu, Jan Aarts, Gerrit E.W. Bauer, Yaroslav M. Blanter, and Toeno van der Sar. Imaging spin-wave damping underneath metals using electron spins in diamond. *Advanced Quantum Technologies*, 4:2100094, 12 2021. 21

[187] Brecht G. Simon, Samer Kurdi, Helena La, Iacopo Bertelli, Joris J. Carmiggelt, Maximilian Ruf, Nick De Jong, Hans Van Den Berg, Allard J. Katan, and Toeno Van Der Sar. Directional excitation of a high-density magnon gas using coherently driven spin waves. *Nano Letters*, 21:8213–8219, 10 2021. 21, 89, 108

[188] Tony X. Zhou, Joris J. Carmiggelt, Lisa M. Gächter, Ilya Esterlis, Dries Sels, Rainer J. Stöhr, Chunhui Du, Daniel Fernandez, Joaquin F. Rodriguez-Nieva, Felix Büttner, Eugene Demler, and Amir Yacoby. A magnon scattering platform. *Proceedings of the National Academy of Sciences of the United States of America*, 118:e2019473118, 6 2021. 21, 89

[189] Brecht G. Simon, Samer Kurdi, Joris J. Carmiggelt, Michael Borst, Allard J. Katan, and Toeno Van Der Sar. Filtering and imaging of frequency-degenerate spin waves using nanopositioning of a single-spin sensor. *Nano Letters*, 2022. 21, 89, 108

[190] B. Divinskiy, V. E. Demidov, S. O. Demokritov, A. B. Rinkevich, and S. Urazhdin. Route toward high-speed nano-magnonics provided by pure spin currents. *Applied Physics Letters*, 109:252401, 12 2016. 23

[191] B.A. McCullian, M. Chilcote, V.P. Bhallamudi, C.M. Purser, E. Johnston-Halperin, and P.C. Hammel. Broadband optical detection of ferromagnetic resonance from the organic-based ferrimagnet v[tcne] ¡i¿ ¡sub¿x¡/sub¿ ¡/i¿ using n- ¡i¿v¡/i¿ centers in diamond. *Physical Review Applied*, 14:024033, 8 2020. 24

[192] J. P. Tetienne, L. Rondin, P. Spinicelli, M. Chipaux, T. Debuisschert, J. F. Roch, and V. Jacques. Magnetic-field-dependent photodynamics of single nv defects in diamond: an application to qualitative all-optical magnetic imaging. *New Journal of Physics*, 14:103033, 10 2012. 24, 93, 112

[193] V. E. Demidov, S. Urazhdin, B. Divinskiy, V. D. Bessonov, A. B. Rinkevich, V. V. Ustinov, and S. O. Demokritov. Chemical potential of quasi-equilibrium magnon gas driven by pure spin current. *Nature Communications 2017 8:1*, 8:1–7, 11 2017. 24, 109

[194] D. Ralph and M. Stiles. Spin transfer torques. *J. Mag. & Mag. Mat.*, 320(7):1190–1216, 2008. 26

[195] A. Manchon, I. M. Miron, T. Jungwirth, J. Sinova, J. Zelezný, A. Thiaville, K. Garello, and P. Gambardella. Current-induced spin-orbit torques in ferromagnetic and antiferromagnetic systems. *arXiv:1801.09636*, 2018. 26

[196] M. W. Doherty, N. B. Manson, P. Delaney, F. Jelezko, J. Wrachtrup, and L. C. Hollenberg. The nitrogen-vacancy colour centre in diamond. *Phys. Rep.*, 528(1):1–45, 2013. 26, 43

[197] L. Rondin, J.-P. Tetienne, T. Hingant, J.-F. Roch, P. Maletinsky, and V. Jacques. Magnetometry with nitrogen-vacancy defects in diamond. *Rep. Prog. in Phys.*, 77(5):056503, 2014. 26

[198] F. Casola, T. van der Sar, and A. Yacoby. Probing condensed matter physics with magnetometry based on nitrogen-vacancy centres in diamond. *Nature Rev. Mat.*, 3(1):17088, 2018. 26

[199] P. Maletinsky, S. Hong, M. S. Grinolds, B. Hausmann, M. D. Lukin, R. L. Walsworth, M. Loncar, and A. Yacoby. A robust scanning diamond sensor for nanoscale imaging with single nitrogen-vacancy centres. *Nature Nano.*, 7(5):320–324, 2012. 26

[200] E. Rittweger, K. Han, S. Irvine, C. Eggeling, and S. W. Hell. STED microscopy reveals crystal colour centres with nanometric resolution. *Nature Phot.*, 3(3):144–147, 2009. 26

[201] C. L. Degen. Scanning magnetic field microscope with a diamond single-spin sensor. *Appl. Phys. Lett.*, 92(24):243111, 2008. 26

[202] J. M. Taylor, P. Cappellaro, L. Childress, L. Jiang, D. Budker, P. R. Hemmer, A. Yacoby, R. Walsworth, and M. D. Lukin. High-sensitivity diamond magnetometer with nanoscale resolution. *Nature Phys.*, 4(10):810–816, 2008. 26

[203] J.-P. Tetienne, T. Hingant, L. Rondin, A. Cavaillès, L. Mayer, G. Dantelle, T. Gacoin, J. Wrachtrup, J.-F. Roch, and V. Jacques. Spin relaxometry of single nitrogen-vacancy defects in diamond nanocrystals for magnetic noise sensing. *Phys. Rev. B*, 87(23), 2013. 26

[204] T. Rosskopf, A. Dussaux, K. Ohashi, M. Loretz, R. Schirhagl, H. Watanabe, S. Shikata, K. M. Itoh, and C. L. Degen. Investigation of surface magnetic noise by shallow spins in diamond. *Phys. Rev. Lett.*, 112(14):147602, 2014. 26

[205] B. A. Myers, A. Das, M. C. Dartiailh, K. Ohno, D. D. Awschalom, and A. C. Bleszynski Jayich. Probing surface noise with depth-calibrated spins in diamond. *Phys. Rev. Lett.*, 113(2):027602, 2014. 26

[206] J.-P. Tetienne, T. Hingant, L. Rondin, S. Rohart, A. Thiaville, J.-F. Roch, and V. Jacques. Quantitative stray field imaging of a magnetic vortex core. *Phys. Rev. B*, 88(21):214408, 2013. 26

[207] R. Badea, M. S. Wolf, and J. Berezovsky. Exploiting bistable pinning of a ferromagnetic vortex for nitrogen-vacancy spin control. *Appl. Phys. Lett.*, 109(13):132403, 2016. 26, 36

[208] J.-P. Tetienne, T. Hingant, J.-V. Kim, L. H. Diez, J.-P. Adam, K. Garcia, J.-F. Roch, S. Rohart, A. Thiaville, D. Ravelosona, and V. Jacques. Nanoscale imaging and control of domain-wall hopping with a nitrogen-vacancy center microscope. *Science*, 344(6190):1366–1369, 2014. 26

[209] C. S. Wolfe, V. P. Bhallamudi, H. L. Wang, C. H. Du, S. Manuilov, R. M. Teeling-Smith, A. J. Berger, R. Adur, F. Y. Yang, and P. C. Hammel. Off-resonant manipulation of spins in diamond via precessing magnetization of a proximal ferromagnet. *Phys. Rev. B*, 89(18):180406, 2014. 26, 27, 32

[210] T. van der Sar, F. Casola, R. Walsworth, and A. Yacoby. Nanometre-scale probing of spin waves using single electron spins. *Nature Comm.*, 6:7886, 2015. 26, 27, 32, 42, 43, 79

[211] C. S. Wolfe, S. A. Manuilov, C. M. Purser, R. Teeling-Smith, C. Dubs, P. C. Hammel, and V. P. Bhallamudi. Spatially resolved detection of complex ferromagnetic dynamics using optically detected nitrogen-vacancy spins. *Appl. Phys. Lett.*, 108(23):232409, 2016. 26, 27, 32

[212] M. R. Page, F. Guo, C. M. Purser, J. G. Schulze, T. M. Nakatani, C. S. Wolfe, J. R. Childress, P. C. Hammel, G. D. Fuchs, and V. P. Bhallamudi. Optically Detected Ferromagnetic Resonance in Metallic Ferromagnets via Nitrogen Vacancy Centers in Diamond. *arXiv:1607.07485* 2016. 26, 27, 32

[213] C. Du, T. van der Sar, T. X. Zhou, P. Upadhyaya, F. Casola, H. Zhang, M. C. Onbasli, C. A. Ross, R. L. Walsworth, Y. Tserkovnyak, and A. Yacoby. Control and local measurement of the spin chemical potential in a magnetic insulator. *Science*, 357(6347):195–198, 2017. 26, 27, 32, 34, 79

[214] S. I. Kiselev, J. C. Sankey, I. N. Krivorotov, N. C. Emley, R. J. Schoelkopf, R. A. Buhrman, and D. C. Ralph. Microwave oscillations of a nanomagnet driven by a spin-polarized current. *Nature*, 425(6956):380–383, 2003. 26, 31

[215] A. A. Tulapurkar, Y. Suzuki, A. Fukushima, H. Kubota, H. Maehara, K. Tsunekawa, D. D. Djayaprawira, N. Watanabe, and S. Yuasa. Spin-torque diode effect in magnetic tunnel junctions. *Nature*, 438(7066):339–342, 2005. 26

[216] J. C. Sankey, P. M. Braganca, A. G. F. Garcia, I. N. Krivorotov, R. A. Buhrman, and D. C. Ralph. Spin-transfer-driven ferromagnetic resonance of individual nanomagnets. *Phys. Rev. Lett.*, 96(22), 2006. 26, 53

[217] H. Suhl. The theory of ferromagnetic resonance at high signal powers. *J. Phys. & Chem. Solids*, 1(4):209–227, 1957. 27

[218] R. Costa Filho, M. Cottam, and G. Farias. Microscopic theory of dipole-exchange spin waves in ferromagnetic films: Linear and nonlinear processes. *Phys. Rev. B*, 62(10):6545–6560, 2000. 27

[219] A. Y. Dobin and R. H. Victora. Intrinsic Nonlinear Ferromagnetic Relaxation in Thin Metallic Films. *Phys. Rev. Lett.*, 90(16):167203, 2003. 27

[220] C. T. Boone, J. A. Katine, J. R. Childress, V. Tiberkevich, A. Slavin, J. Zhu, X. Cheng, and I. N. Krivorotov. Resonant Nonlinear Damping of Quantized Spin Waves in Ferromagnetic Nanowires: A Spin Torque Ferromagnetic Resonance Study. *Phys. Rev. Lett.*, 103(16):167601, 2009. 27

[221] H. Schultheiss, K. Vogt, and B. Hillebrands. Direct observation of nonlinear four-magnon scattering in spin-wave microconduits. *Phys. Rev. B*, 86(5):054414, 2012. 27

[222] I. Barsukov, H. K. Lee, A. A. Jara, Y.-J. Chen, A. M. Gonçalves, C. Sha, J. A. Katine, R. E. Arias, B. A. Ivanov, and I. N. Krivorotov. Giant resonant nonlinear damping in nanoscale ferromagnets. *arXiv:1803.10925*, 2018. 27

[223] See supplementary materials for more information. 29, 31, 34, 35, 36

[224] L. Liu, T. Moriyama, D. C. Ralph, and R. A. Buhrman. Spin-torque ferromagnetic resonance induced by the spin Hall effect. *Phys. Rev. Lett.*, 106(3):036601, 2011. 29, 44, 62, 66, 68

[225] Z. Duan, C. T. Boone, X. Cheng, I. N. Krivorotov, N. Reckers, S. Stienen, M. Farle, and J. Lindner. Spin-wave modes in permalloy/platinum wires and tuning of the mode damping by spin Hall current. *Phys. Rev. B*, 90(2), 2014. 32, 59, 96

[226] J. Sankey, I. Krivorotov, S. Kiselev, P. Braganca, N. Emley, R. Buhrman, and D. Ralph. Mechanisms limiting the coherence time of spontaneous magnetic oscillations driven by dc spin-polarized currents. *Phys. Rev. B*, 72(22), 2005. 32

[227] D. V. Berkov and N. L. Gorn. Magnetization oscillations induced by a spin-polarized current in a point-contact geometry: Mode hopping and nonlinear damping effects. *Phys. Rev. B*, 76(14), 2007. 32

[228] A. Jarmola, V. M. Acosta, K. Jensen, S. Chemerisov, and D. Budker. Temperature- and magnetic-field-dependent longitudinal spin relaxation in nitrogen-vacancy ensembles in diamond. *Phys. Rev. Lett.*, 108(19), 2012. 36

[229] C. Lee, E. Gu, M. Dawson, I. Friel, and G. Scarsbrook. Etching and micro-optics fabrication in diamond using chlorine-based inductively-coupled plasma. *Diamond & Rel. Mat.*, 17(7):1292–1296, 2008. 37

[230] Y. Chu, N. de Leon, B. Shields, B. Hausmann, R. Evans, E. Togan, M. J. Burek, M. Markham, A. Stacey, A. Zibrov, A. Yacoby, D. Twitchen, M. Loncar, H. Park, P. Maletinsky, and M. Lukin. Coherent optical transitions in implanted nitrogen vacancy centers. *Nano Lett.*, 14(4):1982–1986, 2014. 37

[231] C. Kurtsiefer, S. Mayer, P. Zarda, and H. Weinfurter. Stable solid-state source of single photons. *Phys. Rev. Lett.*, 85:290–293, 2000. 39

[232] R. Verberk and M. Orrit. Photon statistics in the fluorescence of single molecules and nanocrystals: Correlation functions versus distributions of on- and off-times. *J. Chem. Phys.*, 119(4):2214–2222, 2003. 39

[233] J.-P. Tetienne, L. Rondin, P. Spinicelli, M. Chipaux, T. Debuisschert, J.-F. Roch, and V. Jacques. Magnetic-field-dependent photodynamics of single NV defects in diamond: an application to qualitative all-optical magnetic imaging. *New J. Phys.*, 14(10):103033, 2012. 42, 112

[234] P. Elleaume, O. Chubar, and J. Chavanne. Computing 3d magnetic fields from insertion devices. In *Proceedings of the 1997 Particle Accelerator Conference*. IEEE, 1997. 42

[235] S. Felton, A. M. Edmonds, M. E. Newton, P. M. Martineau, D. Fisher, D. J. Twitchen, and J. M. Baker. Hyperfine interaction in the ground state of the negatively charged nitrogen vacancy center in diamond. *Phys. Rev. B*, 79(7), 2009. 43

[236] S. O. Valenzuela and M. Tinkham. Direct electronic measurement of the spin Hall effect. *Nature*, 442(7099):176–179, 2006. 44

[237] V. Tshitoyan, C. Ciccarelli, A. P. Mihai, M. Ali, A. C. Irvine, T. A. Moore, T. Jungwirth, and A. J. Ferguson. Electrical manipulation of ferromagnetic NiFe by antiferromagnetic IrMn. *Phys. Rev. B*, 92(21):214406, 2015. 45, 61

[238] J. C. Sankey, Y.-T. Cui, J. Z. Sun, J. C. Slonczewski, R. A. Buhrman, and D. C. Ralph. Measurement of the spin-transfer-torque vector in magnetic tunnel junctions. *Nature Phys.*, 4(1):67–71, 2008. 66

[239] H. Kubota, A. Fukushima, K. Yakushiji, T. Nagahama, S. Yuasa, K. Ando, H. Maehara, Y. Nagamine, K. Tsunekawa, D. D. Djayaprawira, N. Watanabe, and Y. Suzuki. Quantitative measurement of voltage dependence of spin-transfer torque in MgO-based magnetic tunnel junctions. *Nature Phys.*, 4(1):37–41, 2008. 66

[240] W. F. Brown. Thermal fluctuations of a single-domain particle. *Phys. Rev.*, 130(5):1677–1686, 1963. 67, 96

[241] J. P. Nibarger, R. Lopusnik, Z. Celinski, and T. J. Silva. Variation of magnetization and the Landé g factor with thickness in Ni-Fe films. *Appl. Phys. Lett.*, 83(1):93–95, 2003. 68

[242] B. A. Kalinikos and A. N. Slavin. Theory of dipole-exchange spin wave spectrum for ferromagnetic films with mixed exchange boundary conditions. *J. Phys. C: Solid State Phys.*, 19(35):7013, 1986. 75

[243] N. Smith, D. Markham, and D. LaTourette. Magnetoresistive measurement of the exchange constant in varied-thickness permalloy films. *J. Appl. Phys.*, 65(11):4362–4365, 1989. 75

[244] C. Bayer, J. Jorzick, B. Hillebrands, S. O. Demokritov, R. Kouba, R. Bozinoski, A. N. Slavin, K. Y. Guslienko, D. V. Berkov, N. L. Gorn, and M. P. Kostylev. Spin-wave excitations in finite rectangular elements of $Ni_{80}Fe_{20}$. *Phys. Rev. B*, 72(6), 2005. 75, 76

[245] K. Y. Guslienko, S. Demokritov, B. Hillebrands, and A. Slavin. Effective dipolar boundary conditions for dynamic magnetization in thin magnetic stripes. *Phys. Rev. B*, 66(13), 2002. 75

[246] T. Brächer, O. Boulle, G. Gaudin, and P. Pirro. Creation of unidirectional spin-wave emitters by utilizing interfacial Dzyaloshinskii-Moriya interaction. *Phys. Rev. B*, 95(6), 2017. 76

[247] Andrii V. Chumak, Alexander A. Serga, and Burkard Hillebrands. Magnon transistor for all-magnon data processing. *Nature Communications 2014 5:1*, 5:1–8, 8 2014. 88

[248] Mohammad Zahedinejad, Himanshu Fulara, Roman Khymyn, Afshin Houshang, Mykola Dvornik, Shunsuke Fukami, Shun Kanai, Hideo Ohno, and Johan Åkerman. Memristive control of mutual spin hall nano-oscillator synchronization for neuromorphic computing. *Nature Materials 2021 21:1*, 21:81–87, 11 2021. 88

[249] Luuk J.P. Ament, Michel Van Veenendaal, Thomas P. Devereaux, John P. Hill, and Jeroen Van Den Brink. Resonant inelastic x-ray scattering studies of elementary excitations. *Reviews of Modern Physics*, 83:705–767, 6 2011. 88

[250] Nick Träger, Felix Groß, Johannes Förster, Korbinian Baumgaertl, Hermann Stoll, Markus Weigand, Gisela Schütz, Dirk Grundler, and Joachim Gräfe. Single shot ac-

quisition of spatially resolved spin wave dispersion relations using x-ray microscopy. *Scientific Reports 2020 10:1*, 10:1–6, 10 2020. 88

[251] L. Rondin, J. P. Tetienne, S. Rohart, A. Thiaville, T. Hingant, P. Spinicelli, J. F. Roch, and V. Jacques. Stray-field imaging of magnetic vortices with a single diamond spin. *Nature Communications 2013 4:1*, 4:1–5, 7 2013. 88

[252] P. J. Scheidegger, S. Diesch, M. L. Palm, and C. L. Degen. Scanning nitrogen-vacancy magnetometry down to 350mk. *Applied Physics Letters*, 120:224001, 5 2022. 88

[253] C Gonzalez-Ballestero, Toeno Van Der Sar, and O Romero-Isart. Towards a quantum interface between spin waves and paramagnetic spin baths. *Physical Review B*, 105:75410, 2022. 89

[254] Adrian Solyom, Zackary Flansberry, Märta A. Tschudin, Nathaniel Leitao, Michel Pioro-Ladrière, Jack C. Sankey, and Lilian I. Childress. Probing a spin transfer controlled magnetic nanowire with a single nitrogen-vacancy spin in bulk diamond. *Nano Letters*, 18:6494–6499, 10 2018. 89, 91, 94, 95, 96, 97, 102

[255] H. Suhl. The theory of ferromagnetic resonance at high signal powers. *Journal of Physics and Chemistry of Solids*, 1:209–227, 1957. 89

[256] J. P. Nibarger, R. Lopusnik, Z. Celinski, and T. J. Silva. Variation of magnetization and the landé g factor with thickness in ni–fe films. *Applied Physics Letters*, 83:93–95, 7 2003. 96

[257] J. A. Osborn. Demagnetizing factors of the general ellipsoid. *Physical Review*, 67:351, 6 1945. 96

[258] Vladimíra Petráková, Andrew Taylor, Irena Kratochvílová, František Fendrych, Jiří Vacík, Jan Kučka, Jan Štursa, Petr Cígler, Miroslav Ledvina, Anna Fišerová, Peter Kneppo, and Miloš Nesládek. Luminescence of nanodiamond driven by atomic functionalization: Towards novel detection principles. *Advanced Functional Materials*, 22:812–819, 2 2012. 103

[259] K. M.C. Fu, C. Santori, P. E. Barclay, and R. G. Beausoleil. Conversion of neutral nitrogen-vacancy centers to negatively charged nitrogen-vacancy centers through selective oxidation. *Applied Physics Letters*, 96:121907, 3 2010. 103

[260] Felipe Fávaro De Oliveira, S. Ali Momenzadeh, Ya Wang, Mitsuharu Konuma, Matthew Markham, Andrew M. Edmonds, Andrej Denisenko, and Jörg Wrachtrup. Effect of low-damage inductively coupled plasma on shallow nitrogen-vacancy centers in diamond. *Applied Physics Letters*, 107:073107, 8 2015. 103

[261] A. A. Tulapurkar, Y. Suzuki, A. Fukushima, H. Kubota, H. Maehara, K. Tsunekawa, D. D. Djayaprawira, N. Watanabe, and S. Yuasa. Spin-torque diode effect in magnetic tunnel junctions. *Nature 2005 438:7066*, 438:339–342, 11 2005. 107

[262] Charles Kittel. On the theory of ferromagnetic resonance absorption. *Physical Review*, 73:155, 1 1948. 107

[263] Sora Kawai, Hayate Yamano, Takahiro Sonoda, Kanami Kato, Jorge J. Buendia, Taisuke Kageura, Ryosuke Fukuda, Takuma Okada, Takashi Tanii, Taisei Higuchi, Moriyoshi Haruyama, Keisuke Yamada, Shinobu Onoda, Takeshi Ohshima, Wataru Kada, Osamu Hanaizumi, Alastair Stacey, Tokuyuki Teraji, Shozo Kono, Junichi Isoya, and Hiroshi Kawarada. Nitrogen-terminated diamond surface for nanoscale nmr by shallow nitrogen-vacancy centers. *Journal of Physical Chemistry C*, 123:3594–3604, 2 2019. 109

[264] M. V. Hauf, B. Grotz, B. Naydenov, M. Dankerl, S. Pezzagna, J. Meijer, F. Jelezko, J. Wrachtrup, M. Stutzmann, F. Reinhard, and J. A. Garrido. Chemical control of the charge state of nitrogen-vacancy centers in diamond. *Physical Review B - Condensed Matter and Materials Physics*, 83:081304, 2 2011. 109

[265] Hayate Yamano, Sora Kawai, Kanami Kato, Taisuke Kageura, Masafumi Inaba, Takuma Okada, Itaru Higashimata, Moriyoshi Haruyama, Takashi Tanii, Keisuke Yamada, Shinobu Onoda, Wataru Kada, Osamu Hanaizumi, Tokuyuki Teraji, Junichi Isoya, and Hiroshi Kawarada. Charge state stabilization of shallow nitrogen vacancy

centers in diamond by oxygen surface modification. *Japanese Journal of Applied Physics*, 56:04CK08, 4 2017. 109

[266] R. Badea, M. S. Wolf, and J. Berezovsky. Coherent rotation of a single spin via adiabatic half passage in the presence of a ferromagnetic vortex. *Quantum Science and Technology*, 8:025008, 2 2023. 114